AD-A098 081 KANSAS STATE UNIV MANHATTAN DEPT OF CHEMISTRY F/G 7/4
DEVELOPMENT AND USE OF TIME RESOLVED SPECTROSCOPY.(U)
MAR 81 W G FATELEY, R M HAMMAKER AFOSR-78-3617
UNCLASSIFIED AFOSR-TR-81-0351 NL

1 OF 2
AD A
098081

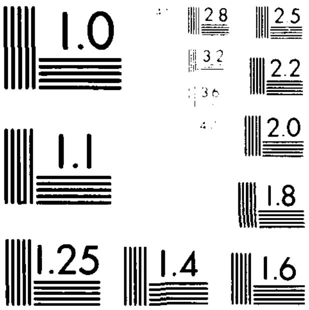
1.0
2.8
2.5
3.2
2.2
3.6
4.0
2.0
1.1
1.8
1.25
1.4
1.6

MICROCOPY RESOLUTION TEST CHART

NATIONAL BUREAU OF STANDARDS [illegible]

AFOSR-TR- 81-0351

LEVEL II

12

AD A098081

A Final Report

for

Air Force, Office of Scientific Research

Grant Number AFOSR - 78-3617

June 1, 1978 - February 28, 1981

Development and Use of Time Resolved Spectroscopy

Submitted by

W. G. Fateley

R. M. Hammaker

Principal Investigators

DTIC
ELECTE
APR 22 1981
S
A

March 1981

FILE COPY

81 4 22 029

Approved for public release;
distribution unlimited.

REPORT DOCUMENTATION PAGE	READ INSTRUCTIONS BEFORE COMPLETING FORM
1. REPORT NUMBER **AFOSR-TR- 81-0351** | 2. GOVT ACCESSION NO. AD-A098 081	3. RECIPIENT'S CATALOG NUMBER
4. TITLE (and Subtitle) Development and Use of Time Resolved Spectroscopy	5. TYPE OF REPORT & PERIOD COVERED Final 6. PERFORMING ORG. REPORT NUMBER
7. AUTHOR(s) W. G. Fateley and R. M. Hammaker	8. CONTRACT OR GRANT NUMBER(s) AFOSR-78-3617
9. PERFORMING ORGANIZATION NAME AND ADDRESS Kansas State University Department of Chemistry Manhattan, Kansas 66506	10. PROGRAM ELEMENT, PROJECT, TASK AREA & WORK UNIT NUMBERS 61102F 2303/A1
11. CONTROLLING OFFICE NAME AND ADDRESS Air Force Office of Scientific Research/NC Bldg. 410, Bolling AFB, DC 20332	12. REPORT DATE March 1981 13. NUMBER OF PAGES 114
14. MONITORING AGENCY NAME & ADDRESS (if different from Controlling Office)	15. SECURITY CLASS. (of this report) Unclassified 15a. DECLASSIFICATION DOWNGRADING SCHEDULE

16. DISTRIBUTION STATEMENT (of this Report)

Approved for public release; distribution unlimited.

17. DISTRIBUTION STATEMENT (of the abstract entered in Block 20, if different from Report)

18. SUPPLEMENTARY NOTES

19. KEY WORDS (Continue on reverse side if necessary and identify by block number)

Time Resolved Spectroscopy
Michelson's Interferometer
Fourier Transform Spectroscopy
Pulsed Laser Excitation
Interferogram
Absorption Studies
Reaction Intermediates
Band Shapes

20. ABSTRACT (Continue on reverse side if necessary and identify by block number)

The research reported demonstrates the application of Time Resolved Spectroscopy (TRS) to dynamic conditions in polymers. The Michelson's interferometer and Fourier Transform Spectroscopy (FTS) were employed in this study. TRS technique involves the coordination of reaction stimulation, e.g., pulsed laser excitation of gases or stretching and relaxation in polymers, and the recording of the interferogram at some unit time after stimulation. In the cases of gases, for versatility the

reaction vessel is designed to allow either emission or absorption studies. Time resolved spectroscopy provides a very attractive means for the elucidation of the structure of reaction intermediates and products, because this technique provides sufficient data for examination of the band shapes of materials and deduction of the energy distributions within the molecules for successive times during reaction.

9 A Final Report. 1 Jun 78 - 28 Feb 81

for

Air Force, Office of Scientific Research

15 Grant Number AFOSR — 78-3617 16 2303 17 A1

June 1, 1978 - February 28, 1981

6 Development and Use of Time Resolved Spectroscopy.

Submitted by

10 W. G. Fateley

R. M. Hammaker

Principal Investigators

18 AFOSR

19 TR-81-0301

AIR FORCE OFFICE OF SCIENTIFIC RESEARCH (AFSC)
NOTICE OF TRANSMITTAL TO DDC
This technical report has been reviewed and is
approved for public release IAW AFR 190-12 (7b).
Distribution is unlimited.
A. D. BLOSE
Technical Information Officer

11 Mar[redacted]81 12 115

40

Table of Contents

PAGE

I. Introduction to Fourier Transform Infrared Spectroscopy . . . .

II. A Description of Time Resolved Spectroscopy . . . .

III. Some Optimizing Conditions for Time Resolved Spectroscopy . . .

IV. Some Preliminary Time Resolved Results . . . .

V. Publications, Seminars and Talks During the Period of this Grant . . . .

VI. Summary . . . .

VII. Acknowledgment . . . .

VIII. Manuscripts, Preprints and Papers Sponsored by AFOSR under this Grant . . . .

Accession For
NTIS GRA&I ☑
DTIC TAB ☐
Unannounced ☐
Justification
By
Distribution/
Availability Codes
Dist | Avail and/or Special
A

I. Introduction to Fourier Transform Infrared Spectroscopy

Interferometry and Fourier Transform Spectroscopy (FTS)

The great advantage of interferometers comes from the careful mating of very old techniques known to A. Michelson[1] and others in 1887 with the new technology of lasers and computers. The mathematical principle of Baron Jean Baptiste Fourier, the French mathematician, is applied to the interpretation of the spectra - therefore the name Fourier Transform Spectroscopy. Essentially Fourier's theory allows us to treat a complex summation of cosine waves (the interferogram) of described intensity and interprets this data in terms of spectral intensity at a certain frequency. The theory of Fourier Transform Spectroscopy has been treated in detail by others[2,3] and is now standard; so we have chosen only to outline the basic details in a qualitative sense.

The Michelson's interferometer consists of two mirrors and a beam splitter (see Fig. 1). The source radiation (or in some applications the emission radiation) reaches the beam splitter at a 45° angle. The beam splitter (BS) passes approximately 50% of the radiation to a moveable mirror (mm) and the residual radiation is reflected to a fixed mirror (fm). In the newest instrumentation the moveable mirror is operated rapidly, cycling approximately every second, on an air bearing. The resulting reflection from each mirror returns to the beam splitter, where the reflection from the moveable mirror (mm) is reflected. The combined waves continue onto the detector. In the absorption mode the sample cell is placed before the detector; however, in the emission mode of interest in some experiments the sample is the source.

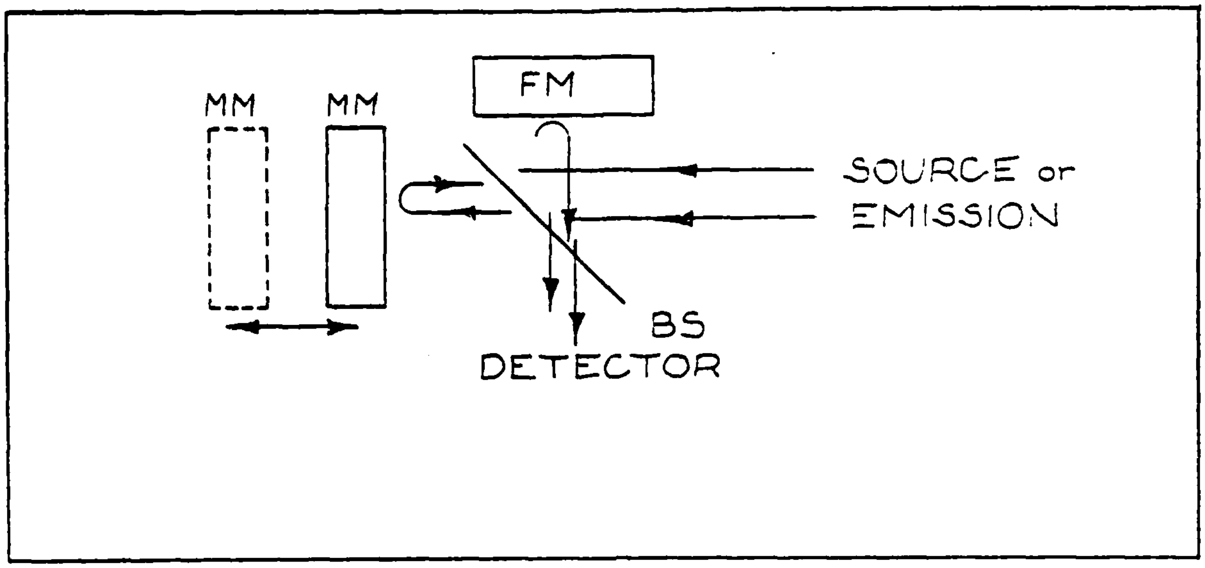

Figure 1. Michelson Interferometer

BS = beam splitter, selected for region of interest,

fm = fixed mirror

mm = moveable mirror

Fig. 1. Diagram of an interferometer

The mirror movement is very accurately measured by a laser impinging upon the back of the mirror. Through the use of Moiré fringes generated using this laser, the position, x, of the mirror can very accurately be recorded and simultaneously the intensity of radiation, I(x), falling upon the detector is measured.

The Fourier transform provides the relationship between the distance, x, and intensity I(x) measured in an interferogram and the desired spectral intensity I(ν) at frequency ν. The mathematical equation relating I(ν) to I(x) is

$$I(\nu) = \int_{-\infty}^{\infty} I(x)\cos 2\pi x\nu dx \qquad (1)$$

The resolution capability is $\frac{1}{2\Delta x}$ where Δx represent the path difference and 2Δx is the optical retardation of radiation striking the movable mirror.

FTS has several advantages over dispersive spectroscopy, such as being able to preform Atomic Spectroscopy and Molecular Spectroscopy on the same instrument, as we propose in this research. Fellgett's original work[4] involved a large number of spectral elements impinging upon the detector - hence, the name Fellgett's advantage from this multiplexing of frequencies. The interferometric signal, S, is directly proportional to the observation time, T; while the noise, N is proportional to $T^{1/2}$. Thus, the signal to noise ratio is proportional to $T^{1/2}$. For comparison, in a dispersive instrument each resolution element, M is observed sequentially for an average time T/M. Thus, the noise is proportional to $(T/M)^{1/2}$ and the signal-to-noise ratio to $(T/M)^{1/2}$. Thus, an advantage of $(M)^{1/2}$ is realized for the application of interferometry over the dispersion instrument operated at an equivalent signal-to-noise ratio. This is quite an advantage since routinely $M = 3000$ in dispersion spectroscopy compared to $M = 1$ in interferometry!

Jacquinot's advantage[5] really describes the great throughput ability of the interferometer to accept a large cross-section of radiation. The advantage is easily realized if we compare the 50 mm circular aperature of the interferometer, note there are no slits, to the 0.1 mm^2 slit area of a dispersion instrument operating at 1 cm^{-1} resolution. Comparing these figures, we easily see the throughput advantage of at least 1000 for the interferometer over the dispersion instrument.

Combining Fellgett's and Jacquinot's advantages with other advantages, e.g., computer techniques of curve smoothing and averaging spectra, and the laser ability to very accurately measure the mirror displacement, the resulting advantage of interferometry over dispersive spectroscopy is convervatively 10^2 in sensitivity or signal-to-noise. It is this advantage that we wish to utilize for our studies.

The interferometer we used in this work to obtain has a spectral range from 10,000 to 10 cm^{-1} with at least 0.001 cm^{-1} precision in frequency and to 0.10 cm^{-1} resolution, depending on the beam splitter, detectors and source we choose.

References

1. A. A. Michelson, Phil. Mag. Ser. 5, 31, 256 (1891); A. A. Michelson, Phil. Mag. Ser. 5, 34, 280 (1892); A. A. Michelson, Light Waves and Their Uses, University of Chicago Press, Chicago 1902. (reprinted, Pheonix Science Series, University of Chicago, Press, 1962).

2. P. R. Griffiths, Chemical Infrared Fourier Transform Spectroscopy, Wiley, New York, 1975.

3. R. J. Bell, Introductory Fourier Transform Spectroscopy, Academic Press, New York, 1972.

4. P. B. Fellgett, J. Phys. Radium, 19, 187, 237 (1958); P. Fellgett, Aspen Int. Conf. on Fourier Spect., 1970 (G. A. Vanasse, A. T. Stair, and D. J. Baker, Eds.), AFCRL-71-0019 p. 139.

5. P. Jacquinot, 17^e Congres du GMAS, Paris, 1954; P. Jacquinot, J. Op. Soc. Am. 44, 761 (1959).

II. A description of Time Resolved Spectroscopy

The basic procedures of Fourier Transform Infrared Time Resolved Spectroscopy (TRS) have been described previously by R.E. Murphy,[1] A. Mantz,[2] and G. Mamantov.[3] In this section we have chosen present only a brief overview of this technique.

Time resolved spectroscopy appears to be a potentially useful method for study of transient intermediates and product buildup for time dependent systems. The TRS technique involves the coordination of reaction stimulation, e.g., pulsed laser excitation of gases or stretching and relaxation in polymers, and the recording of the interferogram at some unit time after stimulation. In the cases of gases, for versatility the reaction vessel is designed to allow either emission or absorption studies. Time resolved spectroscopy provides a very attractive means for the elucidation of the structure of reaction intermediates and products because this technique provides sufficient data for examination of the band shapes of materials and deduction of the energy distributions within the molecules for successive times during reaction.

The fundamental difference between TRS and normal FTIR spectroscopy is the source characteristics. In TRS the source has been made time dependent rather than time independent as required for conventional FTIR spectroscopy. Thus in either emission mode or absorption mode, the source intensity has the time dependence of the spectrum of the species created by the stimulation. Figure 1 illustrates a possible energy buildup in a gaseous molecule system after laser stimulation.

One possible assumption is that the intensity at any time t_N after the stimulation is always reproducibly measured. To obtain an interferogram using this assumption for any time, t_N, all that is necessary is an intensity file, I(x), composed of each mirror position at the time t_N after stimulation. At the completion of the experiment the file will contain the total interferogram at time, t_N. This file can be collected by the coordination of the mirror positions to a time - say t_5 - after the stimulation; here the He-Ne laser of the interferometer is used as a clock. The clock counts the number of zero crossings and after the correct number of crossings has occurred, the source is stimulated by a pulse sent from the controlling computer. The same clock is used to open the detector gate when the number of crossings is equal to time interval N which will be five for our example. After collection of these points in the interferogram, the laser flash start is shifted one zero crossing to the right and the above process is repeated until an intensity sample, I(x), is obtained for each mirror position, x. This is illustrated in Fig. 2.

Since TRS is most useful for kinetic studies it would be advantageous to collect data for several time intervals after the stimulation event. This can be done by performing several of the above experiments; however, a more efficient method is available. Every zero crossing after the stimulation event represents a time related position where it is possible to open up the detector gate and record the intensity at some time, t_N, where N is the number of zero crossings after the stimulation event. With adequate storage capabilities, this can be done for as many times, t_N, as there are zero crossings between stimulation events. The final problem which remains when one uses TRS is the manipulation of the accumulated data into separate files for each t_N. The I(x) values for all x at each of the times t_N must be separated from those of the other times, t_j; and finally placed in order according to x value or increasing optical retardation in the file for each t_N. The computer software to do this is available; however, it can severely tax the memory and storage capacity of some laboratory computers.

Once enough data has been collected to adequately describe the interferogram of the transient species, i.e., enough points to satisfy resolution and wavelength range requirements, the Fourier transform of the points can be taken using the equation

$$S(\nu) = 2 \int_{o}^{X} I(x_{t_N}) \cos 2\pi\nu \, xdx \qquad (1)$$

where x is the mirror displacement. The Fourier transform now provides the infrared spectrum of the reactive system at t_N after stimulation.

At this point it would appear that the goal has been reached but Mamantov et al.,[3] have pointed out some serious practical limitations. They have shown that the interpretation of the data from a TRS experiment is, unfortunately, not as straightforward as it would appear. The problems occur when the theory makes certain assumptions which are not true in practice. The most obvious of these assumptions is that the source is exactly reproducible. In the conventional FTIR experiment that isn't a bad assumption, but the close timing that makes the TRS experiment possible places abnormally high reproducibility and accuracy limits on the source.

One of the first problems with the source is its stimulation interval. The flash stimulation interval chosen must consider the reacting compounds since their products are the true source of radiation for operating the interferometer. The stimulation interval must be long enough for one of two things to happen. First, the stimulation interval must be long enough so that the excited species relax back to the initial reactants or long enough so that they are swept out of the optical path by a flow system, i.e., the same flow system which introduces the reactants, before the next stimulation occurs. If this is not done, the interferometer will detect the remnants of this previous stimulation along with the products from the next stimulation. The results of TRS analysis and spectral interpretation of this mixture from different stimulations can be disastrous, see

Ref. 3. If such a mixture does occur, it is very difficult to interpret the spectra obtained.

A second problem involving the source is in the timing of the stimulation pulses. The laser pulse must be stable enough that it will flash at the same time after the trigger pulse, with the same duration, and with the same intensity.

If the stimulation interval is not constant, the entire timing scheme collapses and the results are useless. In the TRS experiment the detector gate will still open at the same time period after the trigger pulse (400 μsec is a reasonable time after trigger) and the computer will make no compensation nor does it have any way to correct the signal for the change with respect to the stimulation event in the time period when the detector gate is open. The net effect is a broadening of the time period represented from 400 μsec to 400 μsec plus the detector gate to 400 μsec to 400 μsec plus the pulse accuracy.

Another problem occurs when the duration of the stimulation is variable, for the distribution curve of the species in their excited states will change. The same thing happens when the source intensity is variable, although the distribution curve will probably look different than from the one for stimulation duration. The net effect of both is the same. The light source appears variable to the interferometer which is exactly the reason we cannot run a normal TRS study of a time dependent system. The distortion in the spectrum from the changing intensity has been documented by Mamantov et al., Ref. 3 for systems of changing concentration. The distortion causes false absorption and/or emission peaks in the transformed spectrum. This phenomenon is always observed in systems which have changing intensity or flash stimulation duration variation.

A final problem lies in the physical design of the optical path. Simply because the detector gate is opened at some time after the stimulation, there is no assurance that the resulting data is from that stimulation interval only.

For example, if the reaction occurs in a flowing system as we propose here, it is very probable that the species representing the time period of interest has been swept down the tube and out of the optical path. Of course, this can be easily corrected by placing the observation point at the correct distance from the stimulation device. This correction applies only to some distinct time period, t_N, as determined by the flow rate. Thus any other information about another time period, t_j, will be inaccurate. In other words, all advantages from being able to monitor several different time periods are lost.

Additional complications are introduced by the interferometer if it is unstable. Much of the instability can be removed by the application of isothermal conditions within all components in the optical path.

In summary TRS has some possible pitfalls, some we now know while others lie ahead. But most important, the field of TRS holds a significant potential for the understanding of transient intermediates. We are most encouraged by the experiment we have concluded with TRS which were supported by AFOSR and wish to apply this technique to further studies.

Further we have been studying polymer films undergoing stretching and relaxation. The result from these studies are very encouraging and are reported in section IV. We feel TRS is now a reality and much new structural information will be won from studies on nonequilibrium systems.

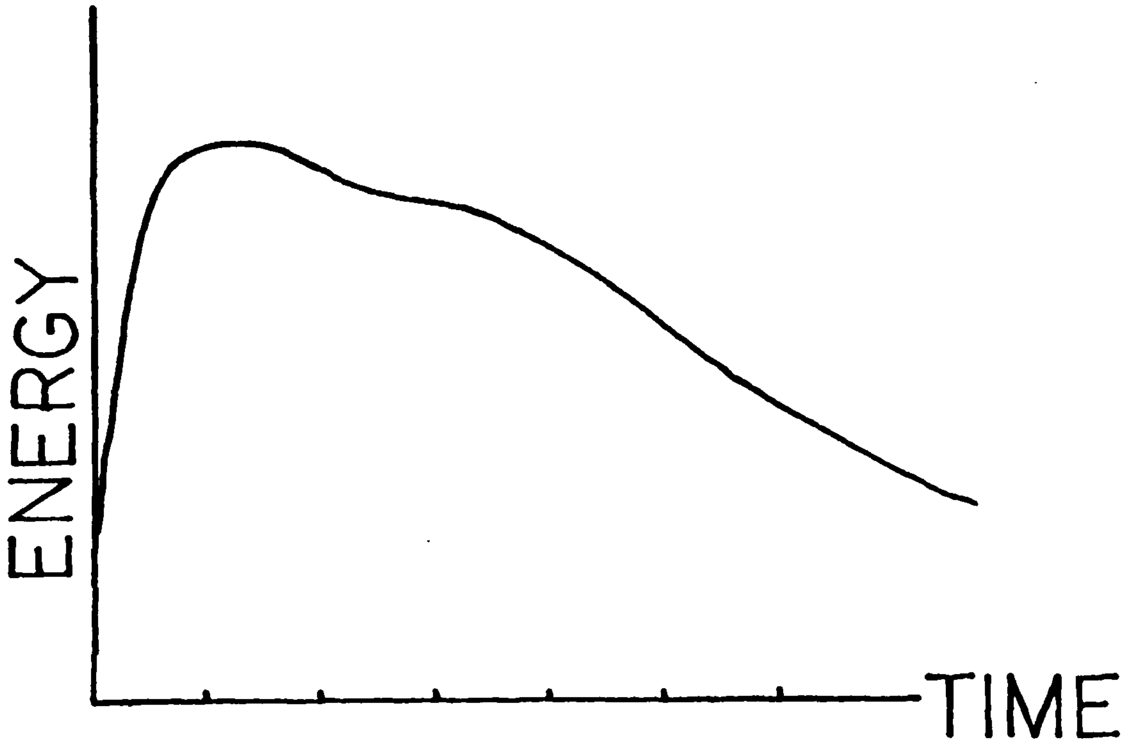

Fig. 1 Possible Energy Diagram of a Molecular System after Excitation

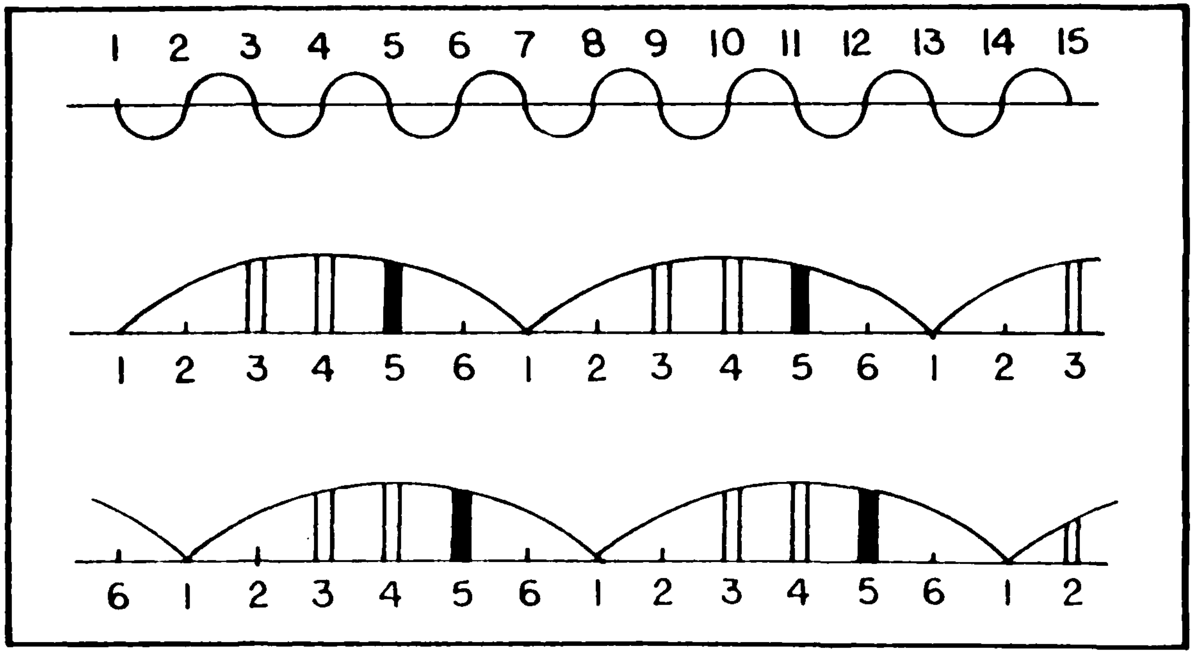
1 2 3 4 5 6 7 8 9 10 11 12 13 14 15
1 2 3 4 5 6 1 2 3 4 5 6 1 2 3
6 1 2 3 4 5 6 1 2 3 4 5 6 1 2

Fig. 2 Diagram of a TRS Collection

This shows three files N = 3, N = 4, N = 5 being collected at a stimulation period of six zero crossings. Collection file N = 5 is shaded. Each file will be collected until all positions (numbered above) have been recorded with a stimulation from each file.

Continuation of Caption for Fig. 2

A. is a plot of zero crossings by the He-Ne laser showing intensity as a function of optical retardation and time.

B. is a plot of two complete and one fractional stimulation intervals and the resulting source intensity as a function of optical retardation and time with time numbered with 1 corresponding to the start of a new stimulation interval.

C. is a plot of one fractional, two complete and one fractional stimulation interval and the resulting source intensity as a function of optical retardation and time with time numbered with 1 corresponding to the start of a new stimulation interval.

Note the optical retardation scale is the same in both B and C but the stimulation interval is moved one zero crossing or 628 nm of optical retardation to the right along the optical retardation scale. Thus the N=5 file (5 zero crossings after the start of a new stimulation interval) is moved from the optical retardation position corresponding to 5 in A for experiment B to the optical retardation position corresponding to 6 in A for experiment C.

References

1. R. E. Murphy, F. Cook, and H. Sakai, *J. Opt. Soc. Am.*, *65*, 600 (1975).
2. A. W. Mantz, *Appl. Spectrosc.*, *30*, 459 (1976). J. F. Durana and A. W. Mantz, Chapter 1, *Fourier Transform Infrared Spectroscopy*, Vol. 2, Ed. J. R. Ferraro and L. J. Basile.
3. A. A. Garrison, R. A. Crocombe, and G. Mamantov, and J. A. de Haseth, *Appl. Spectrosc.*, *34*, 399 (1980).

III. Some Optimizing Conditions for Time Resolved Spectroscopy

The instrumental parameters necessary to collect high quality infrared spectra by Fourier transform interferometry have been adequately described in the recent literature; however, many of the operational parameters necessary for time resolved studies have not been reported.[1] Relationships are discussed here between number of data points, undersampling ratio, resolution, spectral region limits, data files needed, and flash periods, or in the case of polymers, stretching periods. The necessary equations relating instrument parameters which must be optimized to obtain good spectra are presented.

First, in the description of time resolved spectroscopy (TRS) trading rules and their maximization, it is necessary to describe certain terms. These abbreviations may differ for various instruments; however, the definition of the terms will remain the same. For example RES means resolution for most commercial instruments. The following terms were used in our past experiments.

Terms

NPT - number of data points

UDR - undersampling ratio; 1,2,3...etc.

RES - resolution, cm^{-1}

RNG - free spectral range

NTD - number of files to do

FPD - stimulation period

SEP - time separation of interferogram

FFI - stimulation increment

"Trading Rules"

The fundamental difference between TRS and normal FTIR is the time dependence of the intensity in addition to the normal frequency dependence of intensity. To change a time dependent source into a time independent source the technique of strobing is used. In fact a more proper name of this technique would be Stroboscopic Interferometry. The interferometer's detector is strobed allowing only the light of one particular time t_n for a specific width in time to reach the detector. This make the source appear quasi time independent and allows the FTIR collection to proceed normally.

If t_n and the time width were the only experimental parameters necessary for the TRS experiments, experimentation would be very simple. However, this is only the initial parameter from a group of some fairly complex instrumental conditions which must be described for successful experiments. In addition to the instrumental parameter, the chemistry of the sample can play an important role in the choice of experimental parameters.

The initial interest for setting the instrumental parameters is directed to the chemical system to determine the reaction period which will capture important portions of the chemical reaction immediately following laser or ultraviolet stimulation. We note at this point that similar consideration is given to the frequency of stretching certain polymer films and the situation is analogous. The reaction period is not the rate at which the excitation source (e.g. pulsed laser, uv lamp, mechanical deformation, etc) can be reproducibly cycled; rather reaction period is the time which it takes the sample to be displaced from equilibrium and either fully recover and return to its original equilibrium condition; or, in the case of decomposition, go to another equilibrium configuration. If the sample does not recover from excitation (destructive photolysis, the breaking of polymers, etc) the reaction period must be equal to the time necessary to remove the old sample and replace it with an identical new sample. If this does not occur the technique is invalidated.[2]

While at this point it seems desirable to make the reaction period quite long from the viewpoint of the sample other experimental parameters require that the reaction period be as rapid as possible. The number of files to do (NTD) becomes prohibitively large as the stimulation period becomes longer. Rule number one gives the exact relation.

Rule #1 $NTD = \frac{FPD}{FFI}$

where NTD is the number of files to do

FPD is the reaction period

FFI is the stimulation increment

The problem with having a large numer of files to do (NTD) is basically a data problem. As the number grows larger not only are there more files to save, requiring more disk space, but there are also more files to sort through when the computer is creating the time resolved files. The time required for this sort is relatively short (on the order of minutes) for small numbers to do (NTD) like 8 or 10, but it reaches several hours for 100 files and it essentially takes days for larger numbers.

One last reaction period consideration is the total time required for the experiment. As the reaction period becomes longer, naturally more time is used not only in collecting the files, but also for switching between the files. All of this adds up to more chemical reagents necessary to flow through the system. This can become very expensive. Another consideration is that the longer the experiment runs, the more likely that the source stability or interferometer stability will degrade leading to non-reproducible results and invalidating the TRS technique.

The next difficult choice for the instrumental parameters would be the proper undersampling ratio (UDR). The spectral folding properties of the undersampling ratio are well known.[2] This relationship is shown by Rule #2.

Rule #2 $RNG = \frac{15800.8}{UDR_I}$

where RNG is the free spectral region and 15800.8 cm^{-1} is the Ne reference laser in air. UDR_I is the undersampling ratio initially

Due to this effect most normal FTIR experiments are done at UDR=2. One finds in the time resolved experiment there is much more importance attached to the UDR value.

For example the UDR determines the time separation for each of the files. Here one finds it is important to minimize the value of UDR. Rule number three demonstrates this effect.

Rule #3 $SEP = UDR_I \times 100\mu s$

where SEP is the time separation of interferogram and 100μs is the time separating the Reference laser fringes

Directly competing with rule number three is the effect the undersampling ratio, UDR, has on the total number of data points (NPT) as shown in rule number 4.

Rule #4 $NPT = \frac{2 \times 15800.8}{(UDR_I)(RES)}$

where NPT is the number of data points

UDR_I is the undersampling ratio initially

RES is the resolution

The total number of points represents the number of times the transient effect is repeated. There are several reasons that make it desirable to minimize this number; and, hence, maximize the UDR. The most obvious reason is that if the sample can only undergo a set number of excitations before being degraded, that number cannot be exceeded and should not even be closely approached. A related factor which must be considered is the coaddition advantage when one wishes to achieve a higher signal to noise. For every $\sqrt{2}$ increase in the signal to noise the number of points taken doubles. This can very rapidly place sample perturbations in the thousands to hundred thousands. The time necessary to perform the experiment becomes very important in this consideration.

If these were the only two competing UDR effects the choice would be fairly simple, but the UDR also controls the free spectra range. Not only is the spectra range limited to that shown in Rule #2, but the frequency of the initial and final points are also fixed by the relationship which modifies Rule 2.

Rule #2a

Frequency of the first point = $\frac{15800.8}{\text{UDR}} \times 2N$

Rule #2b

Frequency of the last point = $\frac{15800.8}{\text{UDR}} \times (2N \pm 1)$

where N is any integer. This results in some desired spectral ranges becoming ursable since they fold in the data over the end points.

One final complication is the value for the stimulation increment, FFI, or in other words the offset staggering of the strobes to the mirror positions. On the Digilab® instrument, FFI is equal to the UDR which sometimes places an additional strain on experimental parameters. The stimulation increment does not theoretically have to be equal to the initial undersampling ratio, but it must be equal to the final undersampling ratio, UDR, of the sorted time files as shown by Rule number 5.

Rule #5

$\text{UDR}_F = \text{FFI}$

where UDR_F is the final undersampling ratio

If FFI is independent of UDR_I, then there is a simple tradeoff between the spectral folding and the number to do, NTD, as shown in rules number one and five. When FFI = UDR_I all of the rules given depend upon the UDR chosen.

With all of the prejudices being placed upon the values of the same experimental parameters it is important to resolve the problem of experimental conditions in a common sense manner. The following choices must be made and the logic for each decision is discussed in terms of gains and losses.

The first choice must be the chemical system to be observed. While this is generally dictated by the research program, the experimentalist should keep in mind that the more reproducible the effect the fewer sample perturbations will be required to give spectra without strobiscopic aliasing of spectra. The experiments should be in a realistic time frame with the expected output data. Time separations of 100μs are fairly easily obtained, but data faster than that is difficult to do and requires the researcher to place extraordinary attention on reproducibilities and the large amount of signal averaging. Resolution is related to several variable parameters and can be any value desired; however, systems with low resolutions provide the best time periods for the experiment. The same argument goes for the free spectral region one wishes to study. Reaction systems with smaller spectral ranges will yield better results and reflect smaller and more identifiable noise.

References

1. See references 1, 2, and 3 in Appendix A.2.
2. D. E. Honigs, R. M. Hammaker, and W. G. Fateley in "Analytical Applications of FT-IR to Molecular and Biological Systems," ed. by J. R. Durig, Reidel, Boston (1980) pp. 89-118.
3. See reference 3 in Appendix A.2.

IV. Some Preliminary Time Resolved Results

To elucidate the changes in molecular structure of polypropylene film during stretching and relaxation, we chose to use Time Resolved Fourier Transform Infrared Spectroscopy. The films were stretched and relaxed at 10 hertz cycles in the direction parallel to the C-axis of the polypropylene helix.* The percentage stretches were approximately 5%. To interrogate the nonequilibrium molecular structure, the infrared spectrum was collected over a 10 microsecond time interval every 10 milliseconds. The results are shown in Figures 1a, 1b, 2a, 2b, 3a and 3b. The spectra indicate some vibrational frequencies change only in intensity while other vibrations change in frequency and intensity.

There is no apparent frequency shifts in the spectra shown in Figures 1a, 1b, 2a and 2b because these vibrations represent local modes in polypropylene which one would expect not to be sensitive to elongation. However, there are intensity changes in those absorptions (see Figures 1a and 1b), which represent molecular modes which are sensitive to changes in crystallinity in polypropylene. The main spectral frequency change comes from the CH_2 groups which form the helix. These frequencies both shift and change intensity, note especially Figures 3a and 3b. The following conclusions could be reached:

a) There are vibrational frequencies originating from local modes which are unaffected by stresses which change the helix's dimensions.

b) Those vibrations of CH_2 groups in the helix demonstrate non-equilibrium structural changes in the microsecond time scale.

c) Some intensity changes can be interpreted as increases or decreases in crystallinity.

---

*The polypropylene films and x-ray characterizatins were provided by Dr. John Rabolt, IMB, San Jose, California.

In this experiment the Digilab® Model 296 interferometer was used. The TRS unit provided by Digilab® has undergone numerous electronic modifications which were necessary for satisfactory experimentation operation. A globar infrared source, typical of those used so successfully by Perkin Elmer Instrument for twenty years, was placed so as to illuminate the polymer film. The polymer film was stretched by a modified solenoid taken from an automobile starter. The stretching-relaxation, which is approximately 10 hertz, is controlled by the time clock of the interferometer. The infrared spectra are collected for 10 microseconds before stretching begins, then the structure is interrogated for 10 microseconds at periods of 10 milliseconds, 20 milliseconds during stretching and 30 milliseconds and 40 milliseconds during relaxation. The complete experimental details of the application of time resolved spectrscopy is the subject of a paper which is now in preparation. A mercury-cadmium-telluride detector was used with a CaF_2 beam splitter. A summary of this study and the time periods involved is given in Table 1.

The 3000 cm^{-1} region was investigated but the polymer films were too opaque in this region. Now new films have arrived which are thin enough to allow observation in the 3000 cm^{-1} carbon-hydrogen stretching region. The region below 1300 cm^{-1} was inaccessible because of the CaF_2 beam splitter used in this experiment.* Future experiments will employ KBr beam splitters and different optical filters.

---

*The instrument is shared with Professor Setser and his work demands this beam splitter region.

Table 1

The time periods and spectral range used in this experiment

Time Period*	Region, cm^{-1}	Figure
A. Stretching Cycle		
0	1500-1400	1a, curve #1
	1400-1300	2a, curve #1
	1325-1275	3a, curve #1
10 ms	1500-1400	1a, curve #2
	1400-1300	2a, curve #2
	1325-1275	3a, curve #2
20 ms	1500-1400	1a, curve #3
	1400-1300	2a, curve #3
	1325-1275	3a, curve #3
B. Relaxation Cycle		
30 ms	1500-1400	1b, curve #4
	1400-1300	2b, curve #4
	1325-1275	3b, curve #4
40 ms	1500-1400	1b, curve #5
	1400-1300	2b, curve #5
	1325-1275	3b, curve #5

*Time period measured from the initiation of the stretching

Figure Captions

Figure 1a. Infrared spectrum from 1500 to 1400 cm^{-1} of polypropylene film during stretching. Curve No. 1 is the 10 microsec spectrum taken before stretching. Curve No. 2 is the 10 microsec spectrum at 10 millisec after film stretching began. Curve No. 3 is the 10 microsec spectrum at 20 millisec after stretching began. The stretching frequency is approximately 10 hertz.

Figure 1b. The infrared spectrum from 1500 to 1400 cm^{-1} of polypropylene film during relaxation. No. 3 is a repeat of the same spectrum as shown in Fig. 1b. Curve No. 4 is taken during film relaxation approximately at 30 millisec after the initiation of stretching. Curve No. 5 is again during relaxation approximately at 40 millisec after the initiation of stretching.

Figure 2a. The infrared spectrum from 1400 to 1300 cm^{-1} of polypropylene film during stretching. Time periods for curves 1, 2 and 3 are defined in Figure 1a.

Figure 2b. The infrared spectrum from 1400 to 1300 cm^{-1} of polypropylene film during relaxation. Time period for curves 3, 4 and 5 are defined in Figure 1b.

Figure 3a. The infrared spectrum for 1325 to 1275 cm^{-1} of polypropylene film during stretching. The presentation has been expanded to better evaluate the spectra. Time periods of curves 1, 2 and 3 are defined in Figure 1a.

Figure 3b. The infrared spectrum from 1325 to 1275 cm^{-1} of polypropylene film during relaxation. The scale is the same as in Figure 3a. Time period of 3, 4 and 5 are defined in Figure 1b.

FIG 1A

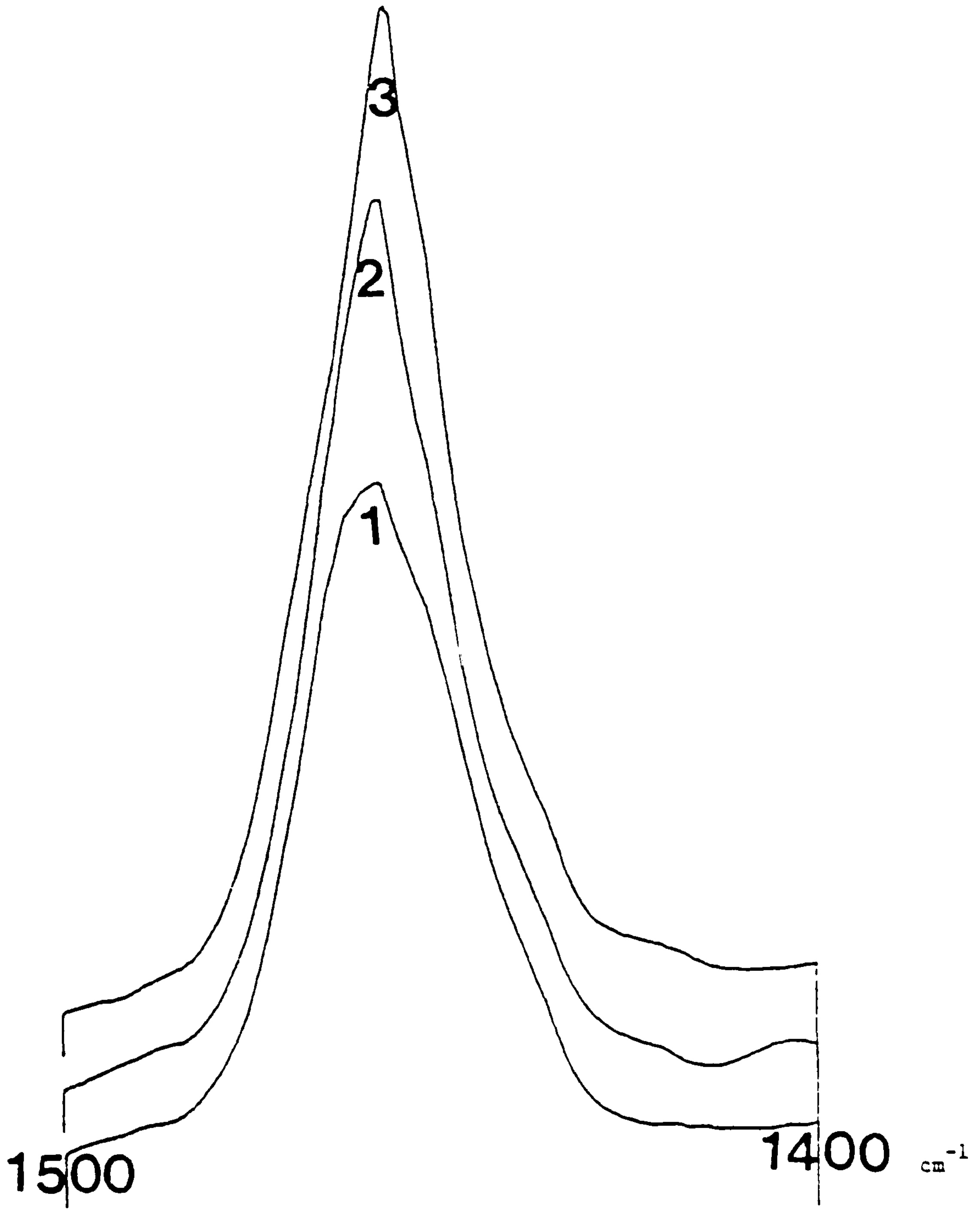

FIG 2A

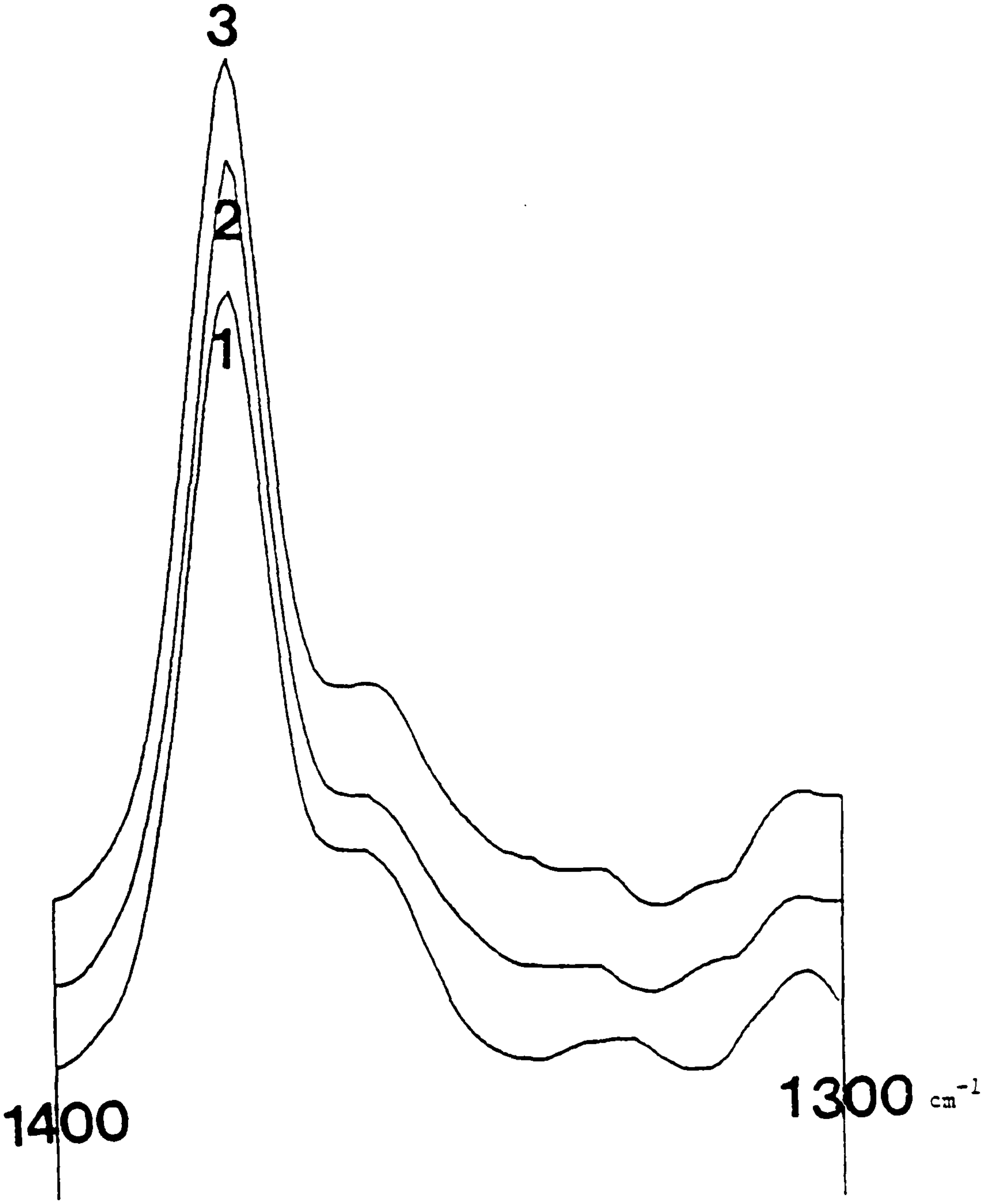

FIG 3A

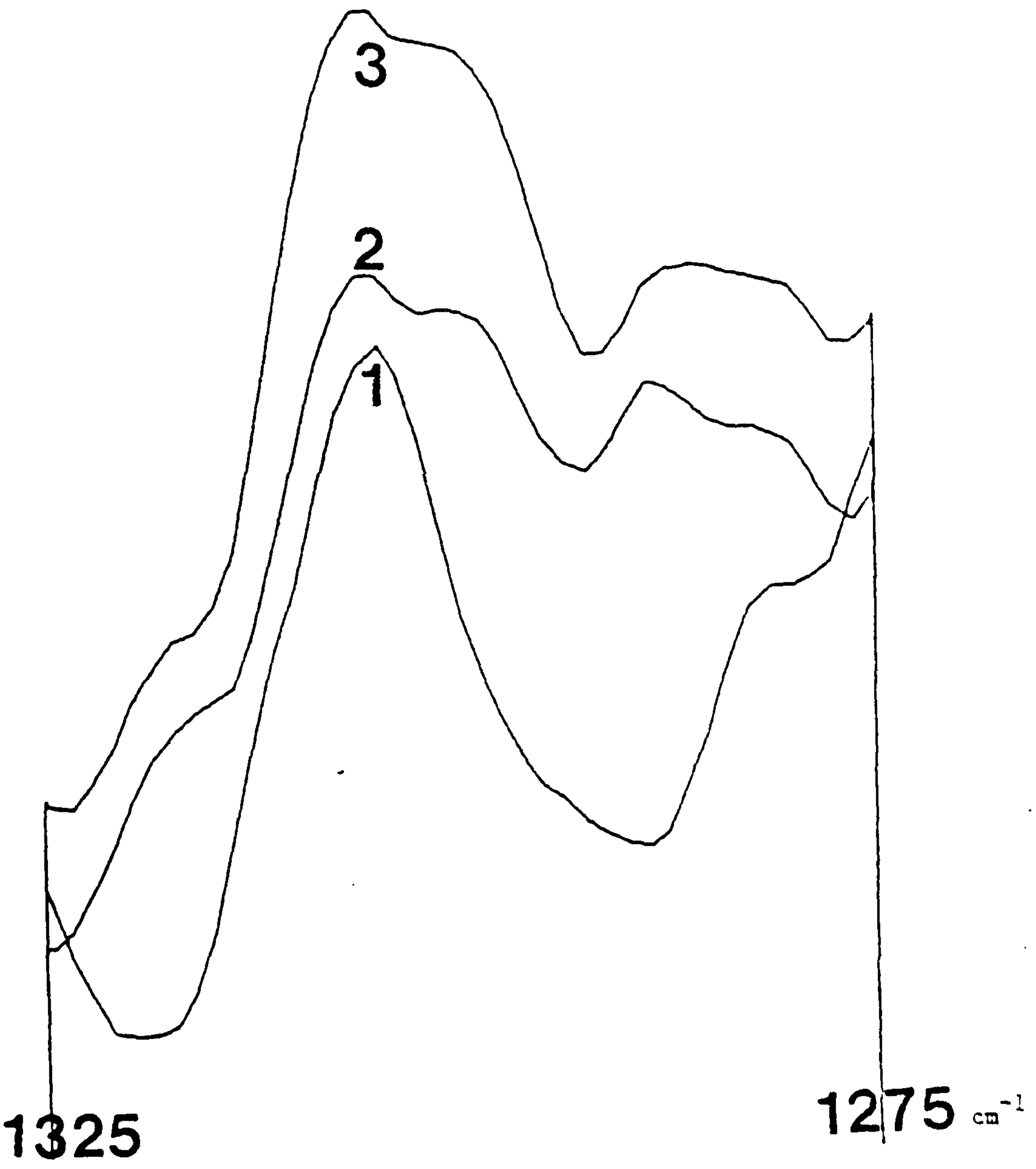

FIG 1B

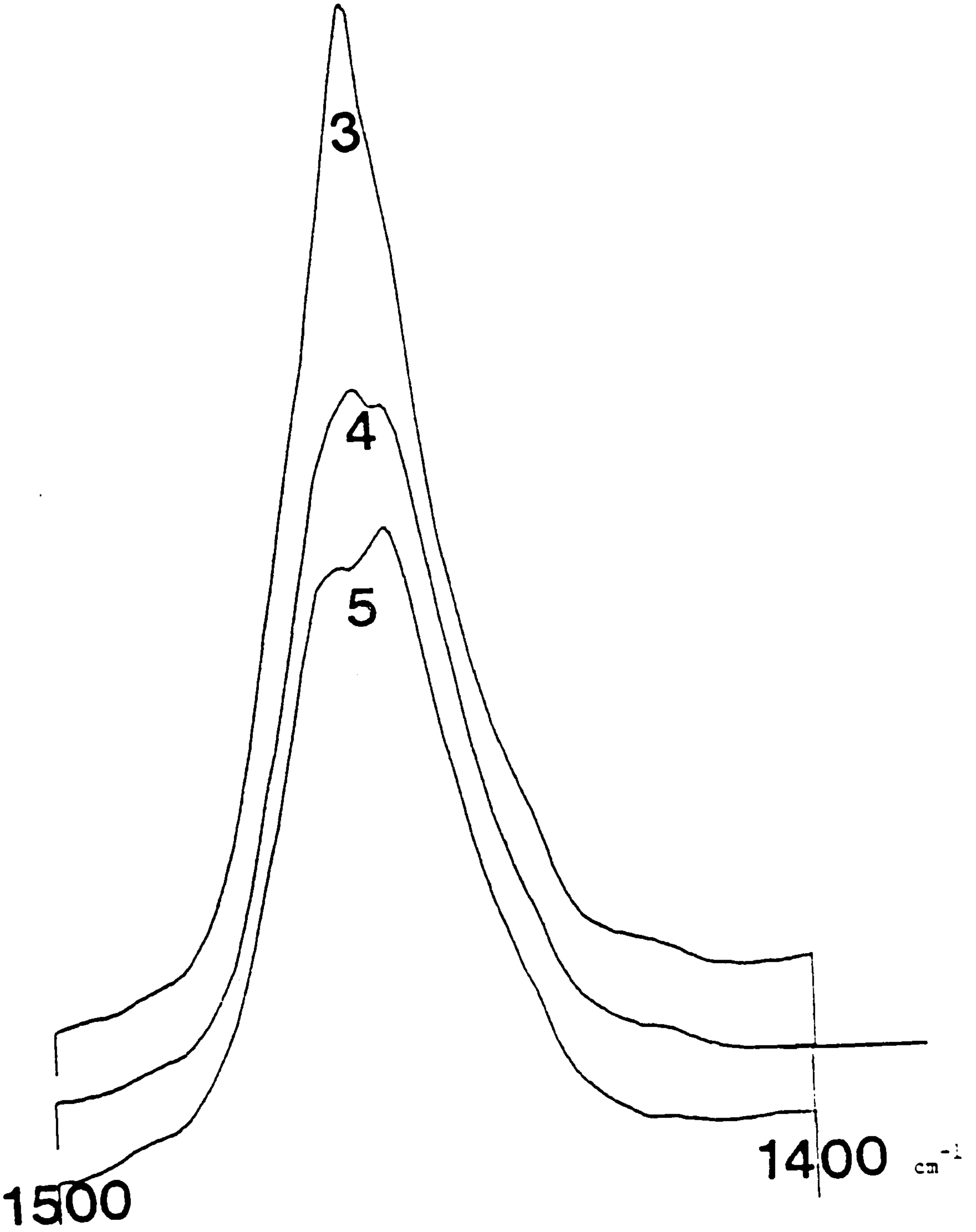

FIG 2B

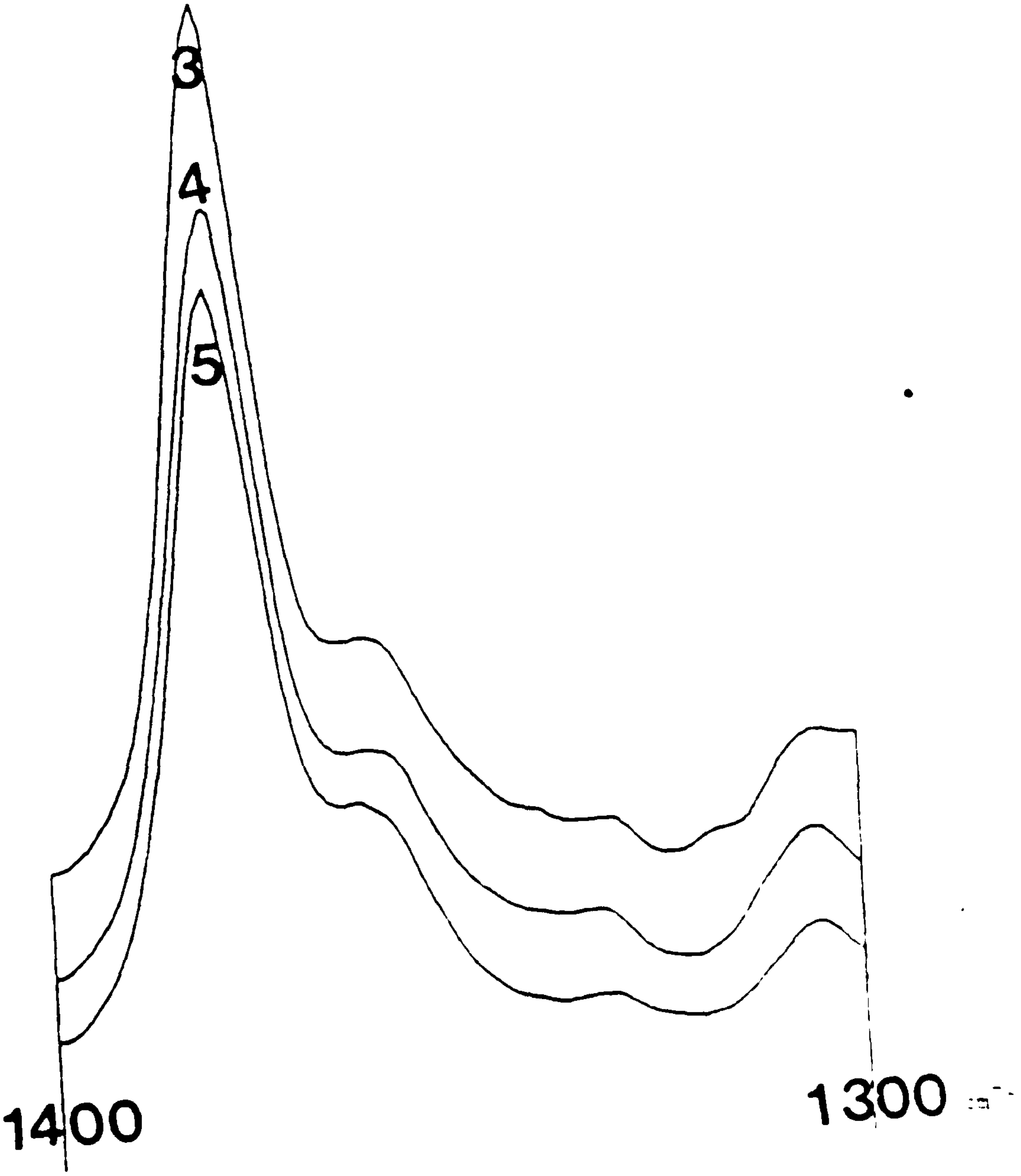

FIG 3B

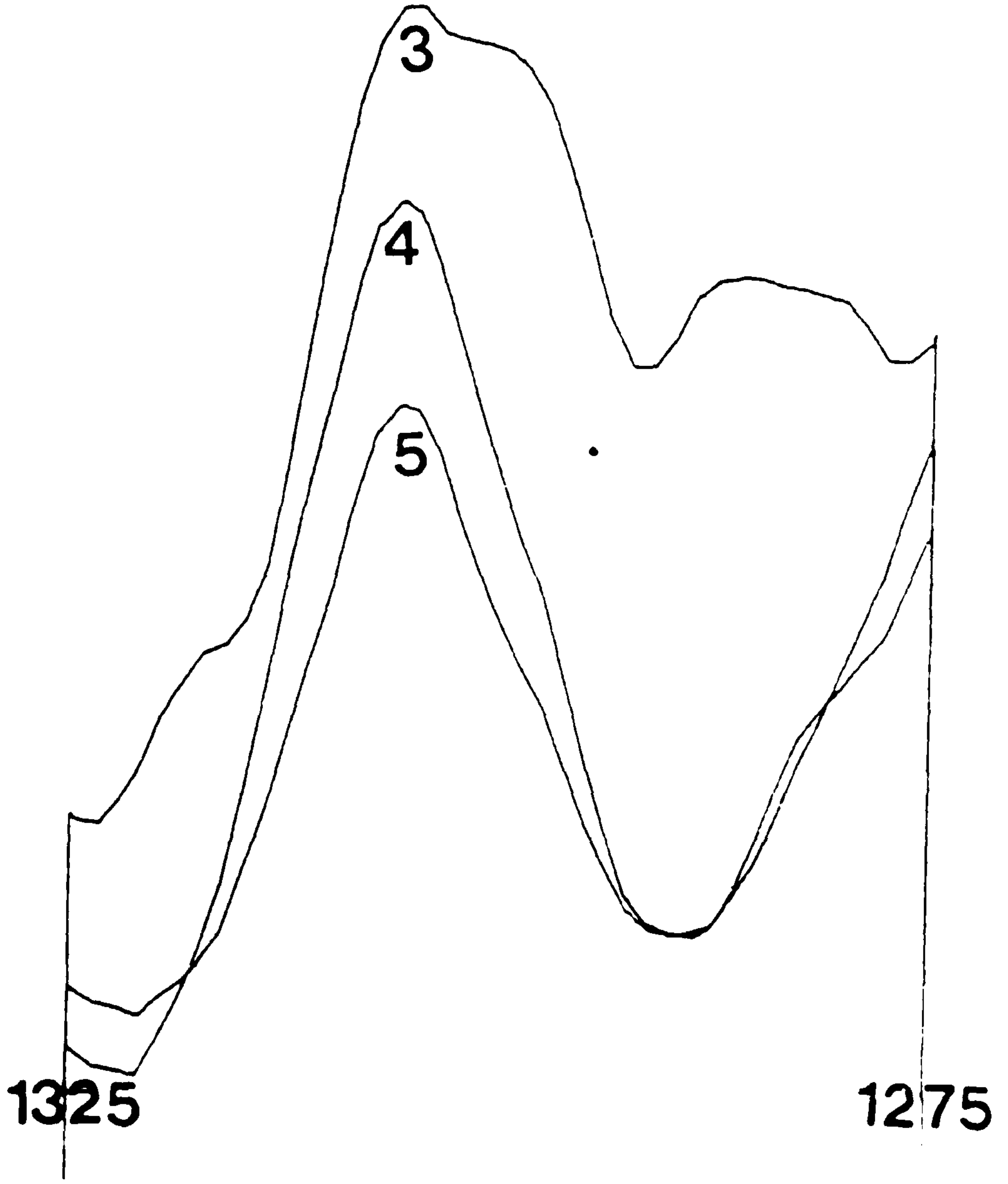

In summary, it is apparent that we are observing the infrared spectrum of the polymer under non-equilibrium condition of stretching and relaxation. Further studies of polyethylene, and polytetrafluoroethylene show similar spectral effects. Additional research is needed to elucidate the polymer structure at nonequilibrium condition. The most important study has not yet been performed. We wish to stretch-relax the polymer films until failure of the polymer film occurs, i.e., the polymer film breaks. We will then analyze the spectra of the polymer during stress past prior failure in an effort to identify what molecular changes occur. We feel this information will be very important in understanding polymer structural failure.

V. Publications, Seminars and Talks During the Period of the Grant

A. Publications

1. "Raman Spectroscopy", W. G. Fateley and F. F. Bentley, Encyclopedia of Physics, 1980.

*2. "Raman Spectra of the Adduct Structure of Cl_2 and Br_2 with Piaselenole", J. J. Blaha, W. Brittain, C. E. Meloan and W. G. Fateley, Appl. Scpectrscopy, 23, 636 (1980).

*3. Chapter "Hadamard Transform Spectrscoy", C. S. Bartholomew, G. W. Fateley and N. P. Murarka, NATO Advance Study Institute on Analytical Application of FTIR, J. R. Durig, Editor, Aug. 1980.

*4. Chapter "Time Resolved Spectroscopy", D. E. Honigs, R. M. Hammaker and W. G. Fateley, NATO Advance Study Institute on Analytical Application of FTIR, J. R. Durig, Editor, Aug. 1980.

*5. Chapter "One View of the Advantages of Infrared Interferometry", J. C. Case and W. G. Fateley, NATO Advance Study Institute on Analytical Application of FTIR, J. R. Durig, Editor, Aug. 1980.

6. "Vibrational Spectra and Normal Coordinate Analyses of CF_3OF and CF_3OCl, J. D. Kuo, D. D. DesMarteau, W. G. Fateley, R. M. Hammaker, C. J. Marsden and J. D. Witt, J. Raman Spectrosc., 9, 230, 1980.

*7. Chapter "Non-traditional Matrix Isolation: Adducts", NATO Advanced Study Institute on "Matrix Isolation Techniques", Orville-Thomas, Eidtor, Fall 1980.

8. "The CF_3 Rotor: Torsional Vibrationas for Some CF_3OX and CF_3OOX Molecules", R. M. Hammaker, W. G. Fateley, Ajit S. Manocha, and D. D. DesMarteau, J. Raman Spectrosc., 9, 181, 1980.

*Papers related to and sponsored by this grant.

In Preparation:

Due to the large amount of descriptions, discussion and data, we have chosen to publish the results from TRS in a chapter now under preparation. The Editor, Professor J. R. Durig, has scheduled this chapter to be published in the summer of 1981.

B. Seminars and Talks

Invited Lectures on TRS by R. M. Hammaker and W. G. Fateley

Foreign invitations to lecture on this subject

1. England
2. Germany
3. France
4. Italy

Future Lectures, Fall 1981

1. Japan
2. Korea

United States

1. St. Louis, SAS and ACS
2. Pittsburgh, JSP
3. Union Carbide, South Charlestown, W. VA
4. Oklahoma State
5. Pittsburgh Conference
6. MASUA Speaker
7. NBS

VI. Summary

Although this report represents a period of one year it actually summarizes the total period of research sponsored by the Air Force, Office of Scientific Research. This grant provided support to (1) develope time resolved infrared interferometry, and (2) demonstrate the use of time resolved spectroscopy on chemical systems. Both of these goals have been accomplished.

The research reported herein demonstrates the excellent application of time resolved spectroscopy to dynamic conditions in polymers. Certainly the next extension of this research will be to the structure of polymers just prior to polymer failure. We feel this technique will be a very excellent diagnostic tool to the better understanding of polymer failure under stress.

We greatly appreciate the Air Force, Office of Scientific Research's support and the tremendous help, cooperation, encouragement, and understanding of Mr. Denton Elliot during this research period.

VII. Acknowledgments

I gratefully acknowledge the support of the Air Force, Office of Scientific Research for their three year support to develop Fourier Transform Time Resolved Spectroscopy. I am especially indebted to Mr. Denny Elliot for his support and very kind encouragement.

VIII. Manuscripts, Preprints and Papers Sponsored by AFOSR Under this Grant

A. Time Resolved Spectroscopy

B. One View of the Advantage of Infrared Interferometry

C. Hadamard Transform Spectroscopy

D. Raman Studies of the Adduct Structure of Cd_2 and Br_2 with Piaselenole

E. The CF_3 Rotor: Torsional Vibrations for Some CF_3OX and CF_3OOX Molecules

F. Vibrational Spectra and Normal Coordinate Analysis of CF_3OF and CF_3OCl

Chapter[†]

A. Time Resolved Spectroscopy[*]

D. E. Honigs, R. M. Hammaker and W. G. Fateley

Department of Chemistry
Kansas State University
Manhattan, Kansas 66506

The basic procedures of Fourier Transform Infrared Time Resolved Spectroscopy (TRS) have been described previously by R. E. Murphy,[1] A. Mantz,[2] and G. Mamantov.[3] In this chapter we have chosen to present only a brief overview of this technique.

Time resolved spectroscopy appears to be a potentially useful method for study of intermediates and products of gas phase reactions. The TRS technique involves the coordination of reaction stimulation, e.g. pulsed flash photolyses, laser excitation, or some other periodic reaction initiating techniques, and the recording of the interferogram at some unit time after stimulation. For versatility the reaction vessel may be designed to allow either emission or absorption studies. Time resolved spectroscopy provides a very attractive means for the elucidation of the structure of reaction intermediates and products because this technique may provide sufficient data for examination of the band shapes of materials and deduction of the energy distributions within the molecules.

The fundamental difference between TRS and normal FTIR spectroscopy is the source characteristics. The source in this discussion may be the emission spectrum from the species created by the stimulation or a time independent source modulated by the absorption spectrum of the species created by the stimulation. In either case the source has been made time dependent rather than time independent as required for conventional FTIR spectroscopy. Thus in either emission mode or absorption mode, the source intensity has the time dependence of the spectrum of the species created by the stimulation.

---

[*] Work Sponsored by AFOSR, Grant No. AFOSR 78-3617

[†] D. E. Honigs, R. M. Hammaker and W. G. Fateley, "Analytical Applications of FT-IR to Molecular and Biological Systems", Preceedings of the NATO Advanced Study Institute, Florence, Italy, 1980, Editor, J. R. Durig. A. Reidel Publ. Co., 1980.

Fig. 1 illustrates a possible energy build up in a molecular system after stimulation. One assumption is that the intensity at any time t_N after the stimulation is always reproducibly measured. To obtain an interferogram using this assumption for any time t_N, all that is necessary is an intensity file, I(X), composed of each mirror position at time t_N after stimulation. At the completion of the experiment the file will contain the total interferogram at time t_N. This file can be collected by the coordination of the mirror positions to a time - say t_5 - after the stimulation; here the He-Ne laser of the interferometer is used as a clock. The clock counts the number of zero crossings and after the correct number of crossings has occurred, the source is stimulated by a pulse sent from the controlling computer. The same clock is used to open the detector gate when the number of crossings is equal to time interval N which will be five for our example. After collection of these points in the interferogram, the flash start is shifted one zero crossings to the right and the above process is repeated until an intensity sample, I(X), is obtained for each mirror position, X. This is illustrated in Fig. 2.

Since TRS is most useful for kinetic studies, it would be advantageous to collect data for several time intervals after the stimulation event. This can be done by performing several of the above experiments; however, a more efficient method is available. Every zero crossing after the stimulation event represents a time related position where it is possible to open up the detector gate and record the intensity at some time, t_N, where N is the number of zero crossings after the stimulation event. With adequate storage capabilities, this can be done for as many times, t_N, as there are zero crossings between stimulation events. The final problem which remains when one uses TRS is the manipulation of the accumulated data into separate files for each t_N. The I(X) values for all X at each of the times t_N must be separated from those of the other times, t_j; and finally placed in order according to X value or increasing optical retardation in the file for each t_N. The computer software to do this is available; however, it can severely tax the memory and storage capacity of some laboratory computers.

Once enough data has been collected to adequately describe the interferogram of the transient species i.e., enough points to satisfy resolution and wavelength range requirements, the Fourier transform of the points can be taken using the equation

$$S(\nu) = 2\int_0^X I(X_{t_N}) \cos 2\pi\nu X dX$$

where X is the maximum mirror displacement

The Fourier transform now provides the infrared spectrum of the reactive system at t_N after stimulation.

At this point it would appear that the goal has been reached but Mamantov et al.,[3] have pointed out some serious practical limitations. They have shown that the interpretation of the data from a TRS experiment is, unfortunately, not as straightforward as it would appear. The problems occur when the theory makes certain assumptions which are not true in practice. The most obvious of these assumptions is that the source is exactly reproducible. In the conventional FTIR experiment this isn't a bad assumption, but the close timing that makes the TRS experiment possible places abnormally high reproducibility and accuracy limits on the source.

One of the first problems with the source is its stimulation interval. The flash stimulation interval chosen must consider the reacting compounds since their products are the true source of radiation for operating the interferometer. The stimulation interval must be long enough for one and, hopefully, two things to happen. First, the stimulation interval must be long enough so that the excited species are swept out of the optical path by a flow system before the next stimulation occurs. If this is not done, the interferometer will detect the remnants of this previous stimulation along with the products from the next stimulation. The results of TRS analysis and spectral interpretation of this mixture from different stimulations can be disastrous, see ref. 3. If such a mixture does occur, it is not possible to interpret the spectra obtained.

A second problem involving the source is in the timing of the stimulation pulses. The electrical pulse or flash device must be stable enough that it will flash at the same time after the trigger pulse, with the same duration, and with the same intensity.

If the stimulation interval is not constant, the entire timing scheme collapses and the results are useless. In the TRS experiment the detector gate will still open at the sime time period after the trigger pulse (400 μsec is a reasonable time after trigger) and the computer will make no compensation nor does it have any way to correct the signal for the change with respect to the stimulation event in the time period when the detector gate is open. The net effect is a broadening of the time period represented from 400 μsec to 400 μsec plus the detector gate to 400 μsec to 400 μsec plus the pulse accuracy.

Another problem occurs when the duration of the stimulation is variable, for the distribution curve of the species in their excited states will change. The same thing happens when the source intensity is variable, although the distribution curve will probably look different than from the one for stimulation duration. The net effect of both is the same. The light source appears variable to the interferometer which is exactly the reason we cannot run a normal FTIR study of a time dependent system. The distortion in the spectrum from the changing intensity has been documented by Mamantov et al ref. 3 for systems of changing concentration. The distortion causes false absorption and emission peaks to be plotted so the spectrum shows both absorption and emission spectra components. This phenomenon is also what occurs for systems of changing intensity or flash stimulation duration.

A final problem lies in the physical design of the optical path. Simply because the detector gate is opened at some time after the stimulation, there is no assurance that the resulting data is from that stimulation interval only.

For example, if the reaction occurs in a flowing system, it is very probable that the species representing the time period of interest has been swept down the tube and out of the optical path. Of course, this can be easily corrected by placing the observation point at the correct distance from the stimulation device. This correction applies only to some distinct time period, t_N, as determined by the flow rate. Thus any other information about another time period, t_j, will be inaccurate. In other words, all advantages from being able to monitor several different time periods are lost.

Additional complications are introduced by the interferometer if it is unstable. Much of the instability can be removed by the application of isothermal conditions within all components in the optical path.

On balance, TRS has many possible pitfalls. Some have been located. Even more probably lie ahead. The field of TRS holds a significant potential, but at this time any time resolved spectra must be interpreted with the utmost caution and skepticism.

References

1. R. E. Murphy, F. Cook, and H. Sakai, J. Opt. Soc. Am., 65, 600 (1975).
2. A. W. Mantz, Appl. Spectrosc., 30, 459 (1976).
3. A. A. Garrison, R. A. Crocombe, and G. Mamantov, and J. A. de Haseth, Appl. Spectrosc., July - Aug. issue 1980.

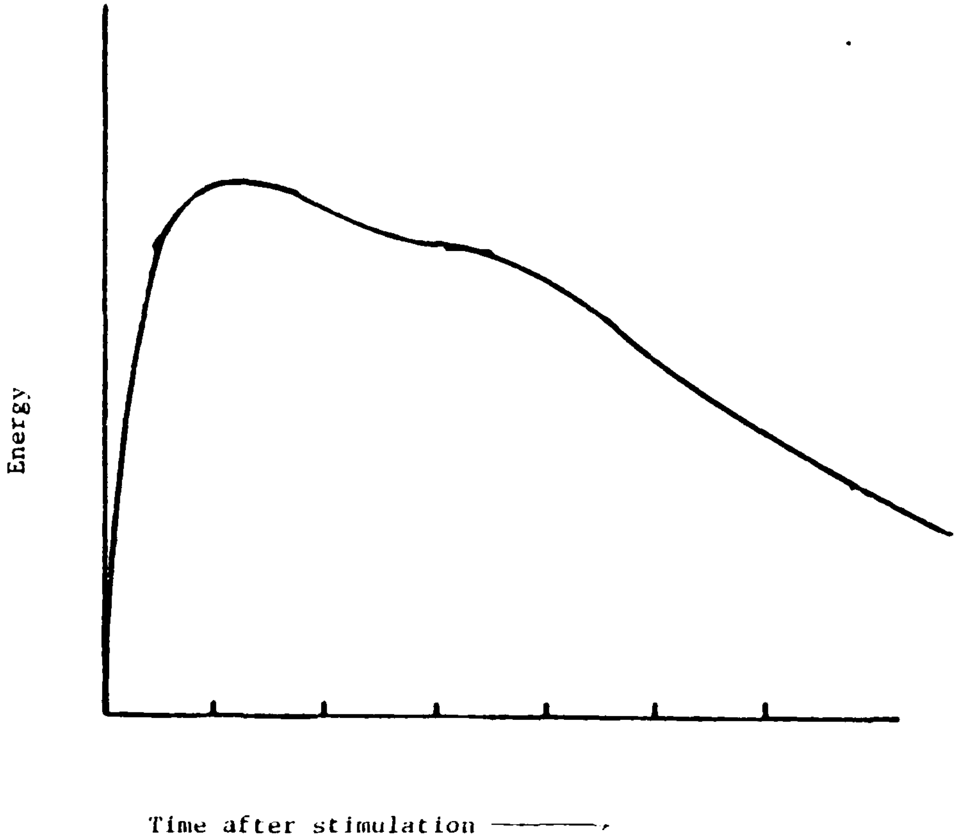

Possible Energy Diagram of a Molecular System after Stimulation

Fig. 1

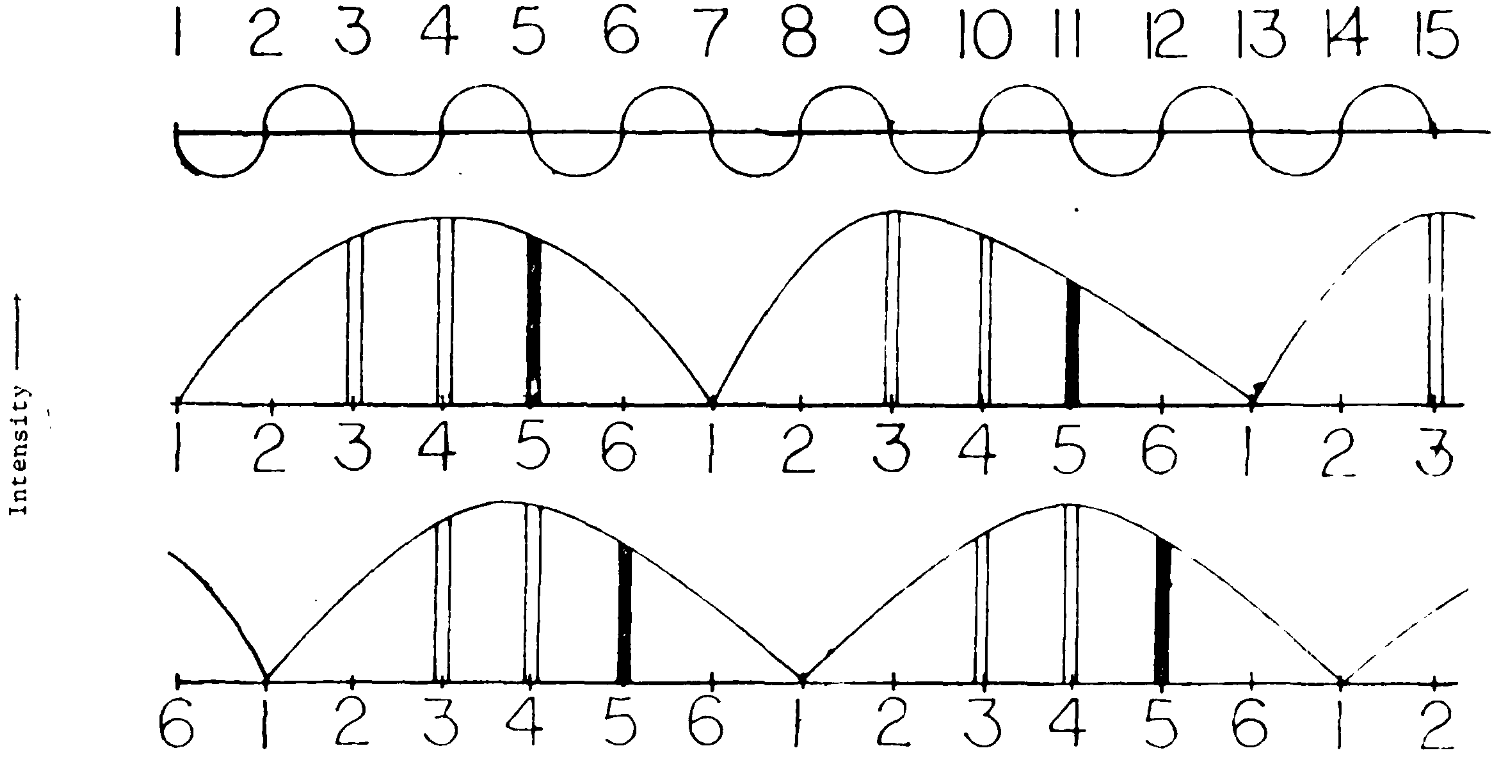
1 2 3 4 5 6 7 8 9 10 11 12 13 14 15
Intensity
1 2 3 4 5 6 1 2 3 4 5 6 1 2 3
6 1 2 3 4 5 6 1 2 3 4 5 6 1 2

Diagram of a TRS Collection

This shows three files N = 3, N = 4, N = 5 being collected at a stimulation interval of six zero crossings. Collection file N = 5 is shaded. Each file will be collected until all mirror positions needed have been recorded with a pulse from each cone.

A. is a plot of zero crossings of the [illegible]

of optical retardation and time.

B. is a plot of two complete [illegible]

resulting source intensity as a function [illegible]

time numbered with 1 corresponding [illegible]

C. is a plot of one fractional, two [illegible]

intervals and the resulting source intensity [illegible]

and time with time numbered with [illegible]

interval.

Note the optical retardation scale [illegible]

interval is moved the zero [illegible]

along the optical retardation [illegible]

the start of a new stimulation interval [illegible]

position corresponding to [illegible] in A for experiment [illegible]

position corresponding to [illegible] in A for experiment [illegible]

B. One View of the Advantages of Infrared Interferometry[≠]

[illegible] Chase and W. G. Fateley*

Chemistry Department
Kansas State University
Manhattan, Kansas 66506

[illegible] applications of FT-IR [illegible] Molecular and [illegible] NATO Advanced Study Institute, [illegible]

* [illegible]

Introduction

Since the mid 1950's many papers have appeared emphasizing substantial advantages of interferometry over dispersive spectroscopy. While it is generally recognized that these advantages are qualitatively correct, the magnitudes of these advantages are still subject to great debate.

In the beginning it was apparent that with the excitement of the "new" form of spectroscopy, the rational behind many of these arguments was clouded and that the total advantage of interferometry might not be as great as first anticipated.

In this chapter we wish to review the advantages and disadvantages of interferometry and attempt to quantify them to the greatest extent possible.

I. Discussion

Let us use a simple optical system for an interferometer with an infrared light source inclined at an angle θ with respect to the optical axis striking a collimator at an angle γ, the differential throughput may be written as:

$$dE = (\cos\theta dA_s)\ (\cos\gamma dA_c)/r^2 \qquad (1)$$

where: dA_s = area of the source

dA_c = area of the collimator

r = distance between source and collimator

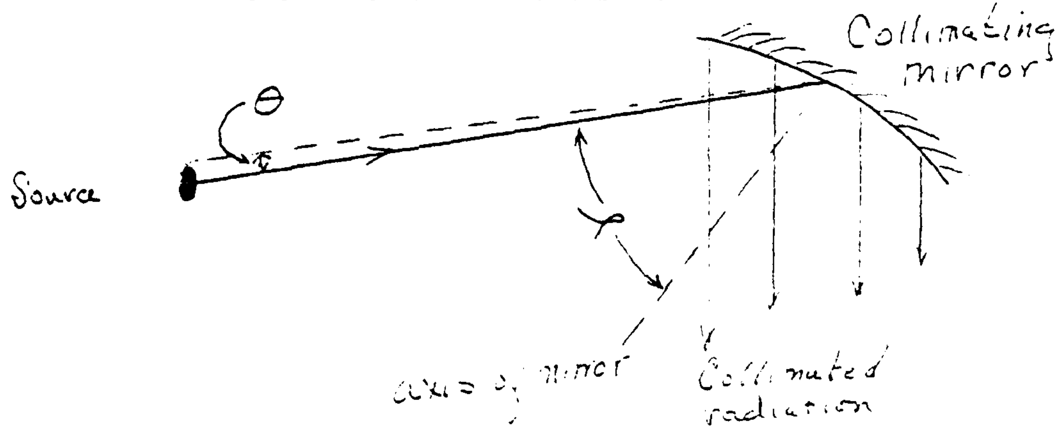

The solid angle subtended by the source can be written as follows:

$$d\Omega = \cos\theta dA_s/r^2 \qquad (2)$$

and the projected area can be expressed as:

$$dA = \cos\gamma \, dA_c \tag{3}$$

Therefore, eq(1) can be rewritten as:

$$dE = d\Omega dA \tag{4}$$

$$E = \Omega A \tag{4'}$$

Assuming a finite source size, the optical path difference between the two arms of a Michelson interferometer is

$$\Delta = ((\sqrt{3+\cos^2\Theta} - 1)(1+\cos\Theta)-2)f + (\sec\Theta - 1)L + 2d\cos\Theta \tag{5}$$

where:

f = focal length of collimating mirror

L = distance from source to fixed mirror

d = distance from fixed to movable mirror (which is equal to the spatial displacement).

The first two terms in eq. (5) are of different sign and are very small as compared to the third term. Thus, they tend to cancel in most cases leaving the approximation

$$\Delta = 2d\cos\Theta \tag{6}$$

If the source is considered to be a point, i.e. $\Theta=0$, then eq.(5) desscibing the optical path difference between the two arms of an interferometer reduces to

$$\Delta p = 2d \tag{7}$$

It is this deviation of Δ from Δp which leads to a frequency spread, ref. 1, 2 which is

$$\Delta\bar{\nu} = \bar{\nu}_{max}\Omega/2\pi \tag{8}$$

where $\bar{\nu}_{max}$ = the highest wavenumber in the spectrum.

Substituting eq. (8) into eq.(4') we obtain the relation for the throughput of a Michelson Interferometer:

$$E^I = 2\pi A^I \frac{\Delta\bar{\nu}}{\bar{\nu}_{max}} \qquad (9)$$

where A^I = area of collimating mirror in the Interferometer Superscript I will designate interferometry and D will indicate dispersive spectroscopy in our comparison.

For a dispersive spectrometer the solid angle may be written as

$$\Omega^D = \frac{hw}{f^2} \qquad (10)$$

where: h = slit height

w = slit width

f = focal length of collimator

since:

$$w = f\frac{(d\Theta)}{(d\bar{\nu})}\Delta\bar{\nu} \qquad (11)$$

and

$$\bar{\nu} = \frac{m}{d(\sin i + \sin\Theta)} \qquad (12)$$

The angular dispersion of the grating becomes

$$\frac{d\Theta}{d\bar{\nu}} = \frac{m}{\bar{\nu}^2 d\cos\Theta} \qquad (13)$$

and the solid angle becomes

$$\Omega^D = \frac{hm}{fd\cos\Theta}\,\frac{\Delta\bar{\nu}}{\bar{\nu}^2} \qquad (14)$$

where m = order of the grating

d = the distance between the lines of the grating.

Substituting eq.(14) and eq.(3) into eq.(4') we obtain for the throughput of a dispersive spectrometer

$$E^D = \frac{hmA^D}{fd}\,\frac{\Delta\bar{\nu}}{\bar{\nu}^2} \qquad (15)$$

A. Jacquinot Advantage

In 1954 Pierre Jacquinot recognized the throughput advantage of the interferometer over dispersive instruments and the ratio E^I/E^D is now usually termed "Jacquinot's advantage", ref. 3, 4,

Using eq.(9) and eq.(5) we obtain an equation for Jacquinot's advantage.

$$E^I/E^D = \frac{2\pi fd}{hm} \frac{A^I}{A^G} \frac{\bar{\nu}^2}{\bar{\nu}_{max}} \qquad (16)$$

Substituting approximate values for the constants in eq.(16) one obtains

$$\frac{E^I}{E^D} = 0.075 \frac{\bar{\nu}^2}{\bar{\nu}_{max}} \qquad (17)$$

It should be noted that gratings are normally changed several times during a complete scan of the mid-IR region and therefore d can be a function of the frequencies, as $d=d(\bar{\nu})$. Since the value of d increases stepwise with decreasing frequency the value E^I/E^D may be thought of as being "slightly less than quadratic" in frequency.

It should also be noted that Jacquinot's advantage is a measure of the amount of radiation striking the detector. Thus, this advantage is most important when the amount of radiation is minimal, e.g. such as the measurement of weak emissions, or at high resolution interferometric studies.

B. Fellgett's Advantage

If one measures a spectrum of width $\delta\bar{\nu}$ at a resolution $\Delta\bar{\nu}$ the number of spectral elements is:

$$M = \frac{\delta\bar{\nu}}{\Delta\bar{\nu}} \qquad (18)$$

In a dispersive instrument the time devoted to each spectral element is therefore T/M where T equals the total active time of the scan. The total active time of data acquisition may be considered to be the total time during which the sample was being irradiated.

C. Hadamard Transform Spectroscopy≠

by

C. S. Bartholomew and W. G. Fateley*
Kansas State University
Manhattan, KS 66506

and

Narayan P. Murarka
IIT Research Institute
10 West 35th Street
Chicago, IL 60616

---

*Work supported by AFOSR, Grant No. 78-3617

≠C. S. Bartholomew, W. G. Fateley, and N. P. Murarka, "Analytical Applications of FT-IR to Molecular and Biological Systems", Proceedings of the NATO Advanced Study Institute, Florence, Italy, 1980, Edited by J. R. During. A. Reidel Publ. Co., 1980.

Fourier Transform Interferometry has become a useful tool in infrared spectroscopy. These instruments require very exacting optics and mechanical alignments which necessitate micrometer accuracy in mirror alignments and the exacting measurement of mirror displacement. Because of these required low tolerances interferometers are very expensive and require constant calibration.

For the past 15 years Hadamard Transform Spectroscopy (HTS) has offered us a very unique and promising technique for spectral observation. This HTS spectrometer shares the high throughput and multiplexing advantages of the Michelson interferometer. But, the Hadamard transform spectrometer has distinct advantages: 1) Mechanical tolerances on the oder of millimeters are required, i.e. three orders of magnitude higher than an interferometer. 2) The higher tolerances mean lower cost in production and less maintenance. 3) Any conventional dispersive spectrometer can be converted to a Hadamard transform spectrometer quite easily if a minicomputer and a slot system are available. This type of conversion can reduce the cost of this instrumentation even more. 4) The transforms for creating spectra data from the encoded slot data are much simpler for HTS. Computer time is drastically reduced for HTS over that for Fourier transform spectrometry; thus simple computers can be used.

Yates, in 1935, ref. 1, described how error levels could be reduced by weighing items as a group rather than individually. It is amazing that even today with the use of computers this simple form of multiplexing has not become a widely used tool for infrared spectroscopy.

To demonstrate HTS, Sloane and Harwit have used systems of weighing; we shall utilize this method as well. By weighing different combinations of several objects of unknown mass, the error in measuring an individual object mass can be reduced, ref. 2, 3. For example, suppose we were to weigh four objects with masses m_1, m_2, m_3 and m_4 on a double pan balance. (There are still one or two around in the archives of our laboratories.) For the first measurement we might place all four objects on the right pan and record the mass. Next we could place two objects on the right pan and two on the left, and so on in different combinations. By weighing four different combinations of the objects we could easily deduce the masses of the individual objects.

If the objects are weighed separately, the best estimates ($\hat{m}$) of the masses of any one object will be the actual mass of that object plus the error associated with the weighing of that object {the measured mass (M)}.

$$M_1 = \hat{m}_1 = m_1 + e_1 \qquad M_3 = \widehat{m}_3 = m_3 + e_3$$
$$M_2 = \hat{m}_2 = m_2 + e_2 \qquad M_4 = \widehat{m}_4 = m_4 + e_4$$

If it is assumed that the error is random with a mean value of zero and variance σ^2, then the average variances of the above mentioned objects will be

$$(\hat{m}_1 - m_1)^2 = e_1^{\,2} = \sigma^2, \; (\hat{m}_2 - m_2)^2 = e_2^{\,2} = \sigma^2, \; \ldots\ldots$$

When all four objects are weighed simultaneously the average error due to the balance and weighing procedure is going to be the same as when the objects are weighed individually.

$$M_1 = m_1 + m_2 + m_3 + m_4 + e_1$$
$$M_2 = m_1 + m_2 - m_3 - m_4 + e_2$$
$$M_3 = m_1 - m_2 - m_3 + M_4 + e_3$$
$$M_4 = m_1 - m_2 + m_3 - m_4 + e_4$$

The masses of the objects can be determined by solving four simultaneous equations for each unknown.

$$M_1 + M_2 + M_3 + M_4 = 4m_1 + 0 + 0 + 0 + (e_1 + e_2 + e_3 + e_4)$$

The best estimate is:

$$\hat{m}_1 = \frac{1}{4}(M_1 + M_2 + M_3 + M_4) = \frac{1}{4}(e_1 + e_2 + e_3 + e_4) + m_1$$

Since the variance of a sum of independent variables is the sum of the variances, the variances of the best estimate $\hat{m}_1$ (and of $\hat{m}_2$, $\hat{m}_3$, $\hat{m}_4$) is $\frac{1}{16} e_1{}^2 + \frac{1}{16} e_2{}^2 + \frac{1}{16} e_3{}^2 + \frac{1}{16} e_4{}^2 = \frac{1}{4}\sigma^2$.

Using just a single pan balance, the following weighing scheme could be effectively used:

$$\begin{aligned}
M_1 &= \phantom{m_1 + {}} m_2 + m_3 + m_4 + e_1 \\
M_2 &= m_1 + m_2 \phantom{{} + m_3 + m_4} + e_2 \\
M_3 &= m_1 \phantom{{} + m_2} + m_3 \phantom{{} + m_4} + e_3 \\
M_4 &= m_1 \phantom{{} + m_2 + m_3} + m_4 + e_4
\end{aligned}$$

Solving for m_1:

$$M_2 + M_3 + M_4 - M_1 = 3m_1 + e_2 + e_3 + e_4 - e_1 \text{ and}$$

$$\hat{m}_1 = \frac{1}{3}(M_2 + M_3 + M_4 - M_1) = m_1 + \frac{1}{3}(e_2 + e_3 + e_4 - e_1)$$

The variance for $\hat{m}_1$, then, is $\frac{4}{9}\sigma^2$. Similarly the variances of $\hat{m}_2$, $\hat{m}_3$ and $\hat{m}_4$ are $\frac{7}{9}\sigma^2$.

By weighing the objects in groups rather than individually, the errors for the estimated masses are reduced. Varying the combinations of objects being weighed and not weighed, as in the single pan balance, reduced the errors to $4\sigma^2/9$. Combinations of sums and differences of the objects' masses, as in the double pan balance, reduce the error even further to $1/4\ \sigma^2$ (from σ^2 for individual weighings of the objects).

The various position patterns (i.e. position on the right or left pan of the balance) used in the weighing of the objects are called weighing designs. These weighing designs can reduce the error in any group of measurements.

An absorption spectrophotometer measures the number of photons (i.e. intensity of radiation) of a certain wavelength light that are not absorbed by a particular sample. Since a quantity is being measured, the use of weighing designs becomes useful in reducing the error (which includes the noise) in spectrophotometric absorption measurements. The aforementioned "objects" correspond to wavelengths of light and the masses correspond to the number of photons passing through the sample and counted by a detector.

It is apparent that by using weighing designs, the error (or noise level in spectroscopy) could be reduced drastically. Error reduction becomes very important in infrared absorption spectroscopy for situations where the intensity of light is low. Subsequently, in the situation of limited intensity the sensitivity is low and the noise is proportionately higher than other spectroscopic regions. In these energy limited systems the most significant source of noise is the detector; thus, the error is independent of the signal applied.

The necessary conditions for applying weighing designs to infrared spectroscopy (and for that matter any spectroscopic technique) are: 1) The light must be separated into its component wavelengths, and 2) these components must be either transmitted, reflected and gathered as a negative contribution to the signal or, more simply, they must be blocked by some means. The first condition presents no problems. Dispersive gratings separate light into their various component wavelengths quite effectively. The technology in making dispersive spectrometers has been quite well developed and these spectrometers can be modified to do Hadamard Transform spectroscopy.

The second criterion for HTS can be obtained by creating a series of masks (number masks = number slots) containing slots that can be either opaque or transparent. These masks would be placed in the light beam's path and thus allow certain wavelengths of light to enter while blocking other wavelengths. A weighing would thus be created quite analogous to the case of weighing objects on a single pan balance; the objects (or wavelengths of light) are either detected or not detected.

Another type of mask might be a mask that either lets light through or reflects it to a different detector; one detector's signal is then subtracted from the other's, creating a situation comparable to weighing objects on a double pan balance. The errors can be reduced much more drastically using a reflectance mask, but implementation of this kind of system might be extremely difficult.

Instrument:

The Hadamard Transform spectrometer is basically a dispersive spectrometer with an encoding mask at the entrance slit and/or exit slit of the instrument, ref. 2. The basic components are a radiation source, an optical separator to separate the light into components wavelengths, the encoding mask, a detector, and a decoder to assimilate the data, see Fig. 1.

The optical separator could be any device such as a grating or prism that spatially separates the incident radiation into its optical components.

The slotted mask encodes the signal according to some weighing design by either absorbing, reflecting or transmitting the signal.

The encoder need be nothing more complicated than a digital computer.

The basic parts of three different spectrometers are shown in figure 2. The first spectrometer in this figure is a classic dispersive spectrometer with a narrow slit at both the entrance and exit. The middle design in this figure is a Hadamard Transform spectrometer with one narrow entrance slit and a mask of some weighing design used at the former position of the exit slit. The bottom drawing in figure 2 has a mask substituted in place of both the entrance and exit slits.

HTS requires as many measurements made as there are slots. For example, if a mask has 255 slots, then 255 measurements must be made.

Weighing Designs:

As can be imagined, a large number of weighing designs can be used to encode radiation of different spectral wavelengths. However, different weighing designs result in different error magnitudes. The choice of which design to use depends on which design gives the minimum error.

The Hadamard matrices (i.e., -1 or +1 elements) will give the minimum error in HTS. For weighing designs using +1 and 0 elements, the so-called S-matrix gives the minimum error for HTS. (Other weighing designs do exist and these will be indicated later.) See Appendix 1 for a discussion of these different matrices.

Sloane, et. al., ref. 4, provide a very elegant discussion on how to evaluate a weighing design. Most of the derivation given below will follow their description.

In Hadamard Transform Spectroscopy a light source is spatially dispersed into N channels. Each channel, j, of light has an average energy integrated over a specific time, e_j. The channels of light are either measured (+1), reflected (-1) or blocked (0) out simultaneously according to a weighing design, W_i, where $W_i = (w_{i1}, w_{i2}, \ldots. w_{iN})$ which is the $i^{\underline{th}}$ vector of weight. Thus, the total energy measured through a mask (weighing design) is the summation of the individual channel energies which have been allowed to pass through that mask, $\sum_{j=1}^{N} w_{ij}e_j$. In this summation w_{ij} is the individual channel (j) weight for mask W_i. The mask weights are assumed to satisfy $|w_{ij}| \leq 1$ and correspond to attentuation. The photodetector adds a random noise, n_i, which gives a final measurement:

$$E_i = n_i + \sum_{j=1}^{N} w_{ij}\ e_j, \ i = 1, 2, \ldots\ldots, M$$

A few assumptions must be made. (Note < > stands for ensemble averages.)

1) $\langle n_i \rangle = 0$, the overall average for the noise is zero.
2) n_i is independent of the signal
3) $\langle n_i^2 \rangle = \sigma^2$
4) successive measurements are uncorrelated ($\langle n_i n_j \rangle = 0$ if $i \neq j$)
5) $\langle \hat{\vec{e}} \rangle = \vec{e}$. The estimated value of the channel energy, if averaged over many readings, will be the actual channel energy.

Assumption number 3, above, says the ensemble mean square of the noise is the same for all measurements. This corresponds to integrating over equal time for those measurements, ref. 5. If the noise is due to the detector only, and if it is independent of size of signal (this assumes linear behavior of the photodetector); then, when averaging over many measurements, the mean square error will depend directly on the time duration the detector takes to make the individual observation.

To estimate the energies, e_j, one needs at least as many measurements (M) (i.e. one mask per measurement) as there are unknowns (N), ref. 4.

The observations are: $\vec{E} = \vec{e}W + \vec{n}$ where $\vec{E} = (E_1, E_2 \ldots E_m)$, the observations; $e = (e_1, e_2, \ldots e_N)$ the channel energies; $(W_1^T, \ldots W_M^T)$, matrix of masks and; $n = (n_1, \ldots n_M)$ noise (T stands for transpose.)

An estimate $\hat{\vec{e}}$ of $\vec{e}$ is a function of the observation, $\hat{\vec{e}}(E)$ lying close to $\vec{e}$. The accuracy of the estimate can be tested by minimizing the mean square error: $\epsilon = <(\hat{\vec{e}}-\vec{e})(\hat{\vec{e}}-\vec{e})^T>$.

Now, set the estimated value of the channel energies, $\hat{\vec{e}}$, to be a linear function of the observations, $\vec{E}$,

$$\hat{\vec{e}} = \vec{E}M$$

for some matrix M.

Minimizing $\epsilon = <(\hat{\vec{e}}-\vec{e})(\hat{\vec{e}}-\vec{e})^T>$

$$<\hat{\vec{e}}> = <\vec{E}M> = <\vec{E}>M$$

$$<\vec{E}> = \vec{e}W + <\vec{n}> = \vec{e}W$$

$$<\hat{\vec{e}}> = \vec{e}WM$$

Therefore, according to assumption 4 above, $<\hat{\vec{e}}> = \vec{e}$, WM must equal the identity matrix, I. If $M = N$, $M = W^{-1}$. If $M > N$ (M cannot be smaller than N), $M = W^T(WW^T)^{-1}$. Substituting for $\hat{\vec{e}}$ and $\vec{e}$,

$$\hat{\vec{e}} - \vec{e} = \vec{E}M - \vec{e} = \vec{e}WM + \vec{n}M - \vec{e}$$

$$WM = I$$

so, $\hat{\vec{e}} - \vec{e} = \vec{n}M$

$$= \vec{n}W^{-1}, \text{ if } M = N$$

$$= \vec{n}W^T(WW^T)^{-1} \text{ at } M > N$$

From assumption 2, $\langle n_i^2 \rangle = \sigma^2$ and $\langle nn^T \rangle = \sigma^2 I$; thus,

$$\varepsilon/\sigma^2 = \text{trace}\,[W^{-1} W^{-1T}] \text{ if } M = N$$

$$= \text{trace}\ [illegible]\ \text{if } M > N.$$

Other methods for finding the best weighing design exist, ref. 3. The A-optimal weighing design minimizes $\varepsilon = \frac{\sigma^2}{N}$ trace $(W^TW)^{-1}$.

A D-optimal weighing design maximizes the determinant of W det(W). D-optimality essentially minimizes the volume of region in which the estimate, $\hat{e}$, is expected to be found.

E-optimality maximizes the smallest eigenvalue of W^TW.

These methods for finding the best weighing design do not always agree. A-optimality seems to be the best method assuming the indiivdual mean square errors are about equal. The best weighing design can be found by applying one or more of the optimality criteria to that design.

Weighing designs and their characteristics are given in Table 1.

Hotelling[5] has shown that for any choice of mask W with $|w_{ij}| \leq 1$, the ε_i are bounded by $\varepsilon_i \geq (\sigma^2/N)$, and that it is possible to have $\varepsilon_i = (\sigma^2 N)$ for all i = 1, ..., N if and only if a Hadamard matrix H_N of order N exists, ref. 6.

The Hadamard matrix will provide the best weighing design for reduction of noise. This matrix and two other matrices will be considered in more detail. It is interesting to note that other matrices in Table 1 have not found much use in Hadamard Transform spectroscopy, therefore only a mention of these matrices is given here.

A Hadamard matrix is an N x N matrix of +1's and -1's constructed in such a way that,

$$HH^T = NI \qquad \text{see ref. 4.}$$

H can be normalized by multiplying the proper rows and columns by -1 to obtain +1's in the first row and column, ref. 3 and Appendix 1 of this chapter.

$$\left|\begin{array}{c:cccc} 1 & 1 & 1 & \cdots & 1 \\ \hdashline 1 & & & & \\ 1 & & G & & \\ \cdot & & & & \\ \cdot & & & & \\ \cdot & & & & \\ 1 & & & & \end{array}\right|$$

If $N \geq 4$, and k and l are two distinct rows of H then (excluding the first row),

row k has +1 and row l has +1 in N/4 places

... +1 ... -1 ...

... -1 ... +1 ...

... -1 ... -1 ...

and N must be a multiple of 4.

The dot product of any two rows of this matrix is zero and thus the matrix is orthogonal.

If one of the following conditions is satisfied, then G can be constructed as a cyclic matrix - a matrix where the $(i+1)^{\underline{th}}$ row can be obtained by shifting the $i^{\underline{th}}$ row one space to the right or left. Here the G matrix has N-1 rows and columns.

1) $N = p + 1$, p is a prime number

2) $N = p(p + 2) + 1$, p and $(p + 2)$ are prime

3) $N = 2^m$

For example:

$$G = \begin{vmatrix} 1 & -1 & -1 \\ -1 & 1 & -1 \\ -1 & -1 & 1 \end{vmatrix}$$

$$\text{row } k \cdot \text{row } \ell = \begin{cases} -1 & i \neq j \\ N-1 & i = j \end{cases}$$

For more cyclic matrices, G, the reader is referred to the literature, references 7, 8 and 9.

The third choice for W is S, which can be generated from G by replacing +1's with 0's and -1's with +1's, see Appendix 1.

$$\text{row } k \cdot \text{row } \ell = \begin{cases} N/4, & i \neq j \\ N/2, & i = j \end{cases}$$

By taking the trace $(W^{-1}(W^{-1})^T)$ it is found, ref. 4:

Matrix w	trace (ε/σ^2)
H^T	1
G^T	2 - 2N
S^T	$4 - 8/N + 4/N^2$

Experimental:

The S-weighing designed mask utilizing 0 or 1 cyclic elements is the most practical and easiest mask to design. Experimentally, zero denotes an opaque slot in the mask, +1 denotes a transparent slot and -1 denotes a reflecting slot. The experiment is greatly simplified by the fact that only 2N-1 slots are needed in one mask to record Hadamard Transform Spectroscopy if a cyclic weighing design is used. Thus, one can stepwise move a mask across an entrance or exit slit and record the intensity of radiation impunging upon the detector for each step of the mask. We refer the reader to Figure 3 which demonstrates this stepping effect.

In practice the signal must be dispersed. Since noise increases by the square-root of the detector surface area, a small size detector is essential, ref. 5. By refocusing the radiation back through the optics, the light can be focused to an area approximately the same size as the entrance slit, ref. 10. A typical arrangement used to accomplish this in Hadamard Transform Spectrometry is shown in Figure 4 from ref. 11. Of course, if an entrance mask has the same number of slots as the exit mask, refocusing is not necessary since the entrance and exit slits will then be the same size.

In Figure 4, the light is passed through the entrance aperature to the grating. The dispersed radiation from the grating is directed to a collimating mirror. The mirror reflects the radiation onto the mask. The encoded light beam is then returned by the same path through the dispersive optics and focussed at the entrance focal plane, ref. 11. In Decker's spectrometer, the entrance slit was slightly below the optical axis, so the returning exit signal was slightly above the optical plane to allow simple detection. The signal was detected by a 1.0 mm square lead sulfide detector. Of course, the detector will vary depending on the region of the infrared spectrum used in the experiment.

Decker used an S_{255} matrix as a weighing design, a 509 slot (2N-1) mask. The entering beam passes through a single narrow slit which is .185 mm high. Decker found the signal to noise (S/N) ratio to be 39.1[illegible]. Using identical optics as the Hadamard Transform Spectrometer, but using a monochromator instead of the weighing design mask, the S/N was only ~4.764. The Hadamard Transform Spectrometer increased the S/N

by a factor of 8.0612 ± 0.3110 over that of a conventional monochromator. The increase in S/N ratio was very close to the theoretical increase of a factor of 8.01567.

An instrument utilizing an S_{2047} weighing design mask (4093 slots) created problems in calculating a S/N ratio. Decker reported just before termination of his experiments that he could not measure any detectable noise when any signal, no matter how small, was detectable in the spectrometer's output, ref. 12.

Harwit, et. al., tested an instrument with a S_{255} exit mask (n) and a S_{15} entrance (m) mask, ref. 10. In this experiment Harwit used only (n + m-1) measurements. The exit mask was used in n/m positions and the entrance mask was stepped through its m positions for each n/m exit mask position, ref. 10. Theoretically, one can expect ε/σ^2 to equal 16/m+1. Improvement over a single slot entrance, S_{255} mask exit spectrometer was shown to increase the S/N by 4.31 (computer simulation). The theoretical limit is 4.26. Assuming the RMS noise to be 0.2 times the peak to peak noise height, the signal to noise ratio was about 40 for the 1.7 μm mercury line measured, ref. 10 and 11. A S_{509} mask entrance and S_{255} mask exit instrument performed with S/N of about 70. These results were not significantly better than Decker's single slit entrance, S_{255} exit mask instrument (S/N = 40), for the factor of 4.26 was not realized in this experiment. Since the dispersive spectrometers used were not the same, differences in the design of the instruments could explain this lack of improvement.

If nm measurements are made, one can expect ε/σ^2 to equal 22.2/n ($\frac{16}{m+n}$, if m >> n). In an experiment utilizing 19 slot exit and entrance masks, the mean square noise was found to be 4.2 times higher for 37(n + m-1) measurments than for 361 (nm) measurements, ref. 13.

Spectral Imaging, Inc., using a configuration with a S_{255} exit and S_{15} entrance mask, claims "a figure of merit" for their instrument over 120 times that of an equivalent scanning-monochromator spectrometer and up to about 30 times that of commercially-available interferometer spectrometers of equal resolution and spectral multiplexing, ref. 14.

"Figure of merit" was defined as:

$$E = RLN^{1/2} A_d^{-1/2} \langle \varepsilon_\lambda D_\lambda^R \rangle_\lambda$$

where $R = \lambda/\Delta\lambda = \nu/\Delta\nu$ is the resolution

L is the "etendu" $\simeq nA_g/\ell R$ for HTS or grating spectrometer

$\simeq 2\pi A_M/R$ for Michelson FTS

N is the degree of spectral multiplexing = number of slots for HTS

n = number of entrance slots of HTS

A_d = detector area

A_g = grating area

A_M = Michelson's entrance aperature area

$\ell = \frac{\text{focal length}}{\text{slit height}}$, for a grating instrument

$\langle \varepsilon_\lambda D_\lambda \rangle_\lambda$ = average over the wavelength range for the product of detector detectivity times the net of filter, grating, beam splitter etc., efficiency.

$E_{HTS}/E_{monochromator} \approx 1/2\ n\ N^{-1/2}$

$E_{HTS}/E_{Michelson\ interferometer} \approx (n/2\pi\ell)(A_S/A_M)(e_g/e_{bs})$

ε_g = grating efficiency

ε_{bs} = beam splitter efficiency

It was somewhat disappointing that no experimental data was given to support the theoretical claims made by Spectral Imaging, Inc. Other experimental instruments utilized weight designs of S_{23} to S_{255} for entrance masks and S_{511} to S_{2047} exit masks.[14] It is interesting to note the resolution was lower than 0.1 cm^{-1} in some of these instruments. Ranges of spectral bands were from 4 to 16 μ depending on optical configuration. Disappointing to us was the fact that no experimental data demonstrating S/N advantages and resolution of these spectrometers were given in these references.

Doubly Multiplexed Spectrometers:

The Michelson interferometer has demonstrated a unique advantage over conventional grating spectrometers. A large part of this advantage is due to the very high throughput of an interferometer (Jacquinot's advantage) and multiplexing (Fellegett's advantage), ref. 16.

If high throughput can be added to the advantage of using polychromatic light (Fellgett's advantage), a Hadamard Transform spectrometer should show a similar increase in S/N ratios. To utilize Jacquinot's advantage in Hadamard transform spectroscopy, an entrance mask can be used in addition to an exit mask. For the S-matrix weighing design HTS should increase the throughput to about one half that of an interferometer. Using Hadamard matrices the throughput of HTS should approximate that of a Michelson interferometer, ref. 16.

In practice an S mask is typically placed in the entrance of a dispersive grating spectrometer equipped with an S exit mask. For each position of the exit mask, the entrance mask is stepped through its m positions. The total number of measurements can be reduced from mn measurements to (n + m-1) measurements.

If the experiments use a) $n = m = N$, b) N^2 observations and c) S_N-matrix weighing designs, then the mean square error, $\varepsilon \simeq (22.2/N)\sigma^2$, reference 16. Compare this mean square error with the mean square error $N\sigma^2$ for a single slot entrance and exit spectrometer and the mean square error of $\{2-(2/(N+1)\}^2\sigma^2$ for a spectrometer with a single slot entrance slit which utilizes an S_N-matrix exit mask, ref. 16. The results predict for large N, a dobubly multiplexed instrument will theoretically reduce noise by a substantial factor.

Error:

The error analysis in our previous discussion has assumed that the only errors are those associated with the detector. Of course, other errors can result from the optics and masks of the instruments. Tai, et. al., using an S_{255} masks, found spurious negative bands appearing at higher and lower energies compared to the principle band. Tai was able to partially explain the effect when he simulated too wide and too narrow opaque mask slots. His conclusion was that the opaque slots were too wide.

Tai, et. al. analyzed the case where an opaque slot is too wide (i.e., when the transmitting slot is too narrow), and found the optical effect will give a spectrum of $(1-\varepsilon, \varepsilon/2, 0 \ldots 0, -\varepsilon/2, -\varepsilon/2, 0 \ldots 0, \varepsilon/2)$; for slots too narrow the spectrum will be $(1-\varepsilon, \varepsilon/2$, 228 0's, $\varepsilon/2, \varepsilon/2$, 22 0's, $\varepsilon/2)$. For any S-matrix mask, there will always be four equal intensity peaks in addition to the main peak. Along with the spurious bands, a spectrum will show a peak on either side of the main peak, causing a broadening appearance.

Other errors may result from distortion, aberations, and diffraction caused by the slots of an instrument, mask position and mask movement. In a typical Hadamard Transform spectrometer, radiation that should pass through a certain slot will frequently spread onto other mask positions on the detector. Here T represents the Transfer matrix and it is the matrix describing the radiation distribution that results from light passing through a slot, ref. 18.

The matrix elements of T correspond to the proportional intensity inpining on a certain slot position of a specific detector measurement.

W, as before, is the weighing design matrix.

The detector readings, $\vec{E}$, of measurements i from a Hadamard transform spectrometer are

$$\vec{E} = TW\vec{e} + \vec{n}$$

where $\vec{E} = (e_o, E_1, \ldots E_{n-1})^T$

$\vec{e} = (e_o, e_1 \ \ldots e_{n-1})^T$

$\vec{n} = (n_o, n_{.} \ \ldots n_{n-1})^T$ ref. 18.

In a conventional monochromator

$$\vec{E} = T\vec{e} + \vec{n}$$

The results of all the incident radiation not falling in the same slot position after passing through the slot are artificially broadened spectral lines and increased noise.

If there were no distortion of light through a slot position then T would be the identity matrix. The mean square errors for the instruments would be those mentioned previously under weighing designs. For simplicity in our discussion we will assume that the singal appears only in the first slot position.

If the slot is sufficiently wide to eliminate diffraction, the intensity of radiation detected will be triangular shaped with the maximum at the mid point of the slot profile (slit function). The base will appear twice as wide as the slot and symmetric about the slot position (Figure 5a). The errors discussed in ref. 18 arising from the above constraints are:

$$T = \frac{1}{6} \begin{vmatrix} 4 & 1 & 0 & \cdots & 0 & 1 \\ 1 & 4 & 1 & \cdots & 0 & 0 \\ \cdot & \cdot & \cdot & \cdots & \cdot & \cdot \\ 1 & 0 & 0 & \cdots & 1 & 4 \end{vmatrix}$$

Conventional monochromator: $\varepsilon = 2\sqrt{3}\,N\sigma^2$

Hadamard transform spectrometer (S exit mask) $\varepsilon \simeq 13.86\,\sigma^2$

HTS with quality matrix (S exit mask) $\varepsilon \approx \{4-8/N + 4/N^2\}$, N is large

Multiplexing decreases the error by N/4.

A very narrow slot resulting in full defraction gives the slot function shown in Figure 5b, ref. 18.

The first row of T is (0.6667; 0.1482, 0.0080, 0.0031, ... 0.0017, 0.0031, 0.0080, 0.1482) (note T is a cyclic matrix).

The errors are:

Conventional monochromator: $\varepsilon = 2.93\,N\sigma^2$

Hadamard transform spectrometer (S-exit mask) $\varepsilon = 11.74\sigma^2$

Again multiplexing decreases the error by N/4. This decrease in error is general for all T-matrices. Also, for any (0,1)-matrix W, $\varepsilon \leq 10.34\,\sigma^2$; N large, ref. 18.

The matrices T give an indication of the noise and line broadening. For example, the larger in number and size of the off-diagonal terms, the larger the error.

If the slot mask is not aligned properly behind the blocking mask, broadening and increased noise results in a Hadamard Transform spectrophotometer.

T is an asymmetric circulant with first row:

$$1/6\ (4-G\,\delta^2 + 3\delta^3,\ (1-\delta)^3,\ 0\ \ldots\ 0,\ \delta^3,\ 1 + 3\delta + 3\delta^2 - 3\delta^3)$$

A slight error in slot width compared to stepping size over a large number of step positions can result in broadening and increased noise, ref. 18.

The ith row of T is $1/6[0, \ldots 0, (i\Delta)^3, 1 + 3i\Delta)^3, 4-6(i\Delta)^2 + 3(i\Delta)^3, (1-i\Delta)^3, 0 \ldots 0$; $4-6(i\Delta)^2 + 3(i\Delta)^3$ is on the main diagonal, the initial position is assumed to be correct and the final position is off by $n\Delta$.

A continuously moving mask causes a pronounced increase in broadening over a stepped mask with the first row of T being:

$\frac{1}{384}$ (230, 76, 1, 00, ... 0, 0, 1, 76) ref. 18.

To reduce broadening, T must be incorporated into the solving of the spectral intensities. The best estimate of the e_i's are:

$$e = W^{-1}\ T^{-1}\ E$$

The transfer matrix T, must be determined for the specific instrument being used.

Imagers:

As mentioned earlier only (n + m-1) measurements are needed to develope a spectrum from a doubly encoded Hadamard Transform Spectrometer. But mn different measurements made from mn linear independent weighing designs could be taken (note the error analyzed for mn measurement (22.2/n) and that analyzed for n + m-1 measurements (16/n+1) described previously in this text). The extra measurements can provide one-dimensional spatial information (i.e. the IR spectra at different distances across a source). However, this increase in spatial information can be obtained only at the cost of signal to noise ratios.

In general, each dimension added to a mask allows one to obtain another parameter, ref. 19. Thus, using a two-dimensional entrance mask and a one dimensional exit mask (Figure 6), spectral information in two dimensions is obtained. With two two-dimensional masks, an additional parameter could be resolved (e.g. polarization data).

A typical imager is shown in Figure 7, ref. 2. Swift, et. al., used an imaging spectrometer to obtain a cathode ray display of the 3.06 to 6.33 μm spectral region of the CO_2 emission of a flame, ref. 20. The source of the CO_2 emission was clearly displayed.

Hadamard Transform Imaging Spectrometers show great promise in collecting spectral data from surfaces. Spectral data from the earth's surface (such as infrared detection) in relation to its regional proximity is one obvious example for satellite applications.

Conclusion

Hadamard Transform Spectroscopy has some very nice applications in the detection of infrared radiation, especially for two dimension survey spectra. HTS incorporates both Fellgett's and Jacquinot's advantages, which are so useful in today's Fourier Transform Spectroscopy. The comparison of HTS to FTIR finds HTS within the same order of magnitude for performance, although much development is needed in experimental technology and weighting function for HTS. The most dramatic and possibly the most important advantage of HTS over FTIR is the reduced cost of a Hadamard Transform Spectrometer.

Three factors combine to reduce the price of a Hadamard Transform Spectrometer to one third that of a Fourier Transform interferometer:

1) HTS requires tolerence in the millimeter range while FTIR tolerance are in the micrometer region or less.

2) Computer time is an order of magnitude less for HTS.

3) Most dispersive spectrometers can be converted to a Hadamard Transform Spectrometer by substituting slotted masks in place of the slit systems.

In addition, less sophisticated computers and software are needed in HTS. For example, the He-Ne laser signals used to track the mirror in FTIR are not necessary in HTS. The Connes effect is still realized in HTS since the mask will measure individual frequencies with great precision and allow substraction and spectral stripping technique which are now so important to spectroscopists applying FTIR techniques. The minimization of moving parts makes HTS a viable instrument for situations where vibrations are present, i.e. air craft and satellite surveillance.

Hadamard Transform Spectroscopy does lack the full advantages realized by FTIR in the far infrared region. Here interference from the mask can be a very serious problem.

Possibly the greatest potential for HTS will be the two dimensional spectral survey of a surface. Here specific chemical identification can be monitored in two dimensional space. This two dimensional monitoring can be very useful for systems as small as flames to pollution monitoring by aircraft surveillance over cities. Certainly of great interest would be the mapping of earth resources and the acquisition of meterological data.

Hadamard Transform Spectroscopy represents a very unique and potentially useful tool for analytical chemistry.

Table 1[+]

W	Elements	N	Conditions	A-optimal $(\frac{\varepsilon}{\sigma^2})$	D-optimal	E-optimal
H_N	-1,1	4t	$H_N H_N^{+} = N I_N$	$1/N$	$N^{N/2}$	N
D_N	-1,1	4t+1 4t+2	(N,K,λ) sym block design* -change 0 to +1 and 1 to -1	$\frac{[N^2-N-4(N-2)n]}{4n[N^2-4(N-1)n]}$ for $n = k-\lambda$	$(4n)^{(N-1)/2}$ $[N^2-4(N-1)n]^{1/2}$	$\min[4n, N^2-4(N-1)$
P_N	-1,1	4t+1 (N=5,13,25)	sym block design* with $N=(d^2+1)/2$ $k = (N+d)/2$, $\lambda = (N+2d+1)/4$	$\frac{2}{2N-1}$	$(N-1)^{(N-1)/2}$ $(2N-1)^{1/2}$	N-1
C_N	1,-1,0	4t+2	$C_N C_N^T = (N-1) I_N$	$\frac{1}{N-1}$	$(N-1)^{N/2}$	N-1
E_N	-1,0,1	4t+2	$E_N^T E_N = \begin{bmatrix} Z & 0 \\ 0 & Z \end{bmatrix}$; $Z = (\frac{1}{2}N-2) I_{N/2} + 2J_{N/2}$ #	$\frac{1}{N-1}$	$2(N-2)^{(N-2)/2}$ $(N-1)$	N-2
G_N	-1,1	4t+3	Delete the first row and column of a normalized H_{N+1} matrix.	$\frac{2}{N+1}$	$(N+1)^{(N-1)/2}$	1
Q_N	-1,1	4t+3 (N=7,31)	Sym. block design*; $N=(d^2+3)/4$, $k=(N+d)/2$, $\lambda=(N=2d+3)/4$	$\frac{4N-6}{(4N-3)(N-3)}$	$(N-3)^{(N-1)/2}$ $(4N-3)^{1/2}$	N-3
A_N	0,1	4t 4t+2	Sym. block design*	$\frac{k(N-2)+1}{k^2(N-k)}$	$k(k-\lambda)^{(N-1)/2}$	$k-\lambda$
F_N	0,1	4t+1	To the elements of E_N, change 1 to 0, -1 to 1	----	$2^{(-N+1)} N(N-1)^{(N-1)/2}$	---
S_N	0,1	4t+3	See Appendix I and Text	$\frac{4N}{(N+1)^2}$	$2^{-N}(N+1)^{(N+1)/2}$	$\frac{1}{4}(N+1)$

Con't

† I is the identity matrix; J is the all ones matrix

* A symmetrical block design is a collection of subsets of size k acquired from a total N objects, such that any two blocks have λ common objects. Its incident matrix, A, forms the weighing design. The (N,k,λ) symmetrical block design converts to the incident matrix, A, by forming an N x N matrix, $A = (a_{ij})$, such that $a_{ij} = 1$ if the ith block contains the j'th object and $a_{ij} = 0$ if the i'th block does not contain the j'th object.

+ (Note: A-optimal is the average mean square error. To get the total mean square error, multiply by N.)

Appendix I. The Generation of the H, G and S matrices

There are two convenient methods for generating weighing design matrices. First, previous literature describes the construction of cyclic S-matrices which do not have length $N = 2^n-1$ (e.g. $N = 4t-1$, where N is a prime number; $N = p\ (p + 2)$ where p and $p + 2$ are both prime numbers), ref. 4 and 21.

However, if the matrix does not have to be cyclic, construction of a H-matrix is quite straightforward. All H-matrices have the relation

$$H_{2i} = \begin{vmatrix} H_i & H_i \\ H_i & H_i \end{vmatrix}$$

For example, ref. 21:

$$H_1 = \begin{vmatrix} 1 \end{vmatrix}$$

$$H_2 = \begin{vmatrix} H_1 & H_1 \\ H_1 & -H_1 \end{vmatrix} = \begin{vmatrix} 1 & 1 \\ 1 & -1 \end{vmatrix}$$

$$H_4 = \begin{vmatrix} H_2 & H_2 \\ H_2 & -H_2 \end{vmatrix} = \left|\begin{array}{cc:cc} 1 & 1 & 1 & 1 \\ 1 & -1 & 1 & -1 \\ \hdashline 1 & 1 & -1 & -1 \\ 1 & -1 & -1 & 1 \end{array}\right|$$

$$H_8 = \begin{vmatrix} H_4 & H_4 \\ H_4 & -H_4 \end{vmatrix} = \left|\begin{array}{cccc:cccc} 1 & 1 & 1 & 1 & 1 & 1 & 1 & 1 \\ 1 & -1 & 1 & -1 & 1 & -1 & 1 & -1 \\ 1 & 1 & -1 & -1 & 1 & 1 & -1 & -1 \\ 1 & -1 & -1 & 1 & 1 & -1 & -1 & 1 \\ \hdashline 1 & 1 & 1 & 1 & -1 & -1 & -1 & -1 \\ 1 & -1 & 1 & -1 & -1 & 1 & -1 & 1 \\ 1 & 1 & -1 & -1 & -1 & -1 & 1 & 1 \\ 1 & -1 & -1 & 1 & -1 & 1 & 1 & -1 \end{array}\right|$$

and so on.

A G matrix can be constructed from this H-matrix by deleting the first row and first column, which in this case are positive 1s.

The S-matrix can be obtained from the G-matrix by the following substitution, ref. 22. All elements which are +1 are replaced by 0, all elements that are -1 are replaced by +1. If this same substitution is made on the H-matrix, the resulting arrangement is the S-matrix.

A cyclic S-matrix can be constructed using primitive polynomials (modulo 2) for the $N=2^n-1$ order matrix, ref. 5. To do this let e_o, ... e_{N-1} be the ordered elements of the first row of S.

$P_n(X) = X^n + a_{n-1} X^{n-1} + \ldots + a_o$ is a primitive polynominal of degree n. There is an excellent list of the polynomials of n degree in ref. 4, table 2 and we shall not repeat these here. The first n elements of a row can be chosen arbitrarily, as long as the row is not all zero elements. The other elements of the row are generated from $e_{m+n} = \sum_{i=0}^{n-1} a_i e_{m+i}$ $[0 \leq m \leq (N-n-1)]$. The terms are added by modulo 2 ignoring carries, i.e., 1 + 1 = 0, 1 + 0 = 1, 0 + 1 = 1, 0 + 0 = 0.

For example, suppose $N = 2^3-1 = 7$. A primitive polynomial of degree 3 is $P_3(X) = X^3 + X + 1$ and $a_o = 1$, $a_1 = 1$ and $a_2 = 0$ (ref. 5). Choosing $e_o = e_1 = e_2 = 1$, the first n = 3 terms, then

$$e_3 = a_o e_o + a_1 e_1 + a_2 e_2 = 1 + 1 + 0 = 0$$

$$e_4 = a_o e_1 + a_1 e_2 + a_2 e_3 = 1 + 1 + 0 = 0$$

$$e_5 = a_o e_2 + a_1 e_3 + a_2 e_4 = 1 + 0 + 0 = 1$$

$$e_6 = a_o e_3 + a_1 e_4 + a_2 e_5 = 0 + 0 + 0 = 0$$

The elements of the first row of the S-matrix can also be produced using a shift register, ref. 17. A shift register for $p_{(x)} = 1 + X + X^4$ is shown in Figure 8, ref. 17.

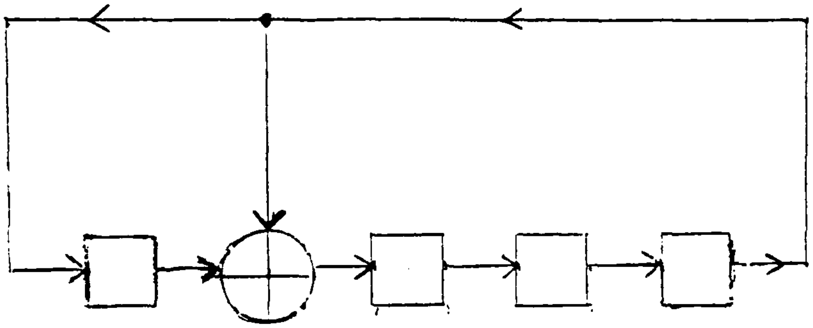

Figure 8. Here the box, □, is the delay element which holds a zero or a positive one. The quartered circle, ⊕ is a modulo 2 addition.

The shift register will go through 2^n-1 states before repeating. A n x (2^n-1) matrix is created quite conveniently and the first row can be used as the first row of a cyclic S-matrix. Subsequent rows of the S-matrix are produced by cycling the previous row one space to the right or left. Reversing a previous process for generalizing an S-matrix from a G-matrix; if the elements of the S-matrix which are zero are replaced by positive ones and the positive ones are replaced by negative ones, the G-matrix is created from the S-matrix. If this is followed by the addition of a first row and a first column of elements which are all +1, the H-matrix is generated.

Appendix II: FAST HADAMARD TRANSFORM

The individual spectral energies are found by: $\hat{\vec{e}} = W^{-1}\vec{E}$. Therefore we need matrix W^{-1} and $\vec{E}$. $\vec{E}$ is the vector of measurements. The inverse of the weighing design, W^{-1}, can be found by the following steps. The inverse of an S-matrix can be determined by first taking the transpose of this S-matrix, ref. 5. Second, the substitution of the fraction $2/(N+1)$ is made for each +1 and $-2/(N+1)$ for each zero in the transposed S-matrix. However, if S is a left cyclic matrix (i.e. the ith row is produced by shifting the previous row one space to the left), then the matrix S is its own transpose and the aforementioned transpose operation is not necessary. S^{-1} can be written as a product of $(2/N+1)$ and a matrix of +1's and -1's.

To find $\hat{\vec{e}}$, it follows that (N^2-N) additions or subtractions are required by straightforward matrix multiplication.

Now, if N equals 2^n-1 and the weighing design, S, is generated using a primitive polynomial (mode 2) of degree n, the number of steps needed to determine $\hat{\vec{e}}$ can be reduced to $(N+1)\log_2(N+1)$, ref. 5. This shorter method utilizes the fast Hadamard transform (FHT). Even though the Hadamard matrix multiplication performed by the FHT does not use the correct matrix, the FHT matrix is related to the correct matrix by two permutations.

The FHT algorithm, as presented by Nelson and Fredman, is a very useful technique, ref. 5. In FHT the following steps are used.

1) The N Hadamard measurements, $\vec{E}$, are permuted by the permutation π_1. To the permuted measurement vector, $\vec{E}_\pi$, one need only add a zero to the front of the vector. This gives $\hat{\vec{E}}_\pi = \binom{0}{\vec{E}_\pi}$.

2) The FHT is performed on $\hat{\vec{E}}_\pi$, giving a vector denoted as $\hat{\vec{S}}_\pi$.

3) The first element of $\hat{\vec{S}}_\pi$ is deleted. The permutation, π_2, is then applied to the remaining vector, forming $\hat{\vec{L}}_\pi$.

4) The vector, L_π, obtained in step 3 is then normalized (each element divided by $-[(N+1)/2]$), resulting in the spectral intensity vector.

Before the algorithm mentioned above can be performed, the permutations, π_1 and π_2, must be determined. The permutations are discussed below.

First, the generation of the permutations of π_1 are described.

1) Let $W_n^T = \begin{bmatrix} \alpha_{11} & \cdots & \alpha_{1N} \\ \vdots & & \\ \alpha_{n1} & & \alpha_{nN} \end{bmatrix}$ = the first n rows of the transpose of matrix $W = \{w_{ij}\}$.

2) Set $\pi_1(j) = \ell$ where ℓ is the integer expressed in binary notation by the sequence $\alpha_{nj}\alpha_{(n-1)j} \cdots \alpha_{1j}$. The value of the $\ell^{\underline{th}}$ element of the permuted measurement vector is set equal to the value of the $j^{\underline{th}}$ element of the original measurement vector, $\vec{E}$.

The permutations of π_2 are generated in the following manner.

1) Let W^T be the transpose of $W = \{w_{ij}\}$.

2) Let R be the matrix whose $\ell^{\underline{th}}$ column is the $j^{\underline{th}}$ column of W^T, where $\pi_1(j) = \ell$.

3) Let $P = \begin{bmatrix} p_{11} & \cdots & p_{1n} \\ \vdots & & \vdots \\ p_{N1} & \cdots & p_{Nn} \end{bmatrix}$ be the matrix where the jth column is the $(2^{j-1})^{\underline{th}}$ column of R.

4) Set $\pi_2(k) = \ell$, where k is the integer expressed in binary notation by the sequence $p_{\ell n}p_{\ell(n-1)} \cdots p_{\ell 1}$. The value of the $\ell^{\underline{th}}$ element of the permuted vector, $\hat{\vec{L}}_\tau$, is set equal to the value of the $k^{\underline{th}}$ element of the original vector.

Finally, the FHT algorithm which is compatible with the aforementioned permutations is presented.

1) Let [F(0), ..., F(N)] be the vector to be transformed. For all possible n-tuples $(\mu_{n-1}, \mu_{n-2}, \ldots, \mu_o)$, set

$$\hat{F}_o(\mu_{n-1}, \mu_{n-2}, \ldots \mu_o) = F(\sum_{j=0}^{n-1} 2^j \mu_j).$$

2) For $1 < j < n$, set

$$\hat{F}_j(\mu_{n-1}, \ldots, \mu_j, \mu_{j-1}, \ldots, \mu_o) = \hat{F}_{j-1}(\mu_{n-1}, \ldots, \mu_j, 0, \mu_{j-2}, \ldots, \mu_o) +$$

$$(-1)^{\mu_{j-1}} F_{j-1}(\mu_{n-1}, \ldots, \mu_j, 1, \mu_{j-2}, \ldots, \mu_o).$$

3) Set

$$T(m) = F_n(\mu_{n-1}, \ldots, \mu_o), \text{ where } m = \sum_{j=0}^{n-1} 2^j \mu_j.$$

[T(o), ..., T(N)] is then the Hadamard transform of [F(0), ..., F(N)].

References

1. F. Yates, *J. Roy. Stat. Soc. Supp.*, *2*, 181 (1935).
2. M. Harwit, "Hadamard Transform Analytical Systems", *Transform Techniques in Chemistry*, Edited by P. R. Griffiths, Plenum Press, New York (1978), pp. 173-197.
3. J. A. Sloane, Martin Harwit, *Applied Optics*, *15*, 107 (1976).
4. N. J. A. Sloane, T. Fine, P. G. Phillips, M. Harwit, *Applied Optics*, *8*, 2103 (1969).
5. E. D. Nelson, M. L. Friedman, *J. of the Optical Society of America*, *60*, 1664 (1970).
6. H. Hotelling, *Ann. Math. Stat.*, *15*, 297 (1944).
7. S. W. Golomb, Ed., *Digital Communications with Space Applications*, Prentice-Hall, Inc., Englewood Cliffs, New Jersey, 1964.
8. R. Thuene and S. W. Golomb, *California Institute of Technology, Jet Propulsion Laboratory, Space Programs Summary No. 37-40*, IV, *207* (1967).
9. L. D. Baumert, *California Institute of Technology, Jet Propulsion Laboratory, Space Programs Summary No. 37-43*, *IV*, 311 (1967).
10. M. Harwit, P. G. Philips, L. W. King, D. A. Briatta, Jr., *Applied Optics*, *13*, 2669 (1974).
11. J. A. Decker, Jr., *Applied Optics*, *10*, 510 (1971).
12. J. A. Decker, Jr., *Analytical Chemistry*, *44*, 127A (1972).
13. P. G. Phillips, M. Harwit, *Applied Optics*, *10*, 2780 (1971).
14. J. A. Decker, Jr., *Analysis Instrumentation*, *10* (1972).
15. Spectral Imaging, Inc., *Product Briefs and Specifications for Hadamard-Transform Spectromers*.
16. M. Harwit, P. G. Phillips, T. Fine, N. J. A. Sloane, *Applied Optics*, *9*, 1149 (1970).
17. M. H. Tai, M. Harwit, N. J. A. Sloane, *Applied Optics*, *14*, 2678 (1975).

18. N. J. A. Sloane, M. Harwit, M. H. Tai, Applied Optics, 17, 299 (1978).

19. M. Harwit, Applied Optics, 10, 1415 (1971).

20. R. D. Swift, R. B. Wattson, J. A. Decker, Jr., R. Paganetti, M. Harwit, Applied Optics, 15, 1595 (1976).

21. L. D. Baumert, in Digital Communications with Space Applications, edited by S. W. Golomb (Prentice-Hall, Englewood Cliffs, N.J., 1964) p. 51-55.

22. R. N. Ibbett, D. Aspinall, J. F. Grainger, Applied Optics, 7, 1089 (1968).

FIGURE CAPTIONS

Figure 1 -- Components used in Hadamard Transform Spectroscopy. The dotted lines indicate additional components necessary when an encoding mask utilizing reflecting and transparent slots is used instead of an encoding mask made of opaque and transparent slots.

Figure 2 -- Block diagrams of three spectrometers. The top spectrometer is a conventional monoachromator. The middle spectrometer is a singly encoded Hadamard Transform Spectrometer and the bottom spectrometer is a doubly encoded Hadamard transform spectrometer.

Figure 3 -- A $2N-1 = 13$ slot mask is stepped across a blocking mask, allowing seven linearly independent seven channel weighing designs to be illuminated by the incident radiation. A measurement of the light intensity is made at each of the seven different mask positions. An S_7 weighing design matrix is thus created.

Figure 4 -- Optics of a typical singly encoded Hadamard Transform Spectrometer.

Figure 5 -- Slit functions of a) a sufficiently wide slot to eliminate all diffraction and b) a narrow slit resulting in full diffraction.

Figure 6 -- Components of a doubly encoded Hadamard Spectrometric Imager. The two-dimensional entrance encoding mask and one-dimensional exit encoding mask allow spectral data in two-dimensions to be observed.

Figure 7 -- Optics of a Hadamard Spectrometric Imager.

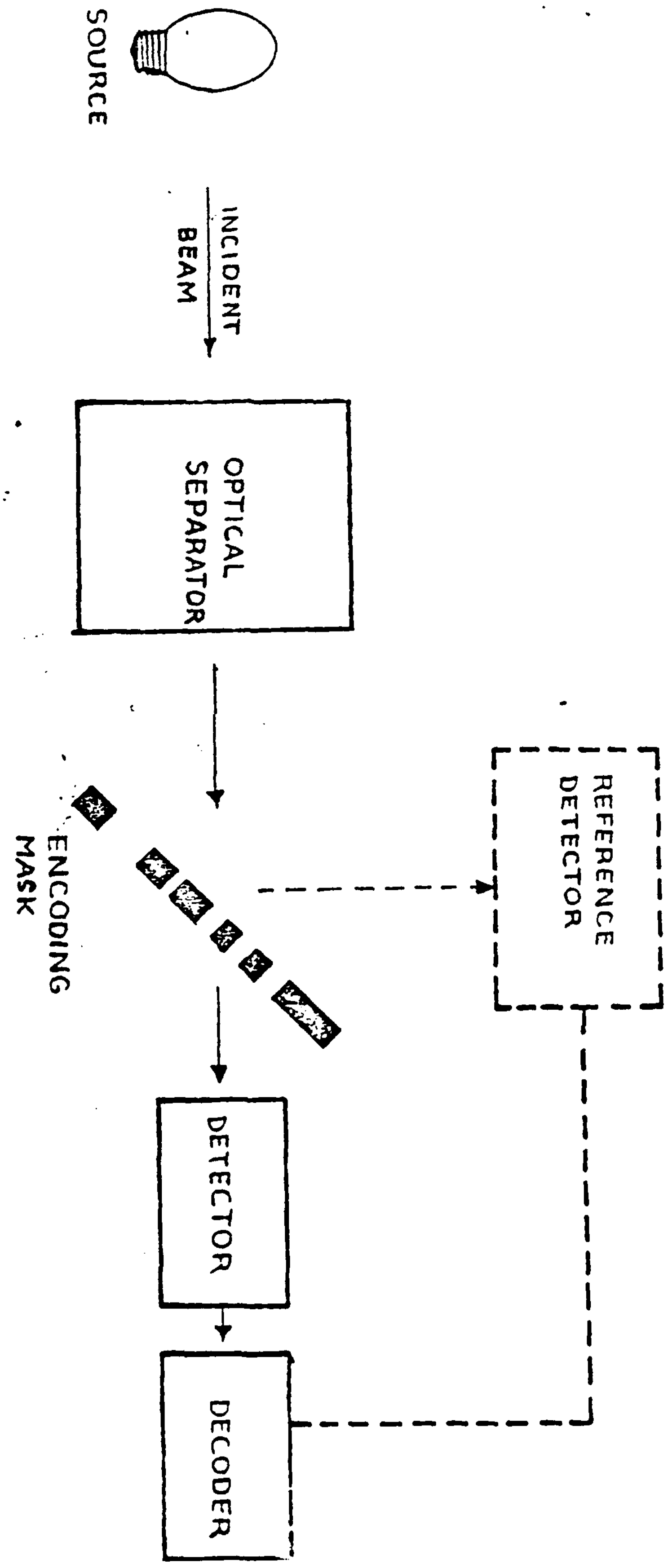
SOURCE
INCIDENT BEAM
OPTICAL SEPARATOR
REFERENCE DETECTOR
ENCODING MASK
DETECTOR
DECODER

Fig 1

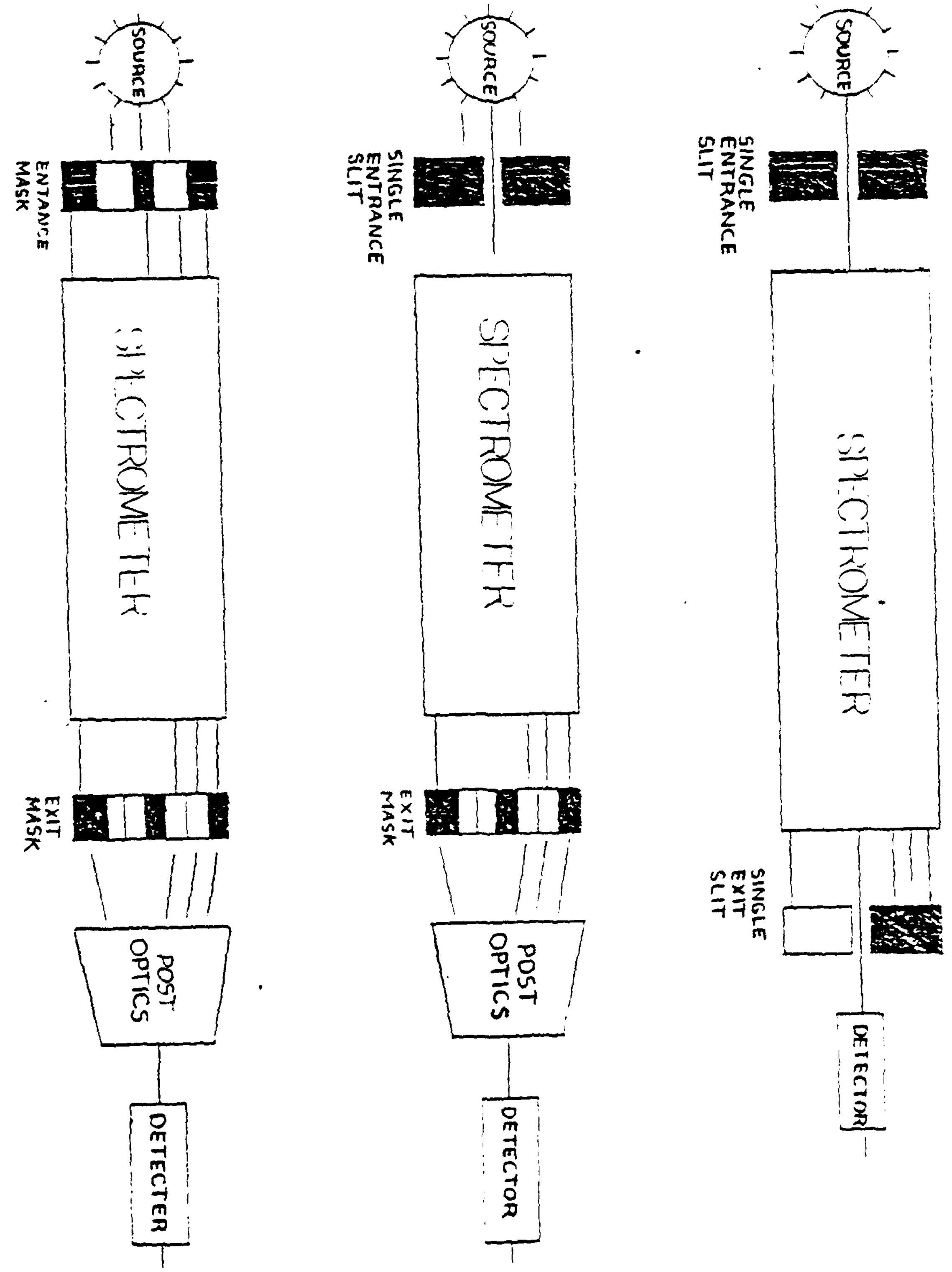
SOURCE
SINGLE ENTRANCE SLIT
SPECTROMETER
SINGLE EXIT SLIT
DETECTOR
SOURCE
SINGLE ENTRANCE SLIT
SPECTROMETER
EXIT MASK
POST OPTICS
DETECTOR
SOURCE
ENTANCE MASK
SPECTROMETER
EXIT MASK
POST OPTICS
DETECTER

Fig 2

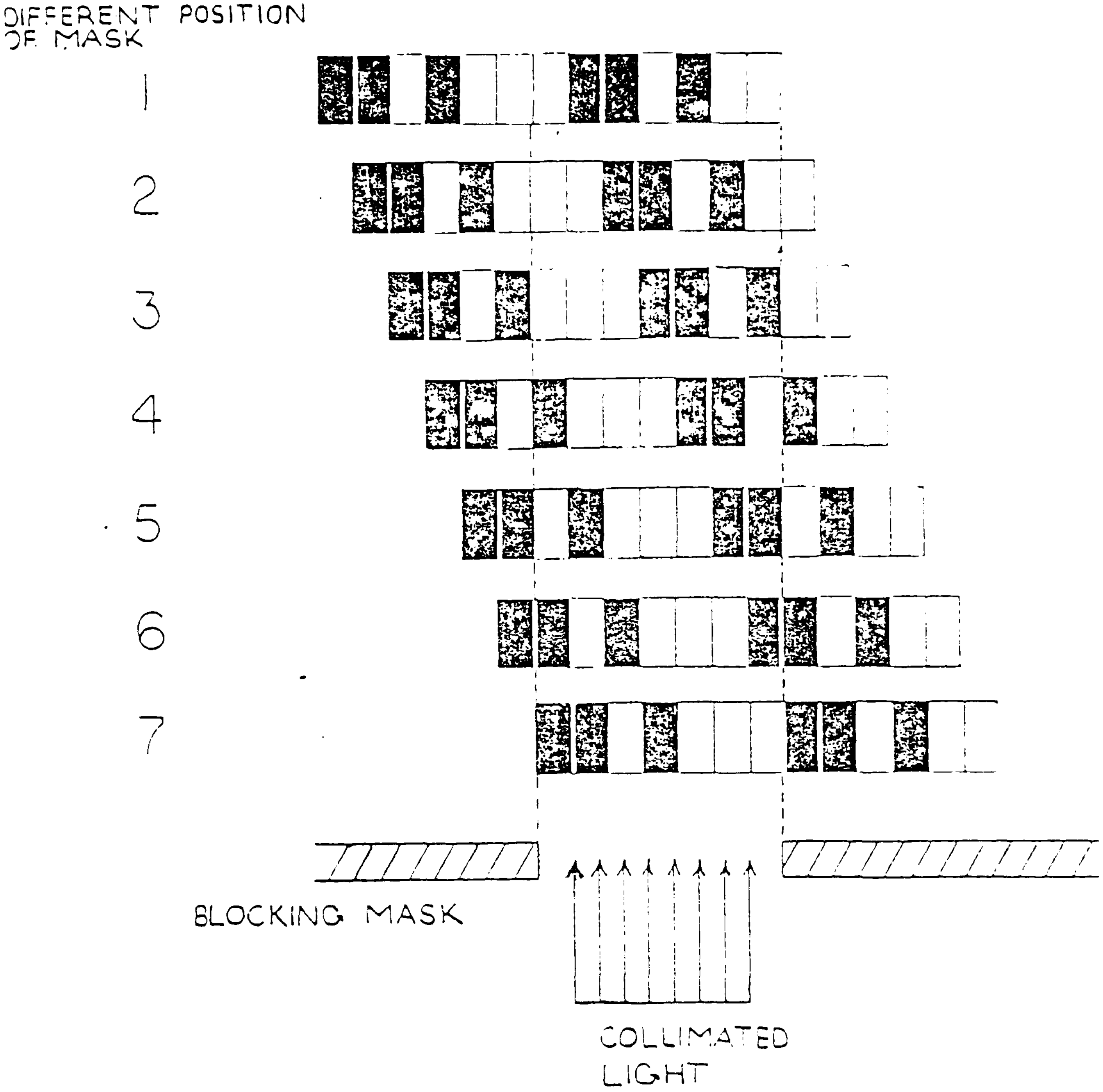
DIFFERENT POSITION OF MASK
BLOCKING MASK
COLLIMATED LIGHT

FIG. 3

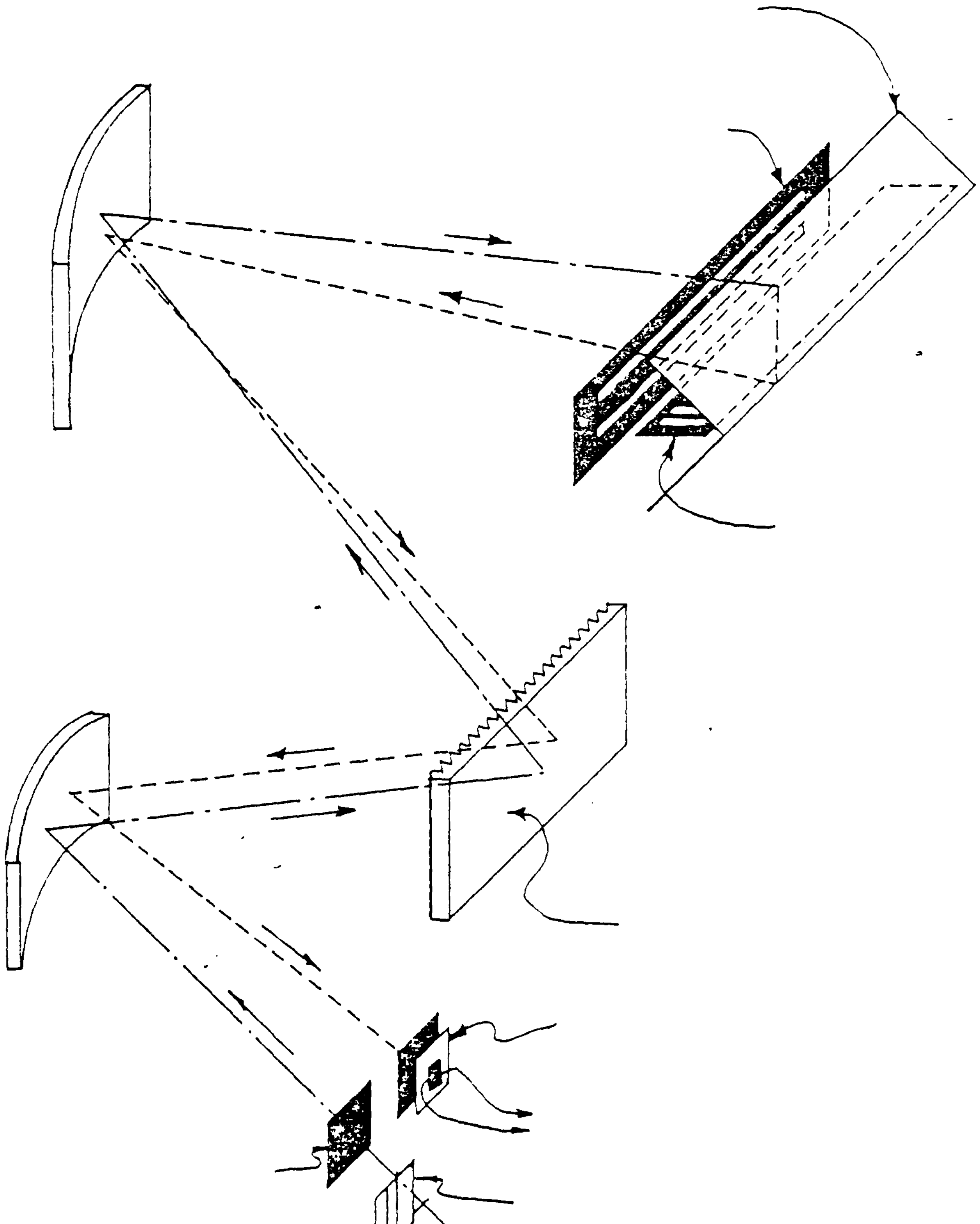

Fig 4

Fig 5a

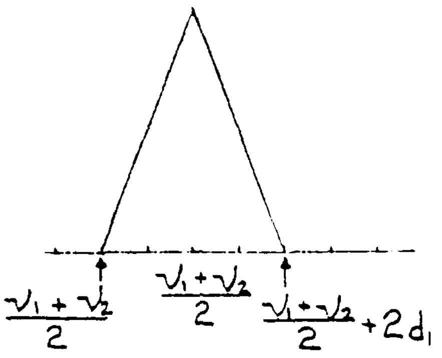
$\frac{\nu_1+\nu_2}{2}$
$\frac{\nu_1+\nu_2}{2}$
$\frac{\nu_1+\nu_2}{2}+2d_1$

Fig 5 b

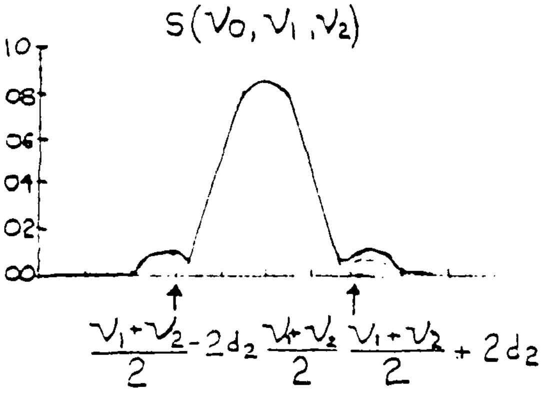
$S(\nu_0,\nu_1,\nu_2)$
10
08
06
04
02
00
$\frac{\nu_1+\nu_2}{2}-2d_2$
$\frac{\nu_1+\nu_2}{2}$
$\frac{\nu_1+\nu_2}{2}+2d_2$

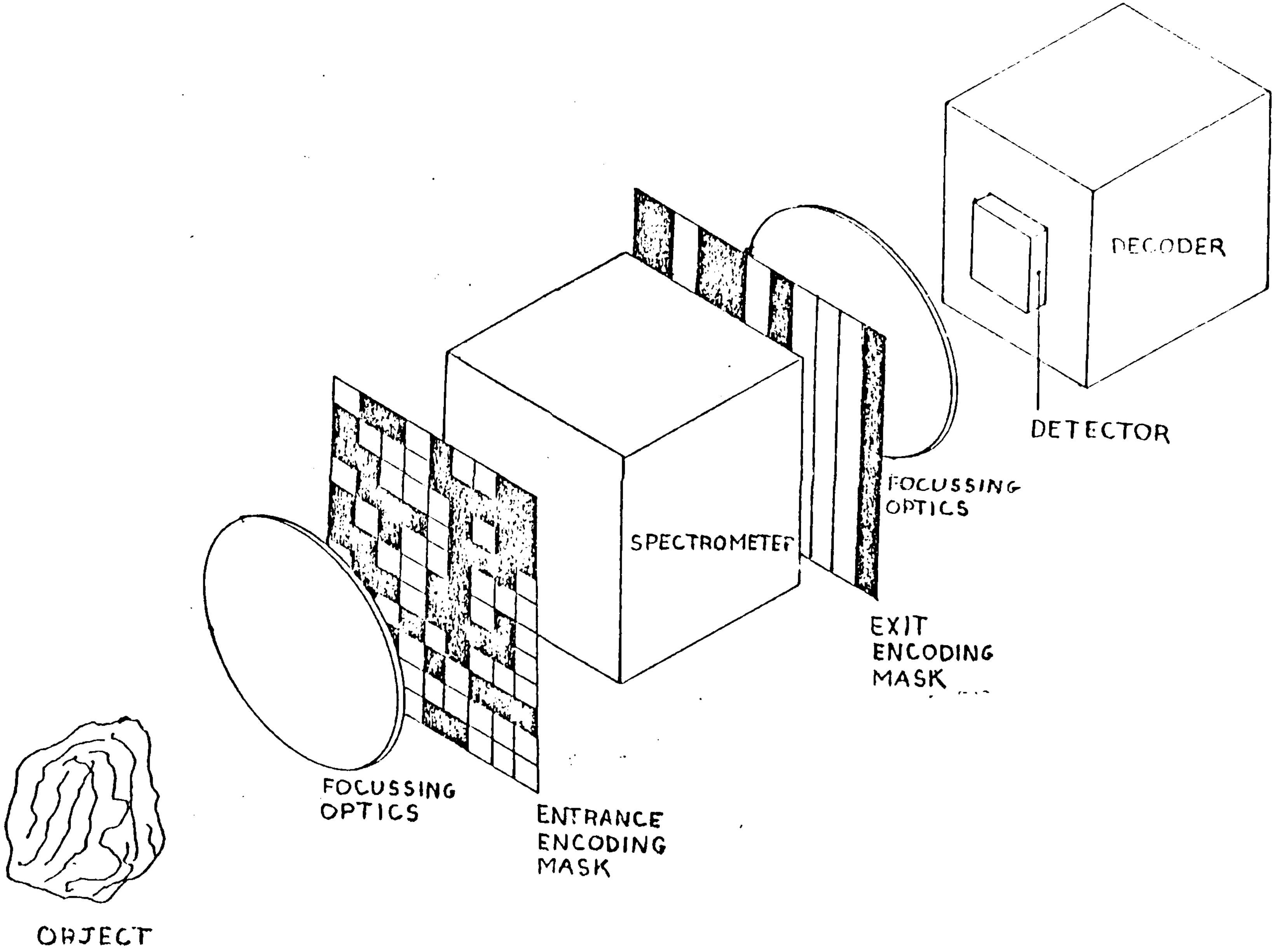
DECODER
DETECTOR
FOCUSSING OPTICS
SPECTROMETER
EXIT ENCODING MASK
FOCUSSING OPTICS
ENTRANCE ENCODING MASK
OBJECT

Fig 6

AD-A098 081 KANSAS STATE UNIV MANHATTAN DEPT OF CHEMISTRY F/G 7/4
DEVELOPMENT AND USE OF TIME RESOLVED SPECTROSCOPY.(U)
MAR 81 W G FATELEY, R M HAMMAKER AFOSR-78-3617
UNCLASSIFIED AFOSR-TR-81-0351 NL

2 OF 2

END
DATE
FILMED
5-81
DTIC

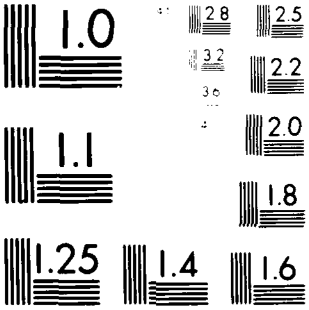
1.0
2.8
2.5
3.2
2.2
3.6
2.0
1.1
1.8
1.25
1.4
1.6

MICROCOPY RESOLUTION TEST CHART
[illegible]

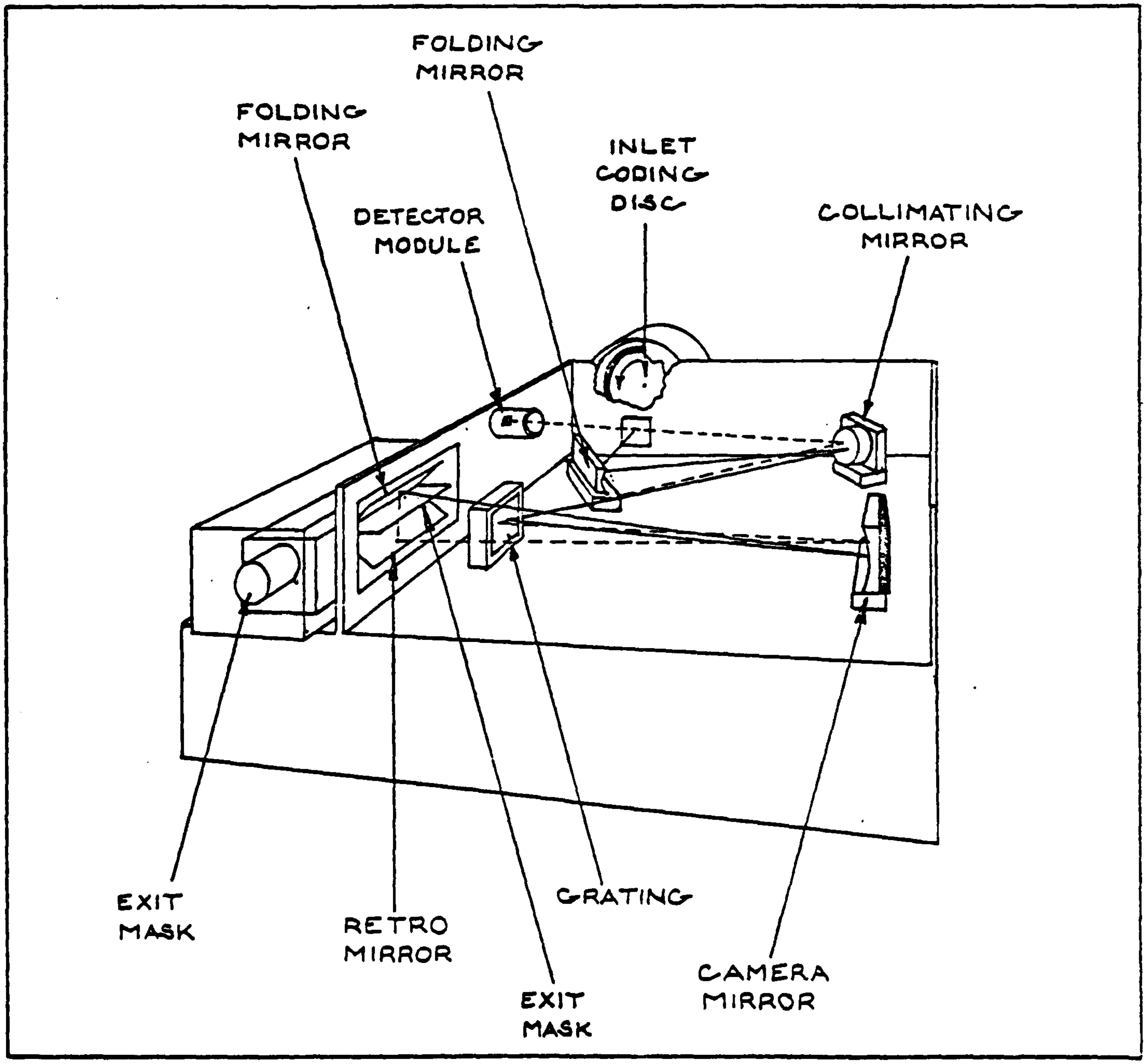
FOLDING MIRROR
FOLDING MIRROR
INLET CODING DISC
DETECTOR MODULE
COLLIMATING MIRROR
EXIT MASK
RETRO MIRROR
GRATING
EXIT MASK
CAMERA MIRROR

D.

Raman Studies of the Adduct Structure of Cl_2 and Br_2 with Piaselenole

J. J. BLAHA,* W. BRITTAIN,† C. E. MELOAN, and W. G. FATELEY‡

Department of Chemistry, Kansas State University, Manhattan, Kansas 66506

The affinity of 2,1,3-benzoselenadiazole, commonly called piaselenole, for chlorine and bromine molecules has been known for a long time. Raman spectroscopy provides a very interesting method for determining the molecular structure of these 1:1 adducts. The Raman spectrum shows the Cl_2 and Br_2 molecules in the adduct remain as a dimer molecule.

Index Headings: Raman spectroscopy; Structure analysis; Matrix isolation.

INTRODUCTION

The interest in the structure of the 1:1 adduct between piaselenole and chlorine or bromine molecules arises from the desire to remove these halogens from air streams. Previously both Cl_2 and Br_2 were removed by an oxidation-reduction reaction, but this is a very time-consuming process.[1] Recently piaselenole has been used as a scrubbing agent to form an adduct with these halogen molecules. Not only does this provide a very simple technique for removal of Cl_2 and Br_2 molecules, but it also allows us to reclaim the halogen gases which are precipitated as the adduct during the scrubbing process. The adduct is easily decomposed to halogen gas and piaselenole by the addition of water.

Piaselenole is known to have a planar, orthoquinoid structure, which undergoes a quaternarization reaction with alkyl halides.[2-4] This compound has been proven to be a valuable reagent in trace analyses.[5-9] Our attention was directed to this unique molecule because of the severity in conditions necessary to chlorinate the six member ring of piaselenole. We assumed chlorination of piaselenole would easily occur with the addition of chlorine gas; however, a yellow material was recovered that did not show aromatic ring chlorination. Additional investigation shows the same conditions necessary for the chlorination of benzene, i.e., chlorine gas, iron filings, and reflux at elevated temperatures, were necessary for the chlorination of piaselenole.[8]

Earlier workers had suggested that the yellow material which resulted from the simple addition of chlorine gas to piaselenole might be an adduct, but little proof was given for this conclusion.[10]

Received 16 March 1980.

* Present address: National Bureau of Standards, Washington, DC.

† Undergraduate research project.

‡ Research sponsored by Air Force, Office of Scientific Research, 78-3617.

We wish to present the Raman spectral data which show that the halogen remains as a dimeric molecules in these 1:1 mole ratio adducts with piaselenole.

I. EXPERIMENTAL

The piaselenole was prepared by mixing aqueous solutions of orthophenylenediamine dichloride with an excess of selenium dioxide. The precipitate formed is characterized by white needle crystals having a melting point range of 74–76°C. The infrared spectrum was also used to identify the compound as piaselenole.

The Raman spectra were obtained by conventional techniques using the 514.5-nm excitation line of the argon ion laser. The Raman scattering was observed at a 90° angle to the impinging laser beam.

The Raman spectra were obtained using two different sampling techniques: (1) samples sealed in capillary tubes, and (2) pellets which were rotated in the laser beam. The rotation of the pellet sample in the laser beam eliminated the opportunity for the sample to be decomposed by the impinging laser radiation.

The piaselenole was dissolved in a solvent and the chlorine gas was bubbled into this solution at a slow flow rate, approximately 1.5 ml/s, through a glass frit. Methyl orange was used as a visual indicator for the reaction end point. The methyl orange bleaches to a colorless solution when free chlorine gas is present. The color change signals the completion of the piaselenole-chlorine adduct formation. A second solution of piaselenole was titrated with a 0.25% by weight bromine solution. The complete formation of the bromine adduct was detected by the characteristic red color of excess bromine. The stoichemistry for both chlorine and bromine was a 1:1 mole ratio with the piaselenole. A word of warning, both adducts can be destroyed by the addition of an excess of the halogen gas. In addition, adduct decomposition was also observed from exposure to light and storage of solid samples at room temperatures.

The adduct precipitate is characterized by long needles colored yellow and yellow-orange for the chlorine and bromine adducts, respectively. The adducts were protected by immersion in the solvent and storage at 0°C. The addition of water to these adducts yield the pure white piaselenole solid and the halogen dissolved in or released from the water.

II. RESULTS AND DISCUSSION

Since both chlorine and bromine molecules are homonuclear, Raman spectroscopy is the obvious choice for the study of these adducts because the halogen vibrations are Raman active and infrared inactive.[11] The Raman

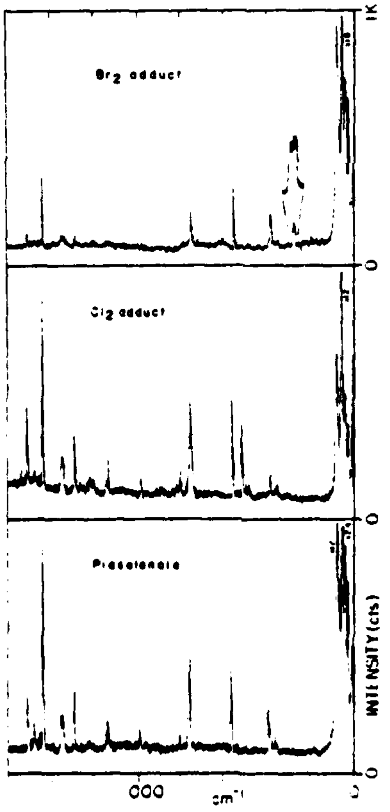

FIG. 1. Raman spectra of piaselenole and associated halogen adducts. Top: bromine adduct. Sample on rotating platform; laser, 514.5 nm; beam, ~2 nm at sample; spectral slit width, 3 cm⁻¹, time constant, 1.0 s; scan rate, 0.83 cm⁻¹/s; full scale, 1000 count. Middle: chlorine adduct. Sample on rotating platform; same conditions as for top. Bottom: piaselenole. Sample in capillary tube; same conditions as for top.

TABLE I. Frequency assignments for piaselenole and the chlorine and bromine adducts (values in cm⁻¹).[a]

Piaselenole	Cl_2 adduct	Br_2 adduct
22 S	22 S	22 S
38 S	38 S	38 S
51 VS	51 VS	51 VS
74 VS	74 VS	74 VS
159 W	158 W	158 W
173 W	172 W	172 W
	Br_2 vibration	286 W 289 M 293 W
353 W	352 W	352 W
381 M	381 M	380 W
487 W	487 W	486 W
497 W	498 W	497 W
Cl_2 vibration	507 W 514 W 521 S	
554 S	554 S	556 S
675 W	674 W	676 W
711 W	710 W	711 W
748 S	748 W	750 W
801 W	800 W	801 W
899 W	896 W	895 W
982 W	980 W	983 W
1134 W	1130 W	1133 W
1144 W	1142 W	1145 W
1223 W	1223 W	1225 W
1240 W	1239 W	1243 W
1288 M	1286 W	1289 W
1341 M	1341 W	1340 M
1347 M	1347 W	1348 M
1352 W	1350 W	1352 W
1437 VS	1435 S	1437 S
1476 W	1476 W	1475 W
1486 W	1486 W	1489 W
1496 W	1496 W	1494 W
1510 M	1508 W	1511 W
1607 W	1606 W	1608 W

[a] The frequencies are obtained from the Raman shift in Fig. 1. Abbreviations used are W, weak, M, medium, S, strong; V, very

spectra of the chlorine and bromine adducts are presented in Fig. 1 and a tabulation of the frequencies and assignments are given in Table I.

The Raman spectra of the adduct are very similar to the spectrum of piaselenole (Fig. 1). However, significant differences are observed near 514 $\mathrm{cm^{-1}}$ for the chlorine adduct and around 289 $\mathrm{cm^{-1}}$ for the bromine adduct. The Raman spectrum of piaselenole shows no scattering in this region. No additional bands due to the adducts are found in the region below 200 $\mathrm{cm^{-1}}$. Closer examination of the region shows scattering at 521, 514, and 507 $\mathrm{cm^{-1}}$ for the chlorine adduct and 293, 289, and 286 $\mathrm{cm^{-1}}$ for bromine adduct. Previous investigators have reported Raman frequencies for the solid chlorine molecule at 542, 534, and 527 $\mathrm{cm^{-1}}$ and for the solid bromine molecule at 305, 301, and 299 $\mathrm{cm^{-1}}$.[12, 13] The authors attributed these several frequencies to the various halogen isotopes. The frequencies do not indicate coupling of vibrational modes due to neighboring halogen molecules.

Earlier workers have reported Raman bands from $SeCl_4$ molecules at 375, 361, and 348 $\mathrm{cm^{-1}}$ and for $SeBr_4$ molecules at 266, 247, and 226 $\mathrm{cm^{-1}}$.[14] Additionally Se_2Cl_6 has a frequency at 367 $\mathrm{cm^{-1}}$ and Se_2Br_6 at 265 $\mathrm{cm^{-1}}$.[15] Certainly the observation of these new frequencies in the adduct cannot be due to the formation of Se—X bonds (i.e., there is no SeX in the adducts).

III. CONCLUSION

As previously noted the piaselenole spectrum is unaffected by the addition of a halogen molecule; therefore, we would not expect the piaselenole molecule to be chemically altered in the formation of the adduct.

In addition the physical appearance of the needle-like crystals for both pure piaselenole and the adduct suggest that little change has occurred in the crystal habit. Furthermore, the chlorine and bromine molecules are easily released from the adduct. Finally the spectrum of solid chlorine, Cl_2, and bromine, Br_2, is very similar to halogen adducts; we must conclude that the halogen molecules remain as dimers, i.e., Cl_2 and Br_2 in the adduct. The observed lowering of the halogen's vibrational frequencies indicates the isolation of halogen and possibly some decrease in the bond order of the halogen due to physical bonding with piaselenole.

We speculate that the association of the halogens with piaselenole occurs as a quaternary amine reaction rather than a simple association with the selenium atom. Previous investigations have shown that the quaternarization reactions are preferred over reactions with the selenium atom.[4, 16] Certainly this is a plausible model in these adducts.

---

1. Association of Official Analytical Chemists, *Official Methods of Analysis, 12th ed.* (Washington, DC, 1975).
2. V. Luzzati, Acta Cryst. **4**, 193 (1951).
3. V. S. Korobkov, A. V. Seckharov, L. P. Zubanov, and D. I. Dvorevenko, Izv. Vyssh. Uchebn. Zaved. Fiz. **11**, 158 (1968).
4. A. J. Nunn and J. T. Ralph, J. Chem. Soc. [Perkin I] **18**, 1568 (1966).
5. J. Hoste, Anal. Chim. Acta **2**, 402 (1948).
6. M. Ziegler and O. Glemser, Z. Anal. Chem. **146**, 29 (1955).
7. T. G. Bunting and C. E. Meloan, Anal. Chem. **40**, 435 (1968).
8. R. H. Hanson and C. E. Meloan, Inorg. Nucl. Chem. Lett. **7**, 461 (1971).
9. T. Bunting, "Exponentially loaded column gas chromatography and cobalt and palladium complexes of piaselenole," Doctoral Thesis, Kansas State University, Manhattan, 1967.
10. L. S. Efrose and R. M. Leviom, Zh. Obshch. Khim. **25**, 199 (1955).
11. J. E. Cahill and G. E. Leroi, J. Chem. Phys. **51**, 4514 (1969).
12. G. C. Hayward and P. J. Hendra, J. Chem. Soc. A, 643 (1967).
13. H. Stammreich and R. Forneris, Spectrochim. Acta **8**, 46 (1956).
14. W. Kiefer, Spectrochim. Acta **27 A**, 1285 (1971).
15. P. J. Hendra and P. J. D. Park, J. Chem. Soc. A, 908 (1968).
16. A. J. Nunn and J. T. Ralph, J. Chem. Soc. Dec., 6769 (1965).

E.

The CF_3 Rotor: Torsional Vibrations for Some CF_3OX and CF_3OOX Molecules

R. M. Hammaker, W. G. Fateley, Ajit S. Manocha, and D. D. DesMarteau
Department of Chemistry, Kansas State University, Manhattan, Kansas 66506, USA
B. J. Streusand† and J. R. Durig
Department of Chemistry, University of South Carolina, Columbia, South Carolina 29208, USA

The low frequency Raman spectra of CF_3OF (gas, liquid), CF_3OCl (liquid), CF_3OOH (gas, liquid), CF_3OOD (liquid), CF_3OOF (gas, liquid) and CF_3OOCl (liquid) have been recorded below 300 cm^{-1}. The spectra have been assigned and the CF_3 torsional modes were observed for all of these compounds in the liquid state. The assigned frequencies for the liquids and the calculated barriers for the vapor state are: CF_3OF, $\nu_\tau = 144\ cm^{-1}$, $V_3 = 4.64\ kcal\ mol^{-1}$; CF_3OCl, $\nu_\tau = 122\ cm^{-1}$, $V_3 = 4.6\ kcal\ mol^{-1}$; CF_3OOH, $\nu_\tau = 155\ cm^{-1}$, $V_3 = 6.0\ kcal\ mol^{-1}$; CF_3OOF, $\nu_\tau = 78\ cm^{-1}$, $V_3 = 2.9\ kcal\ mol^{-1}$; and CF_3OOCl, $\nu_\tau = 80\ cm^{-1}$, $V_3 = 3.7\ kcal\ mol^{-1}$. *The assignments are discussed and the barriers are compared to the corresponding quantities in some similar molecules.*

INTRODUCTION

Trifluoromethyl hypofluorite, CF_3OF is an important reagent in the synthesis of organic and inorganic fluorine compounds.[1] Trifluoromethyl hypochlorite, CF_3OCl, is the first member of the chloroxy perfluoralkane series, and molecules known to undergo readily free radical reactions form derivatives of CF_3OCl in which the CF_3O group is retained.[2] CF_3OOX compounds (X = H, D, F, Cl) are of special interest to the synthetic inorganic chemist.[3–9] Along with bis-trifluoromethyl trioxide,[10] CF_3OOOCF_3, they serve as key reagents for the synthesis of many highly fluorinated peroxides.[4,7–9,11–13]

CF_3OF has been studied by IR and Raman spectroscopy,[14,15] electron diffraction[16] and microwave spectroscopy.[17] More recently, Raman spectra of CF_3OF in the gas phase as well as diluted in argon matrices at 8 K have been reported.[18] The preparation, identification and characterization of CF_3OCl included only IR spectra.[2,19] More recently, complementary Raman spectra of CF_3OCl isolated in an argon matrix at 8 K have been reported.[18]

As a prelude to the investigation of the structure of the CF_3OOX series by vibrational spectroscopy,[20] electron diffraction[21] and microwave spectroscopy,[22] we reinvestigated the IR and Raman spectra of CF_3OF and CF_3OCl. While that work was in progress, the contribution by Smardzewski and Fox appeared[18] and complemented our results. The work on the vibrational spectra of CF_3OF and CF_3OCl has now been completed.[23] The detailed assignments and normal coordinate analyses for CF_3OF and CF_3OCl will be reported separately.[24] The investigation of the CF_3OOX series (X = H, D, F, Cl) by vibrational spectroscopy has now been completed.[25] The detailed assignments and normal coordinate analyses for the CF_3OOX series (X = H, D, F, Cl) will be reported separately.[26]

The observation in the Raman spectra of gases of a number of $\Delta v = 2$ transitions for the methyl torsional modes for ethyl halides,[27] dihalo- and trihaloethanes,[28] and ethanol and ethanethiol[29] suggested that $\Delta v = 2$ transitions may be observable for the trifluoromethyl torsional mode. This suggestion has been realized in some 1,1,1-trifluoroethyl halides;[30] however, a reinvestigation of bis-trifluoromethyl peroxide including the Raman spectrum of the gas[31] did not reveal any $\Delta v = 2$ transitions. The present paper deals with the CF_3 torsional mode in gaseous CF_3OF where a detailed investigation is possible based on Raman spectroscopy. Some considerations about CF_3 torsions in CF_3OCl and the CF_3OOX series (X = H, D, F, Cl) are included.

EXPERIMENTAL

The syntheses and purification of all compounds were carried out at Kansas State University. CF_3OF and CF_3OCl were prepared by the cesium fluoride catalyzed addition of F_2 and ClF, respectively, to COF_2.[32] CF_3OOH was prepared by the hydrolysis of $CF_3OOC(O)F$.[3,4] CF_3OOF and CF_3OOCl were prepared by the cesium fluoride catalyzed addition of F_2 and ClF, respectively, to CF_3OOH.[5–7] CF_3OOD was prepared from CF_3OOH by exchange with D_2O and contained some unreacted CF_3OOH. Purification was normally by vacuum line distillation. CF_3OF was contaminated by $CF_2(OF)_2$ whose separation required low temperature gas chromatography.

IR spectra (4000–160 cm^{-1}) of all compounds in the gas phase were recorded at Kansas State University using a Perkin-Elmer Model 180 IR spectrophotometer. Cells of 10 cm pathlength with AgCl windows and 15 cm pathlength with polyethylene windows were employed.

Raman spectra of all compounds as liquids were recorded at Kansas State University in a low temperature cell similar in design to that of Brown *et al.*[33] The

† Present address: Center for Catalytic Science and Technology, Department of Chemical Engineering, University of Delaware, Newark, Delaware 19711, USA.

CCC-0377-0486/80/0009-0181 $03.50

© Heyden & Son Ltd, 1980

coolant bath temperatures were as follows: CF_3OF and CF_3OCl, −196 °C; CF_3OOH, −30 °C; CF_3OOD, 0 °C; CF_3OOF, −60 °C; CF_3OOCl, −20 °C. The 514.5 nm line of Spectra-Physics Models 164-00 or 164-03 argon ion lasers was used except for CF_3OOCl where its yellow color required the ~620 nm output of a Spectra-Physics Model 375 CW dye laser with rhodamine B pumped by the Model 164-03 argon ion laser. Power levels of the laser were in the range 100–300 mW in all cases. The spectra for all compounds except CF_3OOCl were recorded on a JASCO R300 laser Raman spectrophotometer. The spectra of all the CF_3OOX compounds were recorded on a system consisting of a Spex 14018 double monochromator, a detection system consisting of the RCA C31034 photomultiplier held at −30 °C by a thermoelectric cryostat and the PARC 1140 AC quantum photometer, and homemade sample illumination optics.[25] Depolarization ratios were determined by method IV of Claassen *et al.*;[34] however, their '*f*' has not been determined for the JASCO R300 or the Spex 14018 system. For the JASCO R300, known depolarized bands gave polarization ratios between 0.75 and 0.89; such measurements have not yet been made for the Spex 14018 system.

Raman spectra of CF_3OOH and CF_3OOF as gases at ambient temperature were recorded at Kansas State University using the 514.5 nm line of the Spectra-Physics Model 164-03 argon ion laser and the Spex 14018 system. The Spex 1443A external resonating cavity with both a commercial (Cary) and a homemade[25] gas cell was employed. Power levels of the laser were 2.1–2.2 W. Gas pressures were 500 and 600 Torr, respectively, for CF_3OOH and CF_3OOF.

Spectra of gaseous CF_3OF were obtained at the University of South Carolina. Far-IR spectra below 160 cm^{-1} were recorded using the Digilab Model FTS-15B IR interferometer with 6.25 and 12.5 μm Mylar beamsplitters. A cell of 10 cm pathlength with polyethylene windows was employed. Raman spectra from 350 cm^{-1} to the Rayleigh line were obtained using the 514.5 nm line of a Spectra-Physics Model 171 argon ion laser and a Cary Model 82 laser Raman spectrophotometer. The Cary illumination system and standard gas cell were employed. Power levels of the laser were approximately 4 W with a gas pressure of 500 Torr.

RESULTS AND DISCUSSION

General

The IR (gases) and Raman spectra (liquids) below 300 cm^{-1} of all compounds are shown in Figs. 1 and 2, respectively. Additionally, the Raman spectra of three of the gases are shown in Figs. 3 and 4. The observed frequencies are listed in Tables 1 and 2. Although our IR data above 300 cm^{-1} for CF_3OF are in good agreement with Wilt and Jones,[15] between 200 and 300 cm^{-1} our spectrum differs in that our peaks are 25–28 cm^{-1} higher in frequency although the band shapes are somewhat similar. Our Raman data for both CF_3OF and CF_3OCl are consistent with those of Smardzewski and Fox.[18]

Both the CF_3OX compounds have two overlapping bands in the IR and Raman spectra between 200 and 300 cm^{-1}. Initially we assumed, following Smardzewski and Fox,[18] that both were CF_3 rocking modes, $\rho(CF_3)$, with the one in the *A'* symmetry block being stronger in the Raman and weaker in the IR. Our normal coordinate analysis[23,24] leaves little doubt that the two rocking modes, $\rho(CF_3)$, are far apart, with the one in the *A''* symmetry block for CF_3OX under C_s symmetry being in the surprisingly high frequency range of 400–500 cm^{-1}.

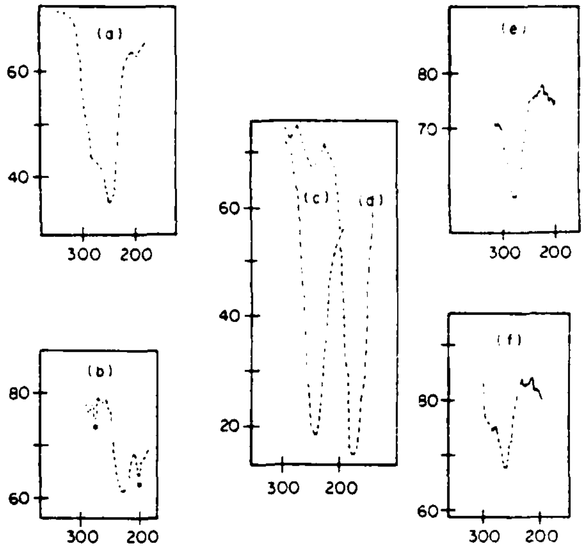

Figure 1. IR spectra below 300 cm^{-1} of gaseous (a) CF_3OF at 438 Torr, (b) CF_3OCl at 140 Torr, (c) CF_3OOH at 20 Torr, (d) CF_3OOD at 20 Torr, (e) CF_3OOF at 160 Torr, (f) CF_3OOCl at 160 Torr. All spectra were recorded using a 15 cm pathlength cell equipped with polyethylene windows. The asterisks (*) indicate bands due to HF, a decomposition product. CF_3OCl always decomposes slowly in the IR cell and some vibration-rotation bands of HF, COF_2 and SiF_4 are always detected along with some pure rotational bands of HF.

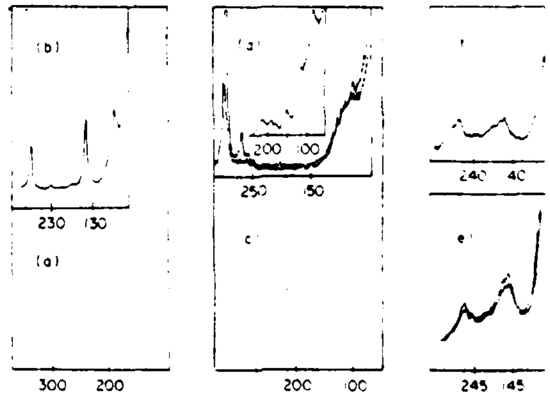

Figure 2. Raman spectra below 300 cm^{-1} of liquid (a) CF_3OF at −196 °C, (b) CF_3OOF at −60 °C, (c) CF_3OCl at −196 °C, (d) CF_3OOCl at −20 °C, (e) CF_3OOH at −30 °C, (f) CF_3OOD at 0 °C. Spectra (a) and (c) were recorded on the Jasco R300 and the remaining spectra were recorded on the Spex 14018 Raman spectrophotometer. The temperatures listed are the coolant bath temperatures in the low temperature cell. In (d) the main spectrum shows both polarizations, the inset spectrum was scanned using different instrumental parameters in order to reveal the weak features at 204, 150 and 80 cm^{-1}.

© Heyden & Son Ltd, 1980

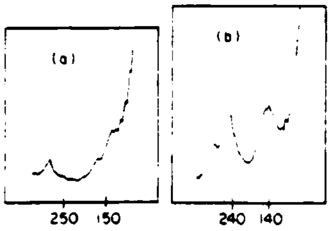

Figure 3. Raman spectra below 300 cm^{-1} of gaseous (a) CF_3OOF at 600 Torr, (b) CF_3OOH at 500 Torr. These spectra were recorded with the Spex 14018 Raman spectrophotometer.

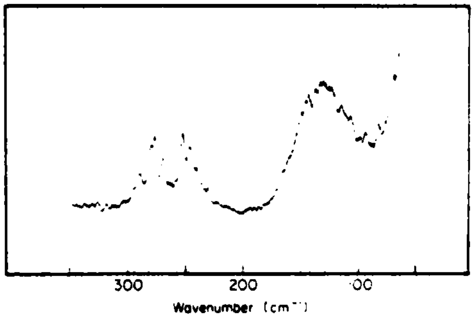

Figure 4. Raman spectrum from 350 to 60 cm^{-1} of gaseous CF_3OF. This spectrum was recorded on a Cary 82 Raman spectrophotometer with a spectral bandwidth of 4 cm^{-1}.

The lowest frequency Raman bands in the liquid are at 144 cm^{-1} and 122 cm^{-1} for CF_3OF and CF_3OCl, respectively. Since these frequencies , while low for rocking vibrations, seemed high for the CF_3 torsions, we initially suggested by analogy to CH_3 torsions[27–29] that the possibility of $\Delta v = 2$ transitions with anomaly high depolarization ratios be considered.[35,36] However, the microwave investigation of CF_3OF by Buckley and Weber[17] strongly supports the assignment of the lowest frequency in Tables 1 and 2 to $\tau(CF_3)$, not $2\tau(CF_3)$. They have shown[17] that the vibrational satellite lines have 0.4 times the intensity of the ground state lines in the microwave spectrum of gaseous CF_3OF at 194 K. This ratio is in good agreement with a population ratio of 0.38 if the $v = 1$ state in the torsional mode is 132 cm^{-1} above the $v = 0$ state. If the band at 132 cm^{-1} were due to a

Table 1. Observed frequencies (in cm^{-1}) below 300 cm^{-1} at moderate resolution

	Raman			IR	
Compound	Gas[b]	Liquid[c]	Ar matrix[d]	Gas[e]	Assignment[a]
CF_3OF	272	259 p	256	278 sh	$\rho(CF_3)$ (A′)
	246	285 sh?		252	$2\tau(CF_3)$ (A′)
	127	144 wp/dp			$\tau(CF_3)$ (A″)
CF_3OCl		220 p	239	233	$\rho(CF_3)$ (A′)
		233 sh?		220 sh??	$2\tau(CF_3)$ (A′)
		122 wp/dp			$\tau(CF_3)$ (A″)
CF_3OOH	290	275 p			$\rho(CF_3)$ (A′)
	246			244[f]	$\tau(OH)$ (A″)
	142	155 wp/dp			$\tau(CF_3)$ (A″)
CF_3OOD		273 p			$\rho(CF_3)$ (A′)
				179[f,g]	$\tau(OD)$ (A″)
		155 wp/dp			$\tau(CF_3)$ (A″)
CF_3OOF	280	283 p		278	$\rho(CF_3)$ (A′)
	132[h]	147 wp/dp			$\tau(OF)$ (A″)
		78 wp/dp			$\tau(CF_3)$ (A″)
CF_3OOCl[i]		266 p		259	$\rho(CF_3)$ (A′)
		204 p?			$2\tau(CF_3) + \tau(OCl)$ (A″)
		150 wp/dp?			$2\tau(CF_3)$ (A′)
		80 p?			$\tau(CF_3)$ (A″)

[a] These symbols are based on C_s symmetry. Only the CF_3OX compounds have C_s symmetry (Ref. 16). CF_3OOH and CF_3OOD only fail to have C_s symmetry by having a light atom off the FCOO plane, but CF_3OOF and CF_3OOCl definitely have only C_1 symmetry (Ref. 21).
[b] The data for CF_3OF is by Smardzewski and Fox (Ref. 18). The data for CF_3OOH and CF_3OOF are from this work using the Spex 14018 system.
[c] The frequencies for the CF_3OX compounds and the polarization information (p or wp/dp) for all compounds are from the JASCO R300 system. The frequencies for the CF_3OOX compounds are from the Spex 14018 system.
[d] These data are from Smardzewski and Fox (Ref. 18) at 8 K.
[e] These data are from the Perkin-Elmer 180 so the region below 160 cm^{-1} is not accessible.
[f] This band is so intense for CF_3OOH that the region from 200 to 300 cm^{-1} is obscured even in the case of CF_3OOD with some unreacted CF_3OOH. Consequently, it is impossible to observe the weaker CF_3 rocking mode expected between 250 and 300 cm^{-1}.
[g] The mid-point of a doublet seen at higher resolution at 174 and 183 cm^{-1} is taken as 179 cm^{-1} for $\tau(OD)$.
[h] Since the gas phase decomposition $CF_3OOF \rightarrow CF_4 - O_2$ occurs easily in the laser beam, the region below ~180 cm^{-1} is complicated by the pure rotational Raman spectrum of O_2. It is possible to identify this band as belonging to CF_3OOF, but the region below 80 cm^{-1} is hopelessly obscured and it is not possible to find the gas phase frequency for the band at 78 cm^{-1} in the liquid.
[i] The band at 295 cm^{-1} in the Raman spectrum of liquid CF_3OOCl is the most intense band in the spectrum and has been assigned to the OOCl bend (Refs. 25, 26). It is not included in this table since it is not involved in our discussion of the CF_3 and OCl torsions and the CF_3 rock. A weak shoulder near 290 cm^{-1} in the IR spectrum of gaseous CF_3OOCl also assigned to the OOCl bend is not included in this table either.

© Heyden & Son Ltd, 1980

Table 2. Raman spectral data[a] (300–50 cm^{-1}) for gaseous CF_3OF

ν (cm^{-1})		Assignment	
Observed	Calculated[b]		
290 281 278 271			$\rho(CF_3)$ (A′)
254	253.1	$2 \leftarrow 0$	$\tau(CF_3)$ (A′)
247	248.0	$3 \leftarrow 1$	$\tau(CF_3)$ (A′)
242	242.7	$4 \leftarrow 2$	$\tau(CF_3)$ (A′)
238	237.0	$5 \leftarrow 3$	$\tau(CF_3)$ (A′)
231	231.1	$6 \leftarrow 4$	$\tau(CF_3)$ (A′)
~132 vs, brd, dp	127.8	$1 \leftarrow 0$	$\tau(CF_3)$ (A′)

[a] All the lines from 230 to 290 cm^{-1} are polarized.

[b] The torsional transitions were calculated with a $V_3 = 1625$ cm^{-1} and an F number of 1.217 cm^{-1}.

$0 \rightarrow 2$ transition, then the $0 \rightarrow 1$ transition would be 67.5 cm^{-1} giving a population ratio of 0.61 at 194 K. This assignment then accounts for the two overlapping bands between 200 and 300 cm^{-1} as $\rho(CF_3)$ and $2\tau(CF_3)$.

For both the CF_3OX compounds the choice of $\rho(CF_3)$ and $2\tau(CF_3)$ for the bands between 200 and 300 cm^{-1} is ambiguous. In Table 1 we suggest 278 cm^{-1} and 233 cm^{-1} for $\rho(CF_3)$ in gaseous CF_3OF and CF_3OCl, respectively. However, the frequencies in the gas phase are higher than the frequencies in the condensed phase, contrary to normal expectations.[37] In general, low frequency modes tend to increase in frequency upon condensation in contrast to stretching modes which tend to decrease in frequency upon condensation. Another surprising feature is that the 252 cm^{-1} band is more intense than the 278 cm^{-1} band in the IR spectrum of gaseous CF_3OF. It is possible that the 278 cm^{-1} band is a part of a contour of a $\rho(CF_3)$ mode between 220 and 300 cm^{-1} with a center near 265 cm^{-1}, and superposition of $2\tau(CF_3)$ near 250 cm^{-1} causes an apparent maximum at 252 cm^{-1}. The higher resolution Raman spectrum of gaseous CF_3OF, treated in detail later in this section, was recorded to investigate this possibility.

In the low frequency Raman spectra in an argon matrix,[18] only one band occurs for both CF_3OF and CF_3OCl; we assume this band is $\rho(CF_3)$. However, since the argon matrix is too highly scattering to permit sufficient approach to the Rayleigh line for observation of $\tau(CF_3)$, there is no opportunity to confirm the assignment of this single Raman line to $\rho(CF_3)$ because the frequency of this line is not significantly different from the $2\tau(CF_3)$ frequency. Since matrix shifts from the gas are often only a few wavenumbers, the single matrix frequency assumed to be $\rho(CF_3)$ matches better with the 252 cm^{-1} band in the IR spectrum of gaseous CF_3OF, but we have chosen to assign $\rho(CF_3)$ to the higher frequency band at 278 cm^{-1}. For gaseous CF_3OCl the use of 233 cm^{-1} as $\rho(CF_3)$ can be justified since the 233 cm^{-1} IR band is more intense than a possible shoulder at 220 cm^{-1}. Also, 233 cm^{-1} is closer to the argon matrix frequency which usually approximates gas frequencies more closely than liquid frequencies.

Analysis of the Raman spectrum of gaseous CF_3OF (50–350 cm^{-1})

The Raman spectrum (50–350 cm^{-1}) of gaseous CF_3OF is shown in Fig. 4. The mode $\tau(CF_3)$ gives rise to the very broad, strong Raman line which appears to be centered at about 132 cm^{-1}; this band is clearly depolarized. The band has the same appearance as those observed for the CF_3 torsions in the CF_3CH_2X compounds.[30] In addition to this broad depolarized band, there are two weaker polarized lines centered at 254 and ~280 cm^{-1}. The higher frequency band has apparent Q-branches at 290, 281, 278 and 271 cm^{-1} whereas the lower frequency line is made up of a series of Q-branches beginning at 254 cm^{-1} with subsequent Q-branches at 247, 242 and 231 cm^{-1} and possibly at 238 cm^{-1}. These Q-branches have decreasing intensity with decreasing frequency and the band appearance is similar to the CF_3 torsional overtones for the CF_3CH_2X compounds.[30] Therefore we initially assigned the Q-branches at 254, 247 and 252 cm^{-1} to the $2 \leftarrow 0$, $3 \leftarrow 1$, and $4 \leftarrow 2$ torsional energy level transitions (see Table 2).

These observed Raman lines for the torsional overtones ($\Delta v = 2$) were used to calculate the potential terms, V_3 and V_6, of the internal rotation Hamiltonian:

$$H = Fp^2 + \tfrac{1}{2}[V_3(1-\cos 3\theta) + V_6(1-\cos 6\theta)]$$

by utilizing a computer program previously described[27] so that the calculated differences in the torsional energy levels reproduced the observed 'double jump' frequencies. 70 sine and 70 cosine functions were used as a basis set. The F number can be considered as the reciprocal of an effective mass for the torsional vibration. It is defined as

$$F = h^2(8\pi^2)^{-1}[I_\alpha(1 - \sum_{g=1}^{3} \lambda_g^2 I_\alpha / I_g)]^{-1}$$

where I_α is the moment of inertia of the internal (CF_3) top, and λ_g is the cosine of the angle between the top axis and the gth principal axis of the entire molecule. With the structural parameters obtained from the electron diffraction study,[16] an F number of 1.217 cm^{-1} (13.85 amu Å^2) was calculated. With this F number and the first five observed double jumps, a V_3 of 1625 ± 21 cm^{-1} (4.64 kcal mol^{-1}) was calculated and the V_6 term had a value of -20 ± 8 cm^{-1}. The fit of the observed and calculated transitions is shown in Table 2.

Torsional vibrations in CF_3OCl and the CF_3OOX series

Since it has not been possible to obtain Raman spectra of gaseous CF_3OCl, it must be treated by analogy to CF_3OF. Assuming a 10% decrease in $\tau(CF_3)$ upon going from the liquid (122 cm^{-1}), we place $\tau(CF_3)$ near 110 cm^{-1} for gaseous CF_3OCl. Thus, the IR band at 233 cm^{-1} in gaseous CF_3OCl seems sufficiently removed from $2\tau(CF_3)$ and therefore can be most reasonably assigned as $\rho(CF_3)$. The band in the argon matrix at 239 cm^{-1} is then most reasonably assigned as $\rho(CF_3)$ as in Table 1. This result is consistent with our view expressed earlier that the single band between 200 and 300 cm^{-1} in the Raman spectra of CF_3OF and CF_3OCl in the argon matrix is probably $\rho(CF_3)$.

© Heyden & Son Ltd, 1980

Our normal coordinate analysis[23,24] yields a potential energy distribution in which a 110 cm^{-1} frequency is 96% $\tau(CF_3)$. Using a reasonable geometry for CF_3OCl,[23,24] $\tau(CF_3)$ near 110 cm^{-1} corresponds to a V_3 near 4.2 kcal mol^{-1}. This value is in reasonable agreement with the barrier in CF_3OF but much larger than values for several CF_3 rotors in other C_s molecules such as: $CF_3C(O)H$ and $CF_3C(O)D$, between 0.5 and 0.9 kcal mol^{-1};[38] $CF_3C(O)F$, 1.4 kcal mol^{-1};[38] $CF_3C(O)Cl$, 1.7 kcal mol^{-1};[38] CF_3NO, 0.4 kcal mol^{-1}.[39] For CH_3 rotor analogies to the CF_3 rotors already mentioned, the results for V_3 are: $CH_3C(O)H$, 1.2 kcal mol^{-1};[40] $CH_3C(O)F$, 1.0 kcal mol^{-1};[40] $CH_3C(O)Cl$, 1.3 kcal mol^{-1};[40] CH_3NO, 1.1 kcal mol^{-1}.[41] The values of V_3 for the CH_3 rotor minus the values of V_3 for the corresponding CF_3 rotor range from -0.7 kcal mol^{-1} to $+0.4$ kcal mol^{-1}. Assuming CH_3 and CF_3 rotors with identical frames will have differences in V_3 values within this range, a V_3 value of 3.1 kcal mol^{-1}[40] for CH_3OCl would predict a V_3 value of 2.4–3.5 kcal mol^{-1} for CF_3OCl. Thus, a V_3 value for CF_3OCl above 3.0 kcal mol^{-1} is plausible and a value above 4.0 kcal mol^{-1} does not seem unreasonable.

For the CF_3OOX series the region 200–300 cm^{-1} is somewhat different. Gaseous CF_3OOH and CF_3OOD, containing some CF_3OOH, both have very intense IR bands at 244 cm^{-1} due to $\tau(OH)$ which completely obscures the 200–300 cm^{-1} region. Gaseous CF_3OOF has one IR band at 278 cm^{-1} which is assigned to $\rho(CF_3)$ and the corresponding Raman bands at 280 cm^{-1} (gas) and 283 cm^{-1} (liquid) are similarly assigned. Gaseous CF_3OOCl has one IR band at 259 cm^{-1} which is assigned to $\rho(CF_3)$ and the corresponding Raman band in the liquid at 266 cm^{-1} is similarly assigned. Liquid CF_3OOCl has its strongest Raman band at 295 cm^{-1} with a surprisingly weak corresponding IR shoulder near 290 cm^{-1}. These bands are assigned as the OOCl bend and were not included in Table 1.

In the Raman spectra of liquid CF_3OOH and CF_3OOD there are bands at 275 and 273 cm^{-1}, respectively, and at 155 cm^{-1} in the spectra of both. Assuming that the OH and OD torsions would be weak and broadened in the Raman spectra of the liquids, we assign the bands near 275 cm^{-1} to $\rho(CF_3)$ and the bands at 155 cm^{-1} to $\tau(CF_3)$, in analogy to CF_3OF. The Raman spectrum of gaseous CF_3OOH has bands at 246 and 142 cm^{-1} and a weak band at 290 cm^{-1} which are assigned as $\tau(OH)$, $\tau(CF_3)$ and $\rho(CF_3)$, respectively. For gaseous CF_3OOH it would be possible to assign the Raman band at 290 cm^{-1} as $2\tau(CF_3)$ rather than $\rho(CF_3)$ although 290 cm^{-1} is greater than twice 142 cm^{-1}. Inspection of the gas phase Raman spectrum shows that there could be a band near 270 cm^{-1} as well. This 270 cm^{-1} band, close to the Raman frequency of 275 cm^{-1} in the liquid, could be $\rho(CF_3)$. However, we prefer to assign the 290 cm^{-1} band as $\rho(CF_3)$ and assume $2\tau(CF_3)$ is too weak to be observed or gives rise to the questionable band near 270 cm^{-1}. For the Raman spectra of liquid CF_3OOH and CF_3OOD where $\tau(CF_3)$ is 155 cm^{-1}, there could be additional bands near 300 cm^{-1} due to $2\tau(CF_3)$. Thus, the CF_3OOH and CF_3OOD Raman spectra are consistent with the presence of weak bands due to $2\tau(CF_3)$ overlapping the $\rho(CF_3)$ region both in the liquid and gaseous samples, in analogy to the CF_3OX compounds. However, the situation is not nearly as well defined as for CF_3OF. The shift of $\tau(CH_3)$ from 155 cm^{-1} in the liquid to 142 cm^{-1} in the gas in the spectra of CF_3OOH is 10%, which is consistent with the similar observation for CF_3OF. Our normal coordinate analysis[26] has a potential energy distribution in which the 142 cm^{-1} frequency is 95% $\tau(CF_3)$ in CF_3OOH.

In the Raman spectrum of liquid CF_3OOF, bands are observed at 283, 147 and 78 cm^{-1} and are assigned to $\rho(CF_3)$, $\tau(OF)$ and $\tau(CF_3)$, respectively. The Raman spectrum of gaseous CF_3OOF contains bands at 280 cm^{-1} and 132 cm^{-1} which are assigned to $\rho(CF_3)$ and $\tau(OF)$, respectively. For liquid CF_3OOF it would be possible to assign the Raman band at 283 cm^{-1} as $2\tau(OF)$ rather than $\rho(CF_3)$ on the basis that it is close to two times 147 cm^{-1}, but then there is no band below 300 cm^{-1} for $\rho(CF_3)$. In gaseous CF_3OOF the Raman band at 280 cm^{-1} is too far from twice 132 cm^{-1} to be $2\tau(OF)$. For liquid CF_3OOF it would be possible to assign the Raman band at 147 cm^{-1} as $2\tau(CF_3)$ rather than $\tau(OF)$ on the basis of twice 78 cm^{-1}, but then there is no band for assignment to $\tau(OF)$. It is possible that weak bands corresponding to $2\tau(OF)$ and $2\tau(CF_3)$ may underlie $\rho(CF_3)$ and $\tau(OF)$, respectively, but no obvious evidence for this appears in the spectra in Fig. 2. It should be pointed out that the spectrum is badly obscured by the pure rotational Raman spectrum of O_2 from the decomposition of CF_3OOF to CF_4 and O_2. However, on the basis of the intensity of the 132 cm^{-1} Raman line, we believe it is not due to the rotational spectrum of O_2. It appears to shift to 147 cm^{-1} with liquefaction. It is not possible to get sufficiently close to the Rayleigh line to search for the gas phase Raman band corresponding to the band at 78 cm^{-1} in the liquid. By analogy to CF_3OF and CF_3OOH we reduce the Raman frequency of 78 cm^{-1} in the liquid by 10%, which gives 70 cm^{-1} as an approximation to the gas phase value for $\tau(CF_3)$. Our normal coordinate analysis has a potential energy distribution in which the 70 cm^{-1} frequency is 95% $\tau(CF_3)$ but the 132 cm^{-1} frequency is only 70% $\tau(OF)$ with 10% each from changes in the FCO and COO angles in CF_3OOF.[25,26]

The assignment of bands between 200 and 300 cm^{-1} in the Raman spectrum of liquid CF_3OOCl has already been given. Liquid CF_3OOCl does not have any Raman bands below 200 cm^{-1} that are as prominent as those in CF_3OOH, CF_3OOD and CF_3OOF; however, there are very weak bands at 80, 150 and 204 cm^{-1}. Depolarization results are uncertain but the 80 and 204 cm^{-1} bands appear to be polarized. We suggest the following very tentative assignments: 80 cm^{-1} as $\tau(CF_3)$, 150 cm^{-1} as $2\tau(CF_3)$ and 204 cm^{-1} as $2\tau(CF_3)+\tau(OCl)$. With the coolant bath at −20 °C in the low temperature cells we expect only transitions from the vibrational ground state of CF_3OOCl to be observed. These Raman bands could be $\tau(CF_3)$, $\tau(OCl)$ and one nonfundamental or two nonfundamentals and either $\tau(CF_3)$ or $\tau(OCl)$. Since CF_3OOH and CF_3OOCl have the same C—O and O—O bond lengths,[21] we assume that they have similar force constants for the CF_3 torsion. Since CF_3OOF has a shorter O—O and a longer C—O bond than CF_3OOH and CF_3OOCl, we use the values of the force constants for the CF_3 torsions in CF_3OOH and CF_3OOF to establish a probable limiting range of force constant values for the CF_3 torsion in CF_3OOCl. Using this

© Heyden & Son Ltd, 1980

range[25,26] of 0.02–0.01 mdyne Å rad^{-2} and the treatment of Fateley and Miller,[42] the range of $\tau(CF_3)$ in the gas phase is 60–87 cm^{-1}. Reducing the liquid frequency by 10% gives 72 cm^{-1} for the CF_3 torsion in gaseous CF_3OOCl.

Since CF_3OOF has a shorter O—O bond[21] than CF_3OOCl and CF_3OOH, we assume that the force constant for the OCl torsion in CF_3OOCl is much smaller than the force constant for the OF torsion in CF_3OOF which is in analogy to the force constant for the OH torsion in CF_3OOH, being smaller than the force constant for the OF torsion in CF_3OOF. Thus, with a much smaller force constant for the OX torsion and a much larger X mass and reduced moment of inertia for internal rotation, CF_3OOCl would be expected to have $\tau(OCl)$ in the gas phase much lower than 132 cm^{-1} for $\tau(OF)$ in gaseous CF_3OOF. Then the bands at 204 cm^{-1} and 150 cm^{-1} in the Raman spectrum of liquid CF_3OOCl are not fundamentals and the band at 80 cm^{-1}, estimated to be 72 cm^{-1} in the gaseous state, is either $\tau(CF_3)$ or $\tau(OCl)$. As indicated above, the choice is $\tau(CF_3)$, in order to keep the force constant for the CF_3 torsion in the probable limiting range of 0.02–0.01 mdyne Å rad^{-2}. The 150 cm^{-1} band may then be assigned to $2\tau(CF_3)$ with the 204 cm^{-1} band assigned as $2\tau(CF_3)+\tau(OCl)$.

Therefore, with $2\tau(CF_3)+\tau(OCl)=204\ \text{cm}^{-1}$ and $2\tau(CF_3)=150\ \text{cm}^{-1}$, one obtains 54 cm^{-1} for $\tau(OCl)$ and a 10% reduction gives 49 cm^{-1} for this mode in the gas phase. The admittedly uncertain polarization data are somewhat disturbing, but other unexpected polarization results have also been observed in CF_3OOF and CF_3OOCl.[25,26] Under C_s symmetry, $\tau(CF_3)$ and $2\tau(CF_3)+\tau(OCl)$ would be depolarized and $2\tau(CF_3)$ would be polarized. Our uncertain polarization data make $\tau(CF_3)$ and $2\tau(CF_3)+\tau(OCl)$ appear to be polarized while $2\tau(CF_3)$ is only weakly polarized. Such a result is possible under the C_1 symmetry that CF_3OOCl possesses; however, in CF_3OOF, which is also of C_1 symmetry, both $\tau(CF_3)$ and $\tau(OF)$ are so weakly polarized as to be indistinguishable from being depolarized. We would have expected similar behavior in CF_3OOCl; perhaps the large angles of twist in the two CF_3OOCl conformers[21] may contribute to this result. Our normal coordinate analysis has a potential energy distribution in which the 72 cm^{-1} frequency is 82% $\tau(CF_3)$ with a 10% contribution from $\tau(OCl)$ and a 5% contribution from the OOCl bend. The 49 cm^{-1} band is 84% $\tau(OCl)$ with a 12% contribution from $\tau(CF_3)$.[25,26]

The force constant values [25,26] for the CF_3 and OX torsions can be used to estimate rotational barriers from the relation $V_n=(2K_\theta/n^2)$. The general term in the full form of the potential energy as a function of the internal torsional angle θ may be expressed as

$$V(\theta)=\frac{V_n}{2}(1-\cos n\theta \qquad (1)$$

Using a MacLaurin series expansion for small θ gives

$$V(\theta)=V_n(n/2)^2\theta^2 \qquad (2)$$

For a simple harmonic potential where K_θ is a torsional force constant

$$V(\theta)=(K_\theta/2)\theta^2 \qquad (3)$$

Equating coefficients of like terms between Eq. (2) and (3) gives

$$V_n=(2K_\theta/n^2) \qquad (4)$$

For $V(\theta)$ in kcal mol^{-1} and θ in radians, the units of V_n must be kcal mol^{-1} rad^{-2}. If K_θ is in mdyne Å rad^{-2} molecule^{-1}, a conversion factor of 143.9 kcal mol^{-1}, equivalent to 1 mdyne Å rad^{-2} molecule^{-1}, is needed and the 2 on the right-hand side of Eq. (4) becomes 287.9. The final working equation is

$$V_n(\text{kcal mol}^{-1}\ \text{rad}^{-2})=(287.9/n^2)K_\theta\ (\text{mdyne Å rad}^{-2}\ \text{molecule}^{-1}) \qquad (5)$$

The use of this equation requires consideration of the details of the programs used in the normal coordinate analysis. We used the GMAT program of Schachtschneider.[43] For the CF_3 torsion where $n=3$, the substitution $n=3$ on the right-hand side of Eq. (5) has already been taken into account in GMAT by having three rows for the coordinate, so $n=1$ must be used to give $V_3=287.9K_\theta$ in Eq. (5). For the OX torsion GMAT has only one row for the coordinate, so $n=2$ is used in Eq. (5) to give $V_2=(287.9/4)K_\theta$.

For the CF_3 torsion the results for V_3 are: CF_3OF, 4.8 kcal mol^{-1}; CF_3OCl, 4.6 kcal mol^{-1}; CF_3OOH, 6.0 kcal mol^{-1}; CF_3OOF, 2.9 kcal mol^{-1}; and CF_3OOCl, 3.7 kcal mol^{-1}. For the OX torsion the results for V_2 are: CF_3OOH, 2.5 kcal mol^{-1}; CF_3OOD, 2.5 kcal mol^{-1}; CF_3OOF, 17 kcal mol^{-1}; and CF_3OOCl, 3.6 kcal mol^{-1}. The values of 3.0–6.0 kcal mol^{-1} for the CF_3 rotational barrier are consistent with the earlier report[44] of 5.4 kcal mol^{-1} in $(CF_3)_2O_2$ but much higher than the more recent value[31] of 0.73 kcal mol^{-1}. The values for the OX rotational barrier for CF_3OOH and CF_3OOCl are similar as might be expected. For CF_3OOF the result is much larger but still well below the value for O_2F_2. This is consistent with the chemical evidence that, while CF_3OOF departs significantly from the other more typical peroxides in the direction of the anomalous compound O_2F_2, CF_3OOF is, nevertheless, more like H_2O_2 or CF_3OOH than like O_2F_2.[21]

Acknowledgement

The authors gratefully acknowledge the financial support of this study by the National Science Foundation by Grants CHE-79-20763 and CHE-78-04077.

REFERENCES

1. C. J. Hoffman, *Chem. Rev.* **64**, 91 (1964).
2. C. J. Schack and W. Maya, *J. Am. Chem. Soc.* **91**, 2902 (1969).
3. R. L. Talbott, *J. Org. Chem.* **33**, 2095 (1968).
4. P. A. Bernstein, F. A. Hohorst and D. D. DesMarteau, *J. Am. Chem. Soc.* **93**, 3882 (1971).
5. D. D. DesMarteau, *Inorg. Chem.* **11**, 193 (1972).
6. C. T. Ratcliffe, C. V. Hardin, L. R. Anderson and W. B. Fox, *J. Am. Chem. Soc.* **93**, 3886 (1972).
7. N. Walker and D. D. DesMarteau, *J. Am. Chem. Soc.* **97**, 13 (1975).

© Heyden & Son Ltd, 1980

8. P. A. Bernstein and D. D. DesMarteau, *J. Fluorine Chem.* **2**, 315 (1973).
9. F. A. Hohorst and D. D. DesMarteau, *Inorg. Chem.* **13**, 715 (1974).
10. L. R. Anderson and W. B. Fox, *J. Am. Chem. Soc.* **89**, 4313 (1967); P. G. Thompson, ibid. **89**, 4316 (1967).
11. F. A. Hohorst, D. D. DesMarteau, L. R. Anderson, D. E. Gould and W. B. Fox, *J. Am. Chem. Soc.* **95**, 3866 (1973).
12. F. A. Hohorst and D. D. DesMarteau, *J. Chem. Soc. Chem. Commun.* **386** (1973).
13. F. A. Hohorst, J. V. Paukstelis and D. D. DesMarteau, *J. Org. Chem.* **39**, 1298 (1974).
14. R. T. Lagemann, E. A. Jones and P. J. H. Woltz, *J. Chem. Phys.* **20**, 1768 (1952).
15. P. M. Wilt and E. A. Jones, *J. Inorg. Nucl. Chem.* **30**, 2933 (1968).
16. F. P. Diodati and L. S. Bartell, *J. Mol. Struct* **8**, 395 (1971).
17. P. Buckley and J. P. Weber, *Can. J. Chem.* **52**, 942 (1974).
18. R. R. Smardzewski and W. B. Fox, *J. Fluorine Chem.* **6**, 417 (1975).
19. D. E. Gould, L. R. Anderson, D. E. Young and W. B. Fox, *J. Chem. Soc. Chem. Commun.* 1564 (1968).
20. D. D. DesMarteau and R. M. Hammaker, unpublished studies.
21. C. J. Marsden, D. D. DesMarteau and L. S. Bartell, *Inorg. Chem.* **16**, 2359 (1977).
22. D. D. DesMarteau, Y. S. Li and J. R. Durig, *Inorg. Chem.* **19**, in press.
23. Jeng-Chung Kuo, MS thesis, Kansas State University, Manhattan, Kansas (1978).
24. J. C. Kuo, D. D. DesMarteau, W. G. Fateley, R. M. Hammaker, C. J. Marsden and J. D. Witt, *J. Raman Spectrosc.*, in press.
25. A. S. Manocha, MS thesis, Kansas State University, Manhattan, Kansas (1978).
26. A. S. Manocha, D. D. DesMarteau, R. M. Hammaker and C. J. Marsden, in preparation.
27. J. R. Durig, W. E. Bucy, L. A. Carreira and C. J. Wurrey, *J. Chem. Phys.* **60**, 1754 (1974).
28. J. R. Durig, W. E. Bucy and C. J. Wurrey, *J. Chem. Phys.* **60**, 3293 (1974).
29. J. R. Durig, W. E. Bucy, C. J. Wurrey and L. A. Carreira, *J Phys. Chem.* **79**, 988 (1975).
30. A. D. Lopata and J. R. Durig, *J. Raman Spectrosc* **6**, 61 (1977).
31. J. R. Durig, W. E. Bucy and W. J. Natter, *J. Raman Spectrosc* **6**, 257 (1977).
32. M. Lustig, A. R. Pitochelli and J. K. Ruff, *J. Am. Chem Soc.* **89**, 2841 (1967).
33. C. W. Brown, A. G. Hopkins and F. P. Daly, *Appl. Spectrosc.* **28**, 194 (1974).
34. H. H. Claassen, H. Selig and J. Shamir. *Appl. Spectrosc.* **23**, 8 (1969).
35. R. M. Hammaker and D. D. DesMarteau, *Raman Newslett.* No. 80 (7 August 1975).
36. R. M. Hammaker and D. D. DesMarteau, Paper 451, Pittsburgh Conference on Analytical Chemistry and Applied Spectroscopy, Cleveland, Ohio (March 1976).
37. W. G. Fateley, I. Matsubara and R. E. Witkowski, *Spectrochim Acta* **20**, 1461 (1964).
38. C. V. Berney, *Spectrochim. Acta Part A* **27**, 663 (1971)
39. H. F. Shurvell, S. C. Dass and R. D. Gordon. *Can. J. Chem* **52**, 3149 (1974).
40. J. R. Durig, S. M. Craven and W. C. Harris, in *Vibrational Spectra and Structure*, Vol. I, ed. by J. R. Durig. Marcel Dekker, New York (1972)
41. D Coffey Jr, C. O. Britt and J. E. Boggs, *J. Chem. Phys.* **49**, 591 (1968).
42. W. G. Fateley and F. A. Miller, *Spectrochim. Acta* **17**, 857 (1961).
43. J. H. Schachtschneider, Vibrational analysis of polyatomic molecules V and VI. Technical Reports No. 231–64 and 57–65. Shell Development Co., Houston, Texas (1964, 1965).
44. J. R. Durig and D. W. Wertz, *J. Mol. Spectrosc.* **25**, 457 (1968).

Received 13 December 1979

© Heyden & Son Ltd, 1980

F.

Vibrational Spectra and Normal Coordinate Analysis of CF_3OF and CF_3OCl

J. C. Kuo, D. D. DesMarteau, W. G. Fateley and R. M. Hammaker
Department of Chemistry, Kansas State University, Manhattan, Kansas 66506 USA

C. J. Marsden†
Department of Chemistry, University of Michigan, Ann Arbor, Michigan 48109, USA

J. D. Witt‡
Corporate Chemical Research Laboratory, Allied Chemical Company, Morristown, New Jersey 07960, USA

The IR spectra (1400 cm^{-1} to 160 cm^{-1}) of the gases at ambient temperature and the Raman spectra (below 1400 cm^{-1}) of the liquids near −196 °C are reported for CF_3OF and CF_3OCl. All fundamentals are assigned under C_s symmetry and the results of a normal coordinate analysis are presented. The assignments of Smardzewski and Fox are adopted with one exception for both CF_3OF and CF_3OCl: the CF_3 rock of A'' symmetry is assigned near 430 cm^{-1} and the two bands between 200 cm^{-1} and 300 cm^{-1} are assigned to an A' fundamental, involving CF_3 rocking and COX bending and a $\Delta\nu = 2$ transition in the CF_3 torsion. An extra band at 548 cm^{-1} in the Raman spectrum of liquid CF_3OCl near −196 °C is assigned to a $CF_3OCl \cdots Cl_2$ complex. The values of the force constants $d(OX)$ for CF_3OX molecules are suggested to be near those for X_2O molecules. More than half the normal modes of A' symmetry show extensive mixing of symmetry coordinates. In some of these cases the symmetry coordinate for which the normal mode is named is the largest but not the dominant contributor to the potential energy distribution, while in others this symmetry coordinate is not even the largest contributor to the potential energy distribution. No normal modes of A' symmetry are present in which $\nu(CO)$, $\delta_s(CF_3)$, $\delta(COX)$, or $\rho(CF_3)$ symmetry coordinates are dominant, and the mode conventionally labeled as $\nu(CO)$ should be labeled as $\nu_s(CF_3)$. For the remaining A' normal modes and all the A'' normal modes, the symmetry coordinate for which the normal mode is named is dominant in the potential energy distribution.

INTRODUCTION

Trifluoromethyl hypofluorite, CF_3OF, is an important reagent in the synthesis of organic and inorganic fluorine compounds.[1] Trifluoromethyl hypochlorite, CF_3OCl, is the first member of the chloroxy perfluoroalkane series and molecules known to readily undergo free radical reactions form derivatives of CF_3OCl in which the CF_3O group is retained.[2] CF_3OF has been studied by IR and Raman spectroscopy,[3,4] electron diffraction[5] and microwave spectroscopy.[6] The preparation, identification and characterization of CF_3OCl included IR spectra only.[2,7] More recently, Raman spectra of both CF_3OF and CF_3OCl diluted in argon matrices at 8 K and of gaseous CF_3OF at ambient temperature have been reported.[8]

As a prelude to investigations of the structure of the CF_3OOX series (X = H, D, F, Cl) by vibrational spectroscopy,[9] electron diffraction[10] and microwave spectroscopy,[11] we reinvestigated the IR and Raman spectra of CF_3OF and CF_3OCl. While this work was in progress, the contribution by Smardzewski and Fox[8] appeared and complemented our results. Considerations about $\Delta\nu = 2$ transitions in the CF_3 rotor[12,13] analogous to the CH_3 rotor[14,15,16] have arisen and the final results are being reported separately.[17] Concurrently, our work with the CF_3OOX series has been completed[18] and is being reported separately.[19] The present paper summarizes our complete results[20] for the assignments and normal coordinate analysis of CF_3OF and CF_3OCl.

EXPERIMENTAL

CF_3OF and CF_3OCl were prepared at Kansas State University by the cesium fluoride catalyzed addition of F_2 and ClF, respectively, to COF_2.[21] Purification was normally by vacuum line distillation. CF_3OF was contaminated with $CF_2(OF)_2$ whose separation required low temperature gas chromatography.

Mid-IR spectra (4000–160 cm^{-1}) of the gases were recorded at Kansas State University with a Perkin-Elmer Model 180 IR spectrophotometer. Cells of 10 cm path length with AgCl windows and 15 cm path length with polyethylene windows were used in the regions 4000–400 cm^{-1} and 650–160 cm^{-1}, respectively.

Raman spectra of the liquids were recorded at Kansas State University in a low temperature cell similar in design to that of Brown *et al.*[22] with the coolant bath at −196 °C (liquid N_2) using a JASCO R-300 Laser Raman spectrophotometer. The 514.5 nm line of a Spectra Physics Model 164-00 argon ion laser was used with power levels at the laser in the range 100–300 mW. Depolarization ratios were determined by method IV of Claassen *et al.*[23] Their *f* has not been determined for the JASCO R-300; however, known depolarized bands gave depolarization ratios between 0.75 and 0.89.

---

† Present address: Department of Chemistry, Melbourne University, Parkville, Victoria 3052, Australia.
‡ Present address: IBM Corporation, Tucson, Arizona, USA.

CCC-0377-0486/80/0009-0230 $04.50

© Heyden & Son Ltd, 1980

Raman spectra of liquid CF_3OCl were also recorded at Allied Chemical Company using a Spex Ramalog system and low temperature cell and the 514.5 nm line of a Coherent Radiation argon ion laser.

SPECTRAL RESULTS

The IR and Raman spectra below 1400 cm^{-1} are shown in Figs 1 and 2, respectively. The frequencies are listed in Table 1 along with the complementary data of Smardzewski and Fox.[8] In general, our IR data for CF_3OF agree well with those of Wilt and Jones.[4] However, between 300 and 200 cm^{-1} our spectra show peaks 25–28 cm^{-1} higher in frequency but with similar band shapes. Since our IR and Raman data are self-consistent and in good agreement with the Raman data of Smardzewski and Fox for both CF_3OF and CF_3OCl, we conclude that the IR data of Wilt and Jones for CF_3OF below 300 cm^{-1} are in error for reasons unknown. Our IR data for CF_3OCl above 500 cm^{-1} are similar to the results of Schack and Maya[2] with our sample appearing to be of higher purity.

The assignments shown in Table 1 are those of Smardzewski and Fox[8] with the exception of one of the CF_3 rocking modes. We are in complete agreement with their reversal of the CO and OF stretching mode assignments of Wilt and Jones. Initially we had assumed, as do Smardzewski and Fox, that the two CF_3 rocking modes would lie between 200 and 300 cm^{-1}. However, our normal coordinate analysis places the two CF_3 rocking modes far apart with the one in the A'' symmetry block being in the surprisingly high frequency range of 400–500 cm^{-1}. The lowest frequency bands in the Raman spectra of both compounds initially seemed high to us for the CF_3 torsion and we suggested they might be $\Delta\nu = 2$ transitions[12,13] analogous to CH_3 torsions.[14-16] However, the microwave work of Buckley and Weber[6] strongly supports the assignments of $\Delta\nu = 1$ transitions being responsible for these bands. Vibrational satellite lines having 0.4 times the intensity of the ground state lines at 194 K in the microwave spectrum of gaseous CF_3OF[6] are in good agreement with a population ratio of 0.39 if the $\nu = 1$ state in the torsional mode is 127 cm^{-1} above the $\nu = 0$ state (using the gas phase Raman frequency of Smardzewski and Fox[8] of 127 cm^{-1} from Table 1 for the $0 \rightarrow 1$ transition in the CF_3 torsion).

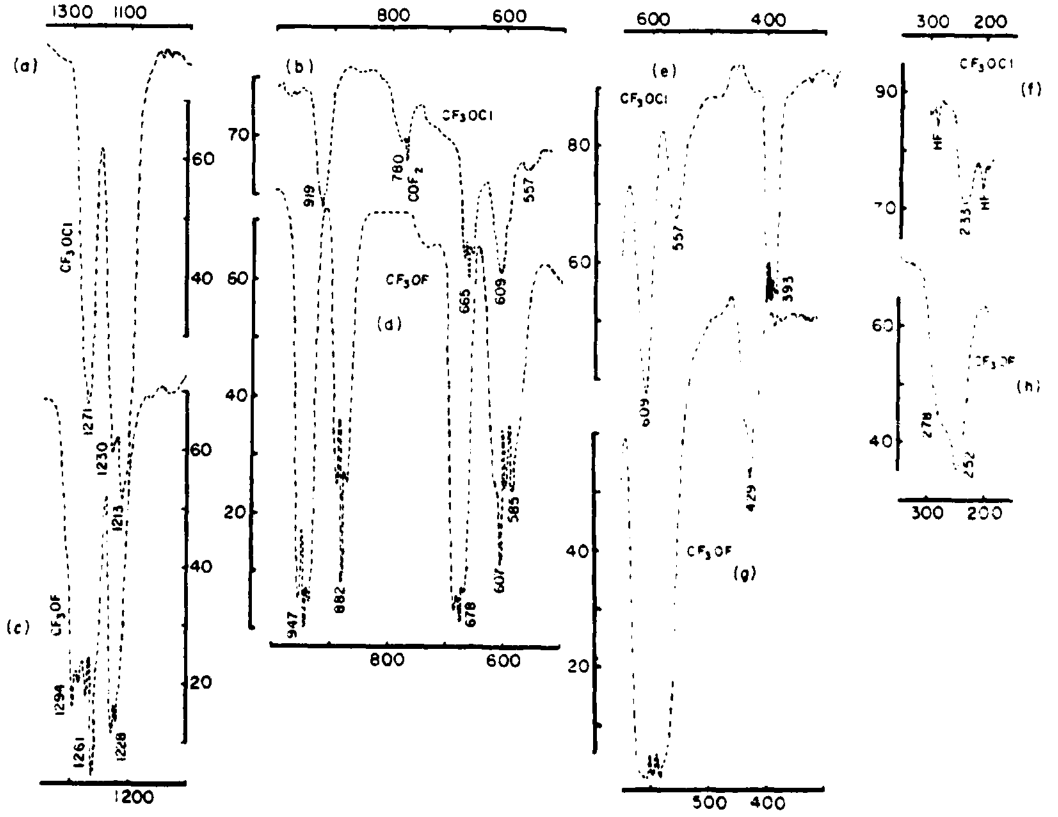

Figure 1. IR spectra (1400–160 cm^{-1}) of gaseous CF_3OF and CF_3OCl at ambient temperature. Spectra (a), (b), (e) and (f) are CF_3OCl and spectra (c), (d), (g) and (h) are CF_3OF. Spectra (a), (b), (c) and (d) are from a 10 cm cell with AgCl windows. Spectra (e), (f), (g) and (h) are from a 15 cm cell with polyethylene windows. Gas pressures are as follows: (a) 3 torr; (b) 65 torr; (c) 3 torr; (d) 161 torr; (e) 100 torr; (f) 140 torr; (g) 438 torr; (h) 438 torr. The mid-point of the doublet whose more intense component is labeled 1228 cm^{-1} in (c) is at 1222 cm^{-1} and the latter frequency is listed in Table 1. The band at 393 cm^{-1} in (e) has a contribution from the Q branch of the degenerate deformation of SiF_4 present as an impurity and in higher resolution expanded scale spectra the SiF_4 Q branch is clearly resolved.

© Heyden & Son Ltd, 1980

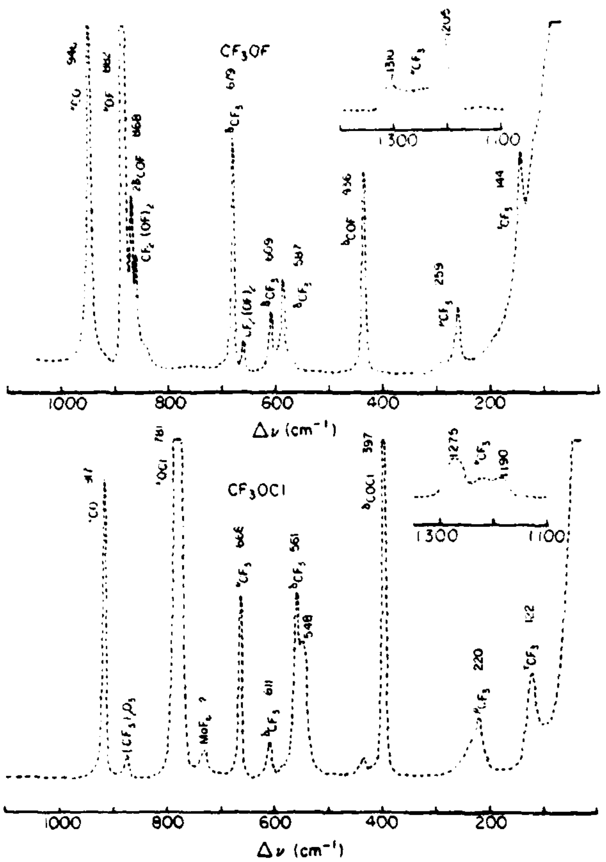

Figure 2. Raman spectra (below 1400 cm^{-1}) of liquid CF_3OF and CF_3OCl near −196 °C. The CF_3OF sample contains a small amount of $CF_2(OF)_2$. The CF_3OCl sample is believed to contain a small amount of Cl_2 held as a $CF_3OCl\cdots Cl_2$ complex.

If the band at 127 cm^{-1} were due to a $0\rightarrow 2$ transition, then the $0\rightarrow 1$ transition would be 65 cm^{-1} giving a population ratio of 0.62 at 194 K. Consequently, the two overlapping bands between 200 and 300 cm^{-1} may be interpreted as the CF_3 rock in the A' symmetry block and $2\tau(CF_3)A'$ (i.e. a $\Delta\nu = 2$ transition in the CF_3 torsion). A detailed investigation of the Raman spectrum of gaseous CF_3OF under higher resolution confirms this suggestion and is being reported separately.[17]

When the IR band of gaseous CF_3OF with a Q branch at 429 cm^{-1} in Fig. 1 is recorded with abscissa expansion and higher resolution a shoulder at 431 cm^{-1} is seen on the Q branch. The corresponding liquid Raman band at 436 cm^{-1} is polarized and so belongs in the A' symmetry block; however, the presence of a weak depolarized band a few cm^{-1} away can neither be confirmed nor denied by the appearance of the Raman spectrum of the liquid. The Raman spectra of Smardzewski and Fox[8,24] for CF_3OF in an argon matrix show a single band at 433 cm^{-1} whose width is comparable to that of other bands in the argon matrix. In our opinion their Raman spectra can neither confirm nor deny the possible presence of two fundamentals separated by several cm^{-1}. Initially we had not tried to interpret the shoulder at 431 cm^{-1}. However, we now adopt the suggestion of our normal coordinate analysis and assign 431 cm^{-1} as the CF_3 rocking mode in the A'' symmetry block.

Our Raman data for liquid CF_3OCl show a very weak band at 430 cm^{-1} in every spectrum where the sensitivity is high enough to record the 611 cm^{-1} band which is the weakest Raman band previously assigned to a fundamental. Since the IR baseline is not flat in this region due to problems with exact compensation of polyethylene sheets placed in the reference beam, it is difficult to tell whether or not a very weak IR band may be present at 430 cm^{-1}. Here, also, we now adopt the suggestion of our normal coordinate analysis and assign 430 cm^{-1} as the CF_3 rocking mode in the A'' symmetry block.

Initially our sample of CF_3OCl contained a large amount of chlorine, and the band in CF_3OCl listed at 561 cm^{-1} in Table 1 for the Raman spectrum of the liquid was only visible as a small shoulder on the intense band due to the dissolved chlorine. Purification of the CF_3OCl sample gave the Raman spectrum shown in Fig. 2. The band at 548 cm^{-1} in Fig. 2 does not appear in the IR spectrum of gaseous CF_3OCl. Smardzewski and Fox[8,24] observe extra bands in the Raman spectrum of CF_3OCl in an argon matrix at 547 and 539 cm^{-1} with relative intensities of 9 and 10 respectively. Our band at 548 cm^{-1} in the Raman spectrum of liquid CF_3OCl appears upon abscissa expansion and higher resolution to consistent of two overlapping bands of equal intensity at about 551 and 545 cm^{-1}. Since all the CF_3OCl fundamentals are reasonably accounted for, the band(s) at 548 cm^{-1} must be either a non-fundamental of CF_3OCl or an impurity.

The assignment to a difference band is reasonable on a frequency basis but not on the basis of intensity and polarization. Using liquid Raman frequencies, $\delta_s(CF_3)A' - \tau(CF_3)A'' = 666 - 122 = 544$ cm^{-1} in good agreement with 548 cm^{-1}. However, the transition from ($\nu_{12} = 1$ all other $\nu_i = 0$, an A'' state) to ($\nu_5 = 1$, all other $\nu_i = 0$, an A' state) is a non-totally symmetric transition and should be depolarized. The 548 cm^{-1} band is polarized. The population of ($\nu_{12} = 1$, all other $\nu_i = 0$) is 10–17% of that of (all $\nu_i = 0$) for $\nu_{12} = \tau(CF_3)A'' =$ 122 cm^{-1} between 77 and 100 K (estimated range of sample temperature with liquid N_2 in the coolant bath of the low temperature cell). The fact that the 548 cm^{-1} band has 80% of the intensity of the $\delta_{as}(CF_3)A'$ fundamental at 561 cm^{-1} is difficult to explain for a non-fundamental with no apparent Fermi resonance possibilities and such an unfavorable Boltzmann population ratio. On both the intensity and polarization basis we feel that the 548 cm^{-1} band must be due to a species other than CF_3OCl.

Possible impurities in the ClF used to prepare CF_3OCl by addition to COF_2 are ClF_5 and ClF_3. However, the Raman spectra of liquid ClF_5[25] and liquid ClF_3[26] are such that both compounds would be detected by intense bands well separated from any of the CF_3OCl bands in Fig. 2.

For the case of CF_3OF prepared by the addition of F_2 to COF_2, CO_2 impurity in the COF_2 leads to the production of some $CF_2(OF)_2$. By analogy the addition of ClF to CO_2 might lead to a variety of materials of the general formula $CF_wCl_x(OF)_y(OCl)_z$. Here w, x, y, z may have values 0, 1 or 2 in various combinations subject to the restrictions that $(w + x) = 2$ and $(y + z) = 2$. For compounds with C—Cl bonds ($x \neq 0$) and for compounds with O—F bonds ($y \neq 0$), Raman bands

© Heyden & Son Ltd, 1980

Table 1. IR and Raman data[a,b] below 1400 cm^{-1} and assignment of fundamentals for CF$_3$OF and CF$_3$OCl

CF$_3$OF								CF$_3$OCl							
IR[c] gas		Raman gas[d]	Raman liquid			Ar matrix[d]		IR[c] gas		Raman liquid			Ar matrix[d]		Assignment[e]
1294	vs	1300	1310	1	?	1288	5	1271	vs	1275	3	0.60	1269	17	$\nu_{as}(CF_3)A'$
		↓ w, br													
1261	vs	1250				1250	7	1230	vs				1221	8	$\nu_{as}(CF_3)A''$
1222	vs	1219 w	1205	3	0.45	1211	14	1213	vs	1190	2	0.66	1200	3	$\nu_s(CF_3)A$
947 *Q*	s	945 m	946	16	0.49	945	54	919 *Q*	m	917	26	0.46	920	28	$\nu(CO)A$
882 *Q*	m	881 vs	882	100	0.03	883	100	780	w	781	100	0.12	783	100	$\nu(OX)A$
		864 vw	868	8	0.04	871	7								$2\delta(COF)A'$
													776	24	$\nu(O^{37}Cl)A'$
678 *Q*	s	675 w	679	12	0.35	678	24	665 *Q*	m	666	15	0.38	663	30	$\delta_s(CF_3)A$
607	m	606 w, sh	609	3	0.85	606	9	609	m	611	3	0.76	609	15	$\delta_{as}(CF_3)A''$
585	m	581 w	587	5	0.43	582	9	557	w	561	14	0.26	558	28	$\delta_{as}(CF_3)A'$
										548	12		547	9	$CF_3OCl \cdot Cl_2$
													539	10	
431 sh	vw									430	1	?			$\rho(CF_3)A''$
429 *Q*	vw	429 m	436	10	0.32	433	34	393 Q	m	397	41	0.27	398	62	$\delta(COX)A'$
278	vw	272 w	259	3	0.52	256	16	233	vw	220	4	0.47	239	5	$\rho(CF_3)A$
252	vw	246 w	285 sh?	?	?			220 sh??		~235 sh?	?	?			$2\tau(CF_3)A'$
		127 w, br	144	5	0.86					122	6	0.81			$\tau(CF_3)A''$

[a] All observed frequencies are in cm^{-1}. Abbreviations used are: w, weak; m, medium; s, strong; vw, very weak; vs, very strong; sh, shoulder; br, broad.

[b] Raman data are listed as frequency in cm^{-1} first and relative intensity second. For all spectra but those of gases, relative intensity is on a scale where the most intense band is 100. For the spectra of liquids the third entry is depolarization ratio measured by method IV of Claassen *et al.*[23] These numbers are really R rather than ρ_s in the notation of Table 1 of Claassen *et al.* since f has not been measured on the JASCO R-300. Known depolarized bands gave R values in the range 0.75 to 0.89 on the JASCO R-300 between 200 cm^{-1} and 3000 cm^{-1} Raman shift from the 514.5 nm argon ion laser line.

[c] *The notation* Q *designates the* Q *branch frequency for bands having* PQR structure as follows: CF$_3$OF 938, 947, 956; 874, 882, 890; 670, 678, 688; ~420, 429, 439. CF$_3$OCl 915, 919, 923; 659, 665, 671; 386, 393, 399.

[d] Data is from Smardzewski and Fox.[8,24]

[e] The word descriptions for these symbols shown in Table 3 are used to name the normal modes. These normal mode names may be classified as reasonable or misleading by inspection of the potential energy distribution in Table 5 using the following criterion: the appropriate symmetry coordinate makes by far the largest contribution to the potential energy distribution. By that criterion, all four modes in the A'' block but less than half the modes in the A' block have reasonable names.[45–48] Based on the potential energy distributions in Table 5, the following tabulation provides complicated but reasonable symbols for the A' modes in question next to the numbers and symbols from Table 3.

Table 3	CF$_3$OF	CF$_3$OCl
1 $\nu_{as}(CF_3)A'$		
2 $\nu_s(CF_3)A'$	$\nu(CO)A' + \delta_s(CF_3)A' + \nu_s(CF_3)A'$	$\nu(CO)A' + \delta_s(CF_3)A' + \nu_s(CF_3)A'$
3 $\nu(CO)A'$	$\nu_s(CF_3)A'$	$\nu_s(CF_3)A'$
4 $\nu(OX)A'$		$\nu(OCl)A' + \delta(COCl)A' + \rho(CF_3)A'$
5 $\delta_s(CF_3)A'$	$\delta_s(CF_3)A' + \delta(COF)A' + \nu(OF)A' + \nu(CO)A'$	$\delta_s(CF_3)A' + \nu(CO)A' + \nu(OCl)A' + \delta(COCl)A'$
6 $\delta_{as}(CF_3)A'$		
7 $\delta(COX)A'$	$\rho(CF_3)A' + \delta_{as}(CF_3)A' + \delta(COF)A'$	$\rho(CF_3)A' + \nu(OCl)A' + \delta_{as}(CF_3)A'$
8 $\rho(CF_3)A'$	$\rho(CF_3)A' + \delta(COF)A'$	$\delta(COCl)A' + \rho(CF_3)A'$
9 $\nu_{as}(CF_3)A''$		
10 $\delta_{as}(CF_3)A''$		
11 $\rho(CF_3)A''$		
12 $\tau(CF_3)A''$		

should be present that are well separated from any of the CF$_3$OCl bands in Fig. 2. One that might be less easily detected is CF$_2$(OCl)$_2$. It is possible to estimate the frequencies for CF$_2$(OCl)$_2$ from those of CF$_3$OCl by using differences between CF$_3$OF and CF$_2$(OF)$_2$ frequencies. These estimates suggest that CF$_2$(OCl)$_2$ might have a strong band at 548 cm^{-1} but not no traces of other bands in addition to those in Fig. 2.

An additional possibility is further reaction of CF$_3$OCl to form CF$_3$OClF$_2$. The CF$_3$O fragments of both CF$_3$OCl and CF$_3$OClF$_2$ might have indistinguishable spectra and differentiation would depend on vibrations of the ClF$_2$ fragment. Since ClF$_3$ has a ClF stretching mode at 529 cm^{-1} (gas phase with liquid at lower frequency), the ClF$_2$ fragment of CF$_3$OClF$_2$ could be responsible for the 548 cm^{-1} band. However, it is difficult to believe that the remaining modes of the ClF$_2$ fragment would not produce additional bands in Fig. 2.

We attribute the 548 cm^{-1} band to the stretching of the Cl—Cl bond of a complex of CF$_3$OCl with molecular chlorine. Chlorine dissolved in CF$_3$OCl would be expected to give three bands for ^{35}Cl$_2$, ^{35}Cl^{37}Cl and ^{37}Cl$_2$ near 545 cm^{-1}. Liquid chlorine in our low temperature cell with liquid nitrogen in the bath gave bands at 547, 540 and 533 cm^{-1} in the intensity ratio 6.5:4.5:1 (theoretical 9:6:1). Condensation of chlorine into a CF$_3$OCl sample of purity similar to Fig. 2 gave bands at 552 and 544 cm^{-1} and a possible shoulder at 537 cm^{-1}. The 548 cm^{-1} band in CF$_3$OCl does not appear to be due to chlorine in the same environment as pure liquid

© Heyden & Son Ltd, 1980

Table 2. The possible arrangements of chlorine isotopes

No.	Mass arrangement CF_3OCl	Cl—Cl		Relative abundance
1	35	35	35	27
2	35	35	37	9
3	35	37	35	9
4	35	37	37	3
5	37	35	35	9
6	37	35	37	3
7	37	37	35	3
8	37	37	37	1

chlorine or excess chlorine in CF_3OCl. However, it would be possible for CF_3OCl to form a complex with chlorine of sufficient strength that is not possible to remove all the chlorine from CF_3OCl by our purification procedure. Then the 548 cm^{-1} band could be due to the stretching of the Cl—Cl bond in a $CF_3OCl\cdots Cl—Cl$ complex.

A complex via the chlorine atom of CF_3OCl, analogous to X_3^- halide complex ions such as I_3^-, would have eight possible isotopic chlorine modifications. The eight possible arrangements of chlorine isotopes and their relative abundances are as shown in Table 2.

The effect of the mass of the chlorine atom in CF_3OCl on the frequency for stretching the Cl—Cl bond from Cl_2 in the complex depends on the strength of the complex. The limit for a weak complex could be three bands due to three degenerate sets as follows: 1 and 5 of relative intensity 36; 2, 3, 6 and 7 of relative intensity 24; and 4 and 8 of relative intensity 4. As complex strength increases these degeneracies would be broken as the mass of the chlorine atom in CF_3OCl begins to influence the frequency. A reasonable strong complex extreme would be where the vibration is still best treated as a perturbed diatomic molecules stretching rather than a three body problem with antisymmetric and symmetric skeletal stretching and skeletal bending. However, the degeneracies are broken and the eight frequencies might tend to group into the following four bands: 1 of relative intensity 27; 2, 3 and 5 of relative intensity 27; 4, 6 and 7 of relative intensity 9; and 8 of relative intensity 1.

For the weak complex extreme, the third band probably would not be observed as it is too weak, so a higher frequency band 1.5 times as intense as a lower frequency band is to be expected. For the strong complex extreme the fourth band would definitely be too weak to observe and the extent of overlap of the other three bands is uncertain. A likely result would be that the third band of intensity 9 would overlap the second band of intensity 27 to give a single asymmetric band or a band with a low frequency shoulder. This superposition would result in a lower frequency band with relative intensity 27 (or more from overlap of the third band) and a higher frequency band of relative intensity 27 (from complex 1). Then two resolvable bands seem reasonable for the range of complex strengths suggested. The higher frequency band would be expected to be from 1.5 times as intense to slightly less intense than the lower frequency band depending on the strength of the complex.

Thus, superposition of spectra of these eight complexes for plausible strengths of the complex could provide two resolvable bands with the higher frequency band being from 1.5 times as intense to slightly less intense than the lower frequency band. Formation of a $CF_3OCl\cdots Cl—Cl$ complex could account for a band at 548 cm^{-1} in the Raman spectrum of liquid CF_3OCl appearing to consist of two overlapping bands of about equal intensity at 551 and 545 cm^{-1}. The observation by Smardzewski and Fox[8] of bands at 547 and 539 cm^{-1} of relative intensities 9 and 10, respectively, in the Raman spectrum of CF_3OCl in an Ar matrix is also consistent. Although the CF_3OCl in Ar sample is intended to contain isolated molecules, experience in other systems suggests that the Ar : CF_3OCl ratio of 100 is too low to insure isolated molecules since ratios $>10^4$ may be necessary in some cases to ensure really isolated molecules. The conditions of a liquid near 77 K and an Ar matrix at 8 K should favor complex formation[27] and the improved resolution in the Ar matrix is reasonable. Thus, a $CF_3OCl\cdots Cl—Cl$ complex provides a simple explanation and is proposed as the most likely origin of the 548 cm^{-1} band.

NORMAL COORDINATE ANALYSIS

The Wilson FG-matrix method[28] was used with the computer programs written by Schachtschneider.[29] The G matrices were calculated from the electron diffraction structure for CF_3OF[5,30] and reasonable assumptions for the structure of CF_3OCl.[30] Symmetrization was accomplished using the symmetry coordinates listed in Table 3 generated from the internal coordinates in Fig. 3.

Table 3. Symmetry coordinates for CF_3OX molecules of C_s symmetry

A′ symmetry	
Antisymmetric CF_3 stretch, $\nu_{as}(CF_3)A'$	$S_1 = \sqrt{6}^{-1}(2\Delta r_4 - \Delta r_5 - \Delta r_6)$
Symmetric CF_3 stretch, $\nu_s(CF_3)A'$	$S_2 = \sqrt{3}^{-1}(\Delta r_4 + \Delta r_5 + \Delta r_6)$
CO stretch $\nu(CO)A'$,	$S_3 = \Delta 1$
OX stretch $\nu(OX)A'$,	$S_4 = \Delta d$
Symmetric CF_3 deformation, $\delta_s(CF_3)A'$	$S_5 = \sqrt{6}^{-1}(\Delta\alpha_4 + \Delta\alpha_5 + \Delta\alpha_6 - \Delta\beta_4 - \Delta\beta_5 - \Delta\beta_6)$
Antisymmetric CF_3 deformation, $\delta_{as}(CF_3)A'$	$S_6 = \sqrt{6}^{-1}(2\Delta\alpha_4 - \Delta\alpha_5 - \Delta\alpha_6)$
COX bend, $\delta(COX)A'$	$S_7 = \Delta\gamma$
CF_3 rock, $\rho(CF_3)A'$	$S_8 = \sqrt{6}^{-1}(2\Delta\beta_4 - \Delta\beta_5 - \Delta\beta_6)$
Redundant	$S_0^a = \sqrt{6}^{-1}(\Delta\alpha_4 + \Delta\alpha_5 + \Delta\alpha_6 + \Delta\beta_4 + \Delta\beta_5 + \Delta\beta_6)$
A″ symmetry	
Antisymmetric CF_3 stretch, $\nu_{as}(CF_3)A''$	$S_9 = \sqrt{2}^{-1}(\Delta r_5 - \Delta r_6)$
Antisymmetric CF_3 deformation, $\delta_{as}(CF_3)A'$	$S_{10} = \sqrt{2}^{-1}(\Delta\alpha_5 - \Delta\alpha_6)$
CF_3 rock, $\rho(CF_3)A''$	$S_{11} = \sqrt{2}^{-1}(\Delta\beta_5 - \Delta\beta_6)$
CF_3 torsion, $\tau(CF_3)A''$	$S_{12} = \Delta\tau$

[a] These coordinates are correct for tetrahedral C_{3v} angles. However, they may be used for the non-tetrahedral angle case since the redundancy is removed during the diagonalization of the G matrix.

© Heyden & Son Ltd. 1980

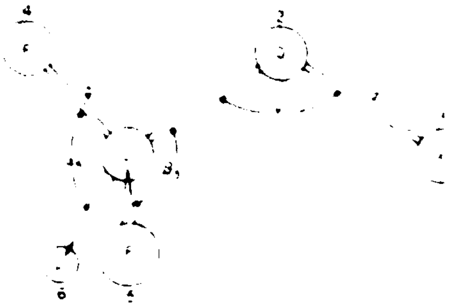

Figure 3 Internal coordinates for CF_3OX molecules. C_s symmetry is assumed with F, C, O and X atoms in the same plane.

The simple molecules F_2O,[12] Cl_2O,[11] CF_3H[14] and CF_4[15] were used to establish a reasonable range of force constant values for CF_3OF and CF_3OCl. Force constant values within this range that were consistent with bond strengths of CF_3OF and CF_3OCl implied by their chemical reactions are shown in Table 4 where force constants based on internal coordinates are listed. The internal coordinate F matrix follows from the list of force constants in Table 4.[16] The potential energy distributions using symmetry force constants based on the symmetry coordinates in Table 3 and the internal coordinate force constant values in Table 4 are in Table 5 along with a comparison of calculated and observed frequencies.

Improvement of the frequency fit for CF_3OCl to that for CF_3OF requires a higher OCl stretching constant, $d(OCl)$, near the value for $d(OF)$ in CF_3OF or alteration of some off diagonal force constants. The force constant values in Table 4 are consistent with the chemical behavior of CF_3OF and CF_3OCl and the force constant values in the following molecules related to CF_3OF and CF_3OCl, respectively: HOF,[17] F_2O[12] and ClO_3OF,[18] and HOCl,[17] Cl_2O,[11] ClO_3OCl[18] and ClO_3OClO_3.[18] The available data favors values of $d(OX)$ in these CF_3OX compounds close to those of the corresponding X_2O compounds.

CF_3OF is thermally stable in an IR cell at room temperature and the gas phase Raman spectrum can be obtained at room temperature using Ar^+ laser radiation. CF_3OCl is stable at room temperature only under scrupulously dry, inert conditions. Photolytic decomposition of CF_3OCl is quite rapid and the decomposition products are consistent with a two step reaction path involving the two radicals CF_3 and Cl.[2] In our work CF_3OCl began to decompose during the recording of its IR spectrum at ambient temperature. Smardzewski and Fox[8] report that CF_3OCl photolyzed almost immediately during their attempt to record its gas phase Raman spectrum at room temperature using Ar^+ laser radiation. Since this behavior suggests that the OF bond in CF_3OF is stronger than the OCl bond in CF_3OCl, similar values of $d(OF)$ and $d(OCl)$ are considered unlikely.

Values of $d(OF)$ in mdyn $Å^{-1}$ are 4.27, 3.95 and 3.56 for HOF,[17] F_2O[12] and ClO_3OF,[18] respectively. Noble and Pimentel[40] have suggested that $d(OF)$ is larger in HOF than in F_2O because the electronegativity of the F atom weakens the OH bond and strengthens the OF bond by attraction of electron density out of the OH bond into the OF bond. For such a change competition it seems reasonable that the CF_3 group of electronegativity 3.3 to 3.4[41] would be better able to compete with the F atom for electron density over the CF_3OF frame than the H atom would with the F atom over the HOF frame. Thus, an upper limit for $d(OF)$ in CF_3OF might be expected to be smaller than in HOF and near to F_2O. The $d(OF)$ value of 3.56 in ClO_3OF where the ClO_3 group has an electronegativity of 3.25 to 3.4[41] represents a reasonable lower limit. The value $d(OF)$ = 3.85 in Table 4 is near the middle of the range from 3.56 to about 4.00 and close to the value for F_2O.

Values of $d(OCl)$ in mdyn $Å^{-1}$ are 3.68, 2.78, 2.65 and 3.09 for HOCl,[17] Cl_2O,[11] ClO_3OCl[18] and ClO_3OClO_3,[18] respectively. The electronegativity argument of Noble and Pimentel can be applied to HOCl, Cl_2O and CF_3OCl. Then, $d(OCl)$ in CF_3OCl should be lower than in HOCl but now the CF_3 group is more electronegative than the Cl atom (3.3–3.4 compared to 3.0), rather than being less electronegative than the F atom in CF_3OF. The $d(OCl)$ value of 2.65 in ClO_3OCl, where the ClO_3 group has an electronegativity of 3.25 to 3.4, represents a reasonable lower limit. The $d(OCl)$ values of 3.09 in ClO_3OClO_3 as a normal ClO single bond gives a reasonable upper limit. The value $d(OCl)$ = 2.80 in Table 4 is near the middle of the range from 2.65 to 3.09 and close to the value for Cl_2O.

Table 4. Internal coordinate force constants[a,b] for CF_3OF and CF_3OCl

Force constant	CF_3OF	CF_3OCl
r	6.950	6.950
t	5.200	5.200
d	3.850	2.800
α	2.000	2.050
β	1.200	1.150
γ	1.800	1.700
τ	0.0167	0.0161
rr	0.900	0.900
rt	0.850	0.900
td	1.000	0.300
$r\alpha$(opp.)	0.120	0.120
$r\alpha$(adj.)	0.910	0.910
$r\beta$(adj.)	0.750	0.700
$t\beta$(opp.)	0.100	0.100
[illegible]	0.200	0.200
[illegible]	0.600	0.600
[illegible]	0.000	0.100
$d\gamma$	0.250	0.100
$\alpha\alpha$	0.300	0.350
$\alpha\beta$(opp.)	0.000	0.000
$\alpha\beta$(adj.)	0.150	0.150
$\beta\beta$	0.100	0.100

[a] Stretching constants in units of millidynes per angstrom. Stretch-bend interaction constants in units of millidynes per radian. Bending and torsion constants in units of millidyne angstrom per square radian.

[b] See Fig. 3 for definition of these internal coordinates.

[c] For torsions [illegible] kcal mol⁻¹ rad⁻² = 287.9 [illegible] millidyne Å rad⁻² molecule⁻¹. For the CF_3 torsion n = 3 but the GMAT program[20] has already taken into account n = 3 so n = 1 must be used on the right hand side of the equation to give [illegible] 287.9. For a program not taking n = 3 into account the proper value would be a factor of 9 (n^2 for n = 3) greater than the one in this table. See Ref. 17 and Ref. 18 Appendix B for further discussion.

Table 5. Potential energy distribution[a] for CF_3OX (X = F, Cl) and comparison of calculated and observed frequencies[b]

A' symmetry

	1		2		3		4		5		6		7		8	
X	F	Cl	F	Cl	F	Cl	F	Cl	F	Cl	F	Cl	F	Cl	F	Cl
ν_i calc (cm^{-1})	1321	1309	1214	1208	941	935	883	774	674	658	589	571	420	348	267	217
ν_i obs (cm^{-1})	1294	1271	1222	1213	947	919	882	780	678	665	585	557	429	393	278	233
i F_{ii}																
1 $r - rr$	76	89	17	5	5				6							
2 $r + 2rr$			38	41	60	65			6	5						
3 l	12	5	54	67	8	16	18		11	15			5		6	
4 d					7		76	51	12	9		8	8	30		
5 *	5		38	46			5		36	48	12	5	10	6		
6 $\alpha - \alpha\alpha$	16	18									61	73	24	12		
7 γ	11	9			8		5	22	17	8			21	9	38	50
8 $\beta - \beta\beta$	10	10					7	14					29	38	58	44

$^{*} = (\alpha + \beta)/2 + \alpha\alpha + \beta\beta - \alpha\beta - 2\alpha\beta$

A'' symmetry

	9		10		11		12	
X	F	Cl	F	Cl	F	Cl	F	Cl
ν_i calc (cm^{-1})	1256	1262	616	613	429	422	128	108
ν_i obs (cm^{-1})	1261	1230	607	609	431	430	127	108
i F_{ii}								
9 $r - rr$	105	104	8	8				
10 $\alpha - \alpha\alpha$	20	20	55	57	31	30		
11 $\beta - \beta\beta$	12	11	15	13	76	77		5
12 τ							96	96

[a] The numbers in the table give the contributions to the potential energy of the various diagonal elements of the symmetrized F matrix ($100\, L_{ik}^2 F_{kk}/\lambda_i$). Numbering of the symmetrized force constants, F_{ii}, and the normal mode frequencies, ν_i, are identical to the numbering of the symmetry coordinates in Table 3. The expression for each symmetrized force constant, F_{ii}, in terms of the force constants in Table 4 is included in the table. Contributions of less than 5% are not included in the table. The sum of the entries in each column will be 100 when positive contributions from diagonal elements of less than 5% and both positive and *negative contributions from off diagonal elements* are included.

[b] The frequencies for CF_3OF are from gas phase IR spectra (Table 1) except for the CF_3 torsion which is from the gas phase Raman spectra of Smardzewski and Fox.[8,24] The frequencies for CF_3OCl are from gas phase IR spectra (Table 1) with two exceptions: 430 cm^{-1} from the Raman spectrum of the liquid and 108 cm^{-1} estimated as the Raman frequency of the liquid less 12% which is the percentage decrease from the liquid frequency to the gas frequency for the CF_3 *torsion in* CF_3OF.

The potential energy distributions in Table 5 show that extensive mixing of the symmetry coordinates in Table 3 occurs in some of the normal modes[43] as might be expected for molecules with atoms of similar masses. Potential energy distributions based on internal coordinates and the corresponding force constants in Table 4 are available elsewhere.[44] Using either potential energy distribution, five modes, all in the A' block under C_s symmetry, differ somewhat between CF_3OF and CF_3OCl; they are $\nu_s(CF_3)A'$, $\nu(OX)A'$, $\delta_s(CF_3)A'$, $\delta(COX)A'$, $\rho(CF_3)A'$. The normal mode symbols used in Table 1, based on the symbols of the symmetry coordinates in Table 3, may be classified as reasonable or misleading depending upon whether or not the following criterion is met: the appropriate symmetry coordinate makes the dominant contribution[45] to the potential energy distribution. By that criterion, all four modes in the A'' block but less than half the modes in the A' block have reasonable symbols in Table 1.[46] The normal modes whose symbols in Table 1 are misleading are in two categories: those where the symmetry coordinate for which the mode is named makes the largest but not the dominant contribution[47] and those where another symmetry coordinate makes the largest contribution.[48] Inspection of Table 5 suggests several changes[47] for the normal mode symbols in Table 1, with the result that the simple symbols $\nu(CO)A'$, $\delta_s(CF_3)A'$, $\delta(COX)A'$ and $\rho(CF_3)A'$ will no longer occur in the A' block, and the mode conventionally labeled as $\nu(CO)A'$ becomes $\nu_s(CF_3)A'$.

The acceptance of the view stated previously that values of $d(OX)$ in CF_3OX compounds are close to $d(OX)$ in the corresponding X_2O compounds supports the acceptance of the force constant values in Table 4 and the potential energy distribution in Table 5 as reasonable. Although a normal coordinate analysis should not normally be said to confirm an assignment absolutely, the results are useful for suggesting alternatives and reasonable conclusions from contradictory data. Here the result that a CF_3 rocking frequency of A' symmetry should be above 400 cm^{-1} led to the recognition that one of two bands between 200 and 300 cm^{-1} could be $2\tau(CF_3)A'$ and prompted our detailed investigation of the CF_3 torsion.[7] The reversal of the CO stretching and OF stretching assignment of Wilt and Jones for CF_3OF by Smardzewski and Fox[8] is supported, although the name CO stretching is misleading.[48,49] For CF_3 compounds of C_s symmetry the assignment of one of the bands in the 1150–1350 cm^{-1} region to the antisymmetric CF_3 stretch of A' symmetry is often

© Heyden & Son Ltd, 1980

ambiguous. Our results here for CF_3OX compounds and elsewhere for the CF_3OOX series[18] suggest that the intermediate frequency of the three bands between 1150 and 1350 cm^{-1} belongs in the A'' block.

SUMMARY

1. The reassignment of $\nu(OF)A'$ in CF_3OF by Smardzewski and Fox is consistent with our normal coordinate analysis.
2. For both CF_3OF and CF_3OCl, $\rho(CF_3)A''$ is assigned near 430 cm^{-1} and the two bands between 200 cm^{-1} and 300 cm^{-1} are assigned to a fundamental involving both $\rho(COX)A'$ and $\delta(COX)A'$ and to a $\Delta\nu = 2$ transition in $\tau(CF_3)A''$.
3. An extra band at 548 cm^{-1} in the Raman spectrum of liquid CF_3OCl is assigned to a $CF_3OCl\cdots Cl_2$ complex.
4. The force constants $d(OX)$ for CF_3OX molecules are suggested to be near in value to $d(OX)$ for X_2O molecules.
5. More than half the normal modes of A' symmetry show extensive mixing of symmetry coordinates.
6. For some normal modes of A' symmetry, the symmetry coordinate for which the normal mode is named is the largest but not the dominant contributor to the potential energy distribution.[47]
7. For other normal modes of A' symmetry, the symmetry coordinate for which the mode is named is not even the largest contributor to the potential energy distribution.[48]
8. No normal modes of A' symmetry are present in which $\nu(CO)A'$, $\delta_s(CF_3)A'$, $\delta(COX)A'$, or $\rho(CF_3)A'$ symmetry coordinates are dominant.
9. The normal mode conventionally labeled as $\nu(CO)A'$ should be labeled as $\nu_s(CF_3)A'$.
10. For the remaining A' normal modes and all the A'' normal modes, the symmetry coordinate for which the normal mode is named is dominant in the potential energy distribution.

NOTES AND REFERENCES

1 C J Hoffman, *Chem Rev* **64**, 91 (1964)
2 C J Schack and W Maya, *J Am. Chem Soc* **91**, 2902 (1969)
3. R T Lagemann, E A Jones and P J H Woltz *J Chem. Phys* **20**, 1768 (1952).
4 P M Wilt and E A Jones, *J Inorg Nucl Chem* **30**, 2933 (1968)
5 F P Diodati and L S Bartell, *J Mol Struct.* **8**, 395 (1971).
6 P Buckley and J P Weber, *Can. J. Chem* **52**, 942 (1974)
7 D E Gould L R Anderson, D E Young and W B Fox, *J Chem Soc Chem Commun.* 1564 (1968)
8 R R Smardzewski and W B. Fox, *J Fluorine Chem.* **6** 417 (1975)
9 D D DesMarteau and R. M Hammaker, unpublished studies.
10. C J Marsden, D D DesMarteau and L S. Bartell, *Inorg. Chem* **16**, 2359 (1977)
11. D D DesMarteau, Y S. Li and J. R Durig, *Inorg. Chem* (in press).
12 R M. Hammaker and D D DesMarteau, Raman Newsl No 80 (7 August 1975).
13. R. M Hammaker and D D DesMarteau, Paper 451, Pittsburgh Conference on Analytical Chemistry and Applied Spectroscopy, Cleveland Ohio, USA (1976)
14 J R Durig, W. E Bucy, L A. Carreira and C. J Wurrey, *J Chem Phys* **60**, 1754 (1974)
15 J R Durig, W E Bucy and C J Wurrey, *J. Chem Phys.* **60**, 3293 (1974)
16 J. R Durig, W. E. Bucy, C J. Wurrey and L A. Carreira, *J Phys. Chem* **79**, 988 (1975)
17 R M Hammaker, W G Fateley, Ajit S Manocha D D DesMarteau, B. J Streusand and J R Durig, *J. Raman Spectrosc* **9**, 181 (1980).
18 Ajit S Manocha, MS Thesis, Kansas State University, Manhattan, KS USA (1978).
19. A S. Manocha, D D DesMarteau, R. M. Hammaker and C J. Marsden, in preparation.
20 Jeng-chung Kuo, MS Thesis, Kansas State University, Manhattan, KS, USA (1978).
21 M Lustig, A R. Pitochelli and J K. Ruff, *J Am Chem Soc* **89**, 2841 (1967)
22 C W Brown, A. G Hopkins and F P Daly, *Appl. Spectrosc.* **28**, 194 (1974).
23 H H. Claassen, H Selig and J. Shamir, *Appl Spectrosc* **23**, 8 (1969)
24 R R. Smardzewski and W B Fox, U S Naval Research Laboratory, Washington DC 20375, USA, private communication to D D DesMarteau
25 G M Begun, W. H Fletcher and D F Smith, *J Chem. Phys* **42**, 2236 (1965)
26 H. Selig, H H Claassen and J H Holloway *J Chem Phys.* **52**, 3517 (1970)
27 Since low temperature should favor complex formation, the complex is probably not present in the gaseous CF_3OCl at room temperature. Even if the complex were present in the gas it would probably be too weak to cause the IR inactive stretching of gaseous Cl_2 to become observable in the IR spectrum of the gaseous complex. Thus, the absence of a 548 cm^{-1} band in the IR spectrum of gaseous CF_3OCl at room temperature is consistent with the presence of a weak $CF_3OCl\cdots Cl-Cl$ complex at low temperature
28. E B Wilson J., J. C. Decius and P C Cross, *Molecular Vibrations*. McGraw-Hill, New York (1955)
29. J H. Schachtschneider, *Vibrational Analysis of Polyatomic Molecules V and VI*, Tech. Rept. Nos 231–64 and 57–65, respectively. Shell Development Co., Houston, Texas
30. *For CF_3OX the structural parameters are the* CF, CO *and* OX bond lengths and the five angles FCF angle or α, tilt angle or β, COX *angle or* γ, *the angle each* CF bond makes with the C_3 axis of the CF_3 group or δ, and the FCO angle for the F atom in the FCOX *plane or* θ. Specification of α *and* β fixes the angles δ and θ since only two of the four angles α, β, δ and θ are *independent*. *The angle of tilt*, β, is in the FCOX plane between the C_3 axis of the CF_3 group and the C−O bond. For *a positive angle of tilt the* F *atom in the* FCOX *plane* is closer to the O atom than are the two out-of-plane F atoms. The *following structural parameters were used for* both CF_3OF and CF_3OCl: $R(C-F) = 1.319$ Å, $R(C-O) = 1.395$ Å, $\alpha = 109.4°$, $\beta = 4.1°$, $\delta = 70.5°$, $\theta = 105.4°$. For CF_3OF $R(O-F) = 1.421$ Å and $\gamma = 104.8°$. For CF_3OCl, $R(O-Cl) = 1.70$ Å and $\gamma = 112.8°$. These two parameters were estimated by comparison of CF_3OF with F_2O[31] and F_2O[31] with Cl_2O[31]. Since the OF bonds in CF_3OF and F_2O differ by only about 0.01 Å, the O−Cl bond length from Cl_2O is used for CF_3OCl. Since the Cl−O−Cl angle in Cl_2O is 8° larger than the F−O−F angle in F_2O, the Cl−O−Cl angle in CF_3OCl is taken as 8° larger than the C−O−F angle in CF_3OF. The principal moments of inertia for CF_3OF in amu·Å^2 are 89.6, 164.6 and 166.0 and the asymmetry parameter is 0.98. The principal moments of inertia for CF_3OCl in amu·Å^2 are 89.6, 254.9 and 256.4 and the asymmetry parameter is −0.99. The α, β, γ and δ used in this note are defined in Fig. 1 of Ref. 5 and do not correspond to the angles defined in our Fig. 3 in all cases

© Heyden & Son Ltd, 1980

31. L. E. Sutton (ed.), *Tables of Interatomic Distances and Configuration in Molecules and Ions*, Special Publication No. 11, p. M 67. The Chemical Society, London (1958).
32. L. Pierce, R. Jackson and N. DiCianni, *J. Chem. Phys.* **35**, 2240 (1961); L. Pierce, N. DiCianni and R. Jackson, *J. Chem. Phys.*, **38**, 730 (1963).
33. M. M. Rochkind and G. C. Pimentel, *J. Chem. Phys.* **42**, 1361 (1965).
34. A. Ruoff, H. Bürger and S. Biedermann, *Spectrochim. Acta Part A* **27**, 1359 (1971); R. W. Kirk and P. M. Wilt, *J. Mol. Spectrosc.* **58**, 102 (1975).
35. A. Müller arnd B. Krebs, *J. Mol. Spectrosc.* **24**, 180 (1967); B. Krebs, A. Müller and A. Fadini, *J. Mol. Spectrosc.* **24**, 198 (1967); J. L. Duncan, and I. M. Mills, *Spectrochim. Acta*, **20**, 1089 (1964).
36. The F matrix is 13 × 13 and the off diagonal elements that are set to zero are the following: all involving τ, all involving γ except with l and d, all involving d except with l and γ.
37. J. F. Ogilvie, *Can. J. Spectrosc.* **19**, 171 (1974).
38. J. D. Witt and R. M. Hammaker, *J. Chem. Phys.* **58**, 303 (1973).
39. K. O. Christe, C. J. Schack and E. C. Curtis, *Inorg. Chem.* **10**, 1589 (1971).
40. P. N. Noble and G. C. Pimentel, *Spectrochim. Acta Part A*, **24**, 797 (1968).
41. W. B. Fox and G. Franz, *Inorg. Chem.* **5**, 947 (1966).
42. A. F. Clifford, *J. Phys. Chem.* **63**, 1227 (1959).
43. The mixing of CF_3 group modes with modes of the remainder of the molecule has been reported previously. See for example, E. C. Tuazon, W. G. Fateley and F. F. Bentley, *Appl. Spectrosc.* **25**, 374 (1971).
44. See Table 15 in Ref. 18.
45. A symmetry coordinate is classified as making the dominant contribution to a column in Table 5 if the corresponding entry is greater than 67% of the sum of the entries in that column or if the corresponding entry is a factor of 4 or more larger than the next largest entry in that column.
46. The normal modes in the A' block that have reasonable symbols in Table 1 are: CF_3OF, $\nu_{as}(CF_3)A'$, $\nu(OF)A'$ and $\delta_{as}(CF_3)A'$; CF_3OCl, $\nu_{as}(CF_3)A'$ and $\delta_{as}(CF_3)A'$.
47. The normal mode symbols where the symmetry coordinate for which the normal modes is named makes the largest but not the dominant contribution are: CF_3OF, $\delta_s(CF_3)A'$, and $\rho(CF_3)A'$; CF_3OCl, $\nu(OCl)A'$ and $\delta_s(CF_3)A'$.
48. The normal mode symbols where another symmetry coordinate makes the largest contribution are: CF_3OF, $\nu_s(CF_3)A'$, $\nu(CO)A'$ and $\delta(COF)A'$; CF_3OCl, $\nu_s(CF_3)A'$, $\nu(CO)A'$; $\delta(COCl)A'$ and $\rho(CF_3)A'$.
49. See Table 1, footnote *e*.

Received 7 January 1980

© Heyden & Son Ltd, 1980

DATE

ILMED

-8